

# Development of a Model for Propeller Tip Vortex Cavitation and Analysis of the Radiated Pressure Fluctuations

Yasaman Mirsadraee

PhD Thesis



**Development of a Model for Propeller Tip Vortex  
Cavitation and Analysis of  
the Radiated Pressure Fluctuations**

Yasaman Mirsadraee

Technical University of Denmark  
Department of Mechanical Engineering  
Section for Fluid Mechanics, Coastal and Maritime Engineering

September 2018



# Abstract

The work presented in this thesis focuses on developing a numerical model for predicting the inception of tip vortex cavitation as well as the dynamics of the developed tip vortex cavity and the associated pressure fluctuations. The inception is predicted by either the comparison of the minimum pressure coefficient and the cavitation number (engineering criterion) or based on monitoring the temporal evolution of a set of spherical nuclei in the tip vortex pressure field (bubble growth approach). For the latter, the Rayleigh-Plesset equation together with the Johnson-Hsieh equation of motion are solved to predict the trajectory and the growth behaviour of the nucleus. Once inception occurs, the vortex line is divided in numerous segments and the dynamic behaviour of each cavitating segment is predicted using the Rayleigh-Plesset equation for a 2-D cylindrical bubble placed at the center of a vortex. In this work, the tip vortex cavitation (TVC) model is fully integrated into the DTU-developed boundary element method (BEM), called ESPPRO. The input data to the TVC model, i.e. the blade tip circulation and Reynolds number, are provided by the BEM part of the implementation.

It is known that the periodic growth and collapse of the blade sheet cavitation contributes mostly to the first and second-order pressure fluctuations (fluctuations occurring at or twice the blade passing frequency). The third and higher-order fluctuations, however, are assumed to be mainly influenced by the dynamics of the cavitating tip vortex. The higher-order fluctuations can be significant if there is sheet cavitation that extends beyond the trailing edge and interacts with the cavitating tip vortex. This interaction is accounted for in this model by using the span-wise average thickness of the blade sheet cavity at the trailing edge as initial radius of the developed tip vortex cavitation.

The numerical model developed here is shown to be convergent with regards to discretization of the cavitating vortex segments. The calculation results are dependent on the value of the outer domain radius of the vortex flow model. The growth of the viscous core radius and the circulation strength along the tip vortex line downstream of the blade is found to influence the results in terms of the cavity radius and the amplitude of the higher-order pressure fluctuations.

The two methods mentioned above for predicting the inception of tip vortex cavitation are applied to a submarine propeller for which a measured inception

## *Abstract*

curve is available. The results of the two methods are compared to each other and also to the experimental results. The results of both methods are very similar with the bubble growth approach being the more conservative of the two.

Two public well-known benchmark test cases have been used for validation. The first case is the INSEAN E779a propeller in open water that develops a stable long cavitating tip vortex which is reproduced by the model. The second case is the KCS propeller for which experimental results with wake field of the model and the full-scale ship are available. This propeller develops only a short cavitating tip vortex in the wake peak region. The agreement between the calculation results and the results from the experiment is good for both cavitation extent and pressure fluctuations, especially for model-scale wake field. The calculation results show larger higher-order amplitudes when interaction of sheet and tip vortex cavitation is included.

Propeller designers are highly dependant on the ship wake field for their design. Two marine propellers designed for the same bulk carrier but for the nominal model-scale and the effective full-scale wake fields have been analysed. The axial components of both wake fields are scaled to the same overall wake fraction to ensure the same mean inflow velocity. It is shown that it is crucial to have the correct wake field distribution as the basis for the design. The dynamics of tip vortex cavitation is pronounced when there is an interaction between sheet and the cavitating tip vortex and it can be seen in the hull pressure fluctuations.

# Resumé

Arbejdet, som præsenteres i denne afhandling, omhandler kavitation, som dannes i hvirvlen fra bladtipperne på en skibspropeller. I arbejdet er der fokus på udviklingen af en numerisk model, ved hjælp af hvilken man kan beregne ikke alene dannelsen af tiphvirvelkavitation, men også det dynamiske forløb af den allerede udviklede tiphvirvelkavitation samt de tilhørende trykvariationer i det omgivende vand. Registrering af en tiphvirvels opståen sker enten ved at sammenligne minimum trykkoefficient med kavitationstallet (ingeniørkriterium) eller ved at registrere udviklingen af kugleformede nuclei i trykfeltet fra hvirvelen (boble-vækst). I sidstnævnte tilfælde løses Rayleigh-Plesset ligningen sammen med Johnson-Hsieh bevægelsesligningen, hvorved man kan beregne bevægelsesbanerne og væksten for nuclei. Når tiphvirvelkavitation er begyndt, inddeles tiphvirvelbanen i segmenter, hvis dynamik modelleres ved hjælp af Rayleigh-Plesset ligningen for en cylindrisk boble omkring segmentet. I det foreliggende arbejde er den numeriske model for tip-hvirvelkavitation fuldstændig integreret i programkoden ESPPRO, der beregner propellerstrømninger ved hjælp af rand-element-metoden. ESPPRO er udviklet på DTU.

Det er velkendt, at den periodiske dannelse, vækst og henfald af lagkavitationen på propellerbladet bidrager mest til trykpulsationerne ved bladfrequensen og den dobbelte bladfrequens. Tredje- og højereordens fluktuationer antages at stamme hovedsageligt fra den kaviterende tiphvirvel. Disse højereordens pulsationer kan være betydelige, hvis der forekommer lagkavitation, som også udstrækker sig bag den følgende kant på bladet, og som er i vekselvirkning med den kaviterende tiphvirvel. Denne vekselvirkning er beskrevet i den foreliggende model, idet den gennemsnitlige tykkelse af lagkavitationen langs bladets følgende kant benyttes som begyndelsesradius for tiphvirvelkavitationen.

Den numeriske model er konvergent med hensyn til diskretisering af segmenterne af den kaviterende tiphvirvel. Beregningsresultaterne afhænger imidlertid af størrelsen af radius af det ydre område af hvirvelstrømningsmodellen. Forøgelsen af radius af den viskose kerne og styrken af cirkulationen langs tiphvirvlen bag bladet har betydning for kavitationsradius og for trykpulsationerne ved højere frekvenser end bladfrequensen.

Begge metoder nævnt ovenfor til at beregne dannelsen af tiphvirvelkavita-

*Abstract (in Danish)*

tion er anvendt for en U-båds-propeller, for hvilket der foreligger måleresultater. Resultaterne af de to metoder er meget ens, idet dog metoden med boble-vækst giver de mest konservative resultater.

To propellere, for hvilke omfattende undersøgelser er offentliggjort i litteraturen, har været benyttet til at validere den udviklede beregningsmetode. Den ene propeller er INSEAN E779a, som i åbent vand udvikler en lang, stabil, kaviterende tiphvirvel. Dette genskabes udmærket af den foreliggende beregningsmodel. Den anden propeller er KCS-propelleren, for hvilken der foreligger forsøgsresultater for propellermodellen i medstrømsfeltet i modelskala og i et simuleret fuldskalamedstrømsfelt. Denne propeller udvikler kun en kort kaviterende tiphvirvel i området med lille tilstrømning til propelleren. Overensstemmelsen mellem resultater fra beregninger og forsøg er god, både for udbredelsen af kavitationen og for trykpulsationerne, især for beregningerne med medstrømsfeltet fra modelskala. Beregningerne giver større trykamplituder ved højereordens frekvenser, når der tages hensyn til vekselvirkningen mellem lag- og tiphvirvelkavitation.

Propellerdesignere er i høj grad afhængige af, at skibets medstrømsfelt er nøjagtigt. To propellere, optimeret for den samme bulkcarrier, er analyseret. Propellerne er optimeret på basis af henholdsvis det nominelle og det effektive medstrømsfelt. For kun at vise indflydelsen af fordelingen af medstrømmen er begge felter skaleret (aksial hastighed) til den samme middelmædstrøm. Beregningerne viser, at det er meget vigtigt at have den korrekte medstrømsfordeling. Også her viser beregningerne, at vekselvirkningen mellem tiphvirvel og lagkavitation på bladet har stor indflydelse på såvel tiphvirvelens dynamik som på trykamplituderne på skroget.

# Acknowledgements

Over the course of completing my Ph.D., I see many people that deserve to be acknowledged without whom the completion of this project would have not been possible. First and foremost, I would like to express my deepest gratitude to my manager at MAN Energy Solutions, Henrik Huse Nørgaard, because he believed in me in the first place, and supported me throughout the project. Words are not able to express how much I appreciate his openness, support and kindness.

I would like to thank my supervisor, Assoc. Prof. Poul Andersen, first of all for providing me with this opportunity. Throughout the past three years, he has always been very supportive, patient and open-minded as well as made time for discussion and provided me with valuable insight and advice.

A very special thank you to my colleague, Pelle Bo Regener. I learned and benefited significantly from his inputs, ideas and our discussions. It was an honour to work closely with him and I appreciate his support throughout the past three years.

Thank you to Prof. Jens Honore Walther, my co-supervisor at DTU and to Johannes Schön who was my industrial supervisor during his time at MAN Energy Solutions. I received invaluable help and guidance from Johannes before and during the initial phase of my studies. I would like to thank him for his guidance and support and that he always made time for answering my questions.

I would also like to thank Prof. Moustafa Abdel-Maksoud for giving me the opportunity of spending my external stay at TUHH. The two months I spent at TUHH were invaluable for the development of my work.

Stephan Berger deserves a special thank you because he was not only very helpful and open during my time at TUHH but also made the time to respond to any questions afterwards.

I'd also like to thank other colleagues at FVM, without them I wouldn't have had so much fun during these 3 years.

Lastly, my family deserve a very special acknowledgement, because of always being there for me and motivating me especially during the final stages of the work.



# Preface

This thesis is submitted in partial fulfilment of the requirements for the Ph.D. degree. The studies have taken place at the Technical University of Denmark, Department of Mechanical Engineering, Section for Fluid Mechanics, Coastal, and Maritime Engineering.

The student was employed at MAN Energy Solutions during the entire studies (March 2015 – March 2018). The project was supervised by Assoc. Prof. Poul Andersen and co-supervised by Prof. Jens Honore Walther.

The financial support was provided by Innovation Fund Denmark through the project titled “Development of Improved Cavitation and Noise Radiation Prediction Methods for Marine Propellers” and MAN Energy solutions, Frederikshavn, Denmark.



# Contents

<b>Abstract</b>	<b>iii</b>
<b>Abstract (in Danish)</b>	<b>v</b>
<b>Acknowledgements</b>	<b>vii</b>
<b>Preface</b>	<b>ix</b>
<b>1 Introduction</b>	<b>1</b>
1.1 Cavitation and its Types . . . . .	2
1.2 Tip Vortex Cavitation . . . . .	5
1.3 Existing Methods for Modelling Tip Vortex Cavitation . . . . .	8
1.4 Present Method . . . . .	10
<b>2 Tip Vortex Cavitation Modelling</b>	<b>15</b>
2.1 Description of the Vortex Field . . . . .	15
2.2 Inception of Tip Vortex Cavitation . . . . .	18
2.3 Developed Tip Vortex Cavitation . . . . .	21
<b>3 Numerical Analysis and Verification</b>	<b>29</b>
3.1 Spherical Bubble Dynamic Behaviour . . . . .	29
3.2 Dynamics of a Cylindrical Bubble Growth . . . . .	30
3.3 Dynamic Behaviour of Developed Cavitating Tip Vortex . . . . .	33
3.4 Convergence Study . . . . .	36
3.5 Influence of $R_D$ and Growth of the Vortex Strength and Core Size on TVC Dynamic Behaviour . . . . .	48
<b>4 Application to Marine Propellers</b>	<b>51</b>
4.1 Study on Tip Vortex Cavitation Inception . . . . .	51
4.2 INSEAN E779a Propeller in Uniform Inflow Conditions . . . . .	57
4.3 KCS Propeller in Non-Cavitating and Cavitating Flow Conditions . . . . .	64
4.4 Impact of Hull Reynolds Number on Propeller Cavitation . . . . .	77
<b>5 Conclusions and Outlook</b>	<b>97</b>
5.1 Discussion and Conclusions . . . . .	97
5.2 Recommendations for Future Work . . . . .	99

xi

*Contents*

<b>Nomenclature</b>	<b>101</b>
<b>List of Figures</b>	<b>105</b>
<b>References</b>	<b>109</b>

# 1 Introduction

Marine propellers typically operate in a non-uniform inflow field, which is mainly caused by the formation of the boundary layer around the ship hull as it moves through the water. As the propeller rotates behind the ship, the profile sections experience variations in the angle of attack. This implies that the blade surface pressure varies as the propeller rotates and depending on the blade position, this pressure may fall below the vapour pressure. Under these circumstances, an intermittent growth and collapse of vapour cavities on the surface of the propeller blade takes place.

The unsteady behaviour of the vapour cavities may have a number of harmful effects among which one can refer to the blade surface erosion, underwater radiated noise, high levels of induced pressure fluctuations on the hull surface and excessive noise inboard the ship. For this reason blade designers consistently try to control cavitation by means of modifying the blade geometry. Reducing cavitation, however, is associated with decrease in propeller efficiency and therefore, designers seek to find a balance between cavitation behaviour of the propeller and its efficiency.

It becomes apparent that a tool capable of predicting cavitation during the design stage is crucial. To this end, currently computational fluid dynamic (CFD) tools are able to predict cavitation with high accuracy, however, as the computational cost is very high, they are not used on a daily basis during the design stage. Boundary element method is an alternative that offers the advantage of high computational efficiency while having an acceptable accuracy. Boundary element method for prediction of blade sheet cavitation has been used for decades. The details of the non-linear method for prediction of sheet cavitation in non-uniform inflow can be found in Fine (1992). It is believed that the contribution of blade sheet cavitation to hull pressure fluctuations is mainly limited to the first and second-order fluctuations (fluctuations occurring at or twice the blade passage frequency). When it comes to higher-order fluctuations, a major contributor is the dynamic behaviour of the cavitating tip vortex.

The aim of this study is to develop a model for predicting the inception and dynamics of developed tip vortex cavitation and to examine the influence of tip vortex cavitation on induced pressure fluctuations on the surface of the ship hull.

## 1.1 Cavitation and its Types

Cavitation refers to a condition under which there exist vapour cavities inside a previously homogeneous liquid. Cavitation occurs when pressure becomes so low that the bond between liquid molecules cannot withstand it and they break apart. In other words, there is a pressure threshold under which cavitation begins. This threshold will be discussed in more details later in this chapter. In the literature one can find various ways of categorizing different types of cavitation. For example, Franc and Michel (2004) divide them into three categories of:

1. Attached sheet cavitation: Cavity with glossy surface that is fixed to the surface it originates from. Sharp pressure gradient after a suction peak on the back side of a blade causes the flow to detach from the surface and creates a sheet attached to the surface.
2. Travelling isolated bubbles: Individual or a cluster of bubbles that are flowing with the fluid. They can be the result of a nucleus undergoing expansion when travelling through a low pressure region or remnants from an attached sheet cavity that are shed to the free stream flow.
3. Vortex cavitation: Cavitation nuclei present in the water can get sucked into the core of vortical structure(s) due to the low pressure in this region and undergo unlimited growth and result in vortex cavitation.

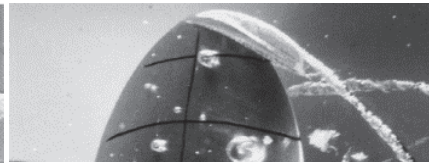
This is perhaps a more generalized form of categorizing different cavitation types. When it comes to marine propellers, one can distinguish between sheet (partial and/or super-cavity), bubble, cloud, hub and tip vortex cavitation. According to model and full-scale observations, the propeller usually experiences one or a combination of the mentioned types (see Figure 1.1). However, this depends on the propeller design and the flow conditions. In the following, different types of cavitation are explained in more detail and special attention is paid to tip vortex cavitation which is the main subject of this thesis.

Sheet cavitation on marine propeller blades is to a certain extent accepted on the suction side (back surface) of the blade. This type of cavitation occurs when the blade section is working at a non-ideal angle of incidence which may result in large suction pressure close to the blade leading edge (Carlton 2007). For single-screw propellers and under normal working conditions, as the propeller rotates behind the ship and reaches the top position, sheet cavitation begins to form on the suction side of the blade which is commonly attached to the blade leading edge. In this region (around 12 o'clock position), the propeller is more susceptible to sheet cavitation due to lower hydrostatic pressure and larger positive angle of attacks. Depending on the propeller design and the ambient

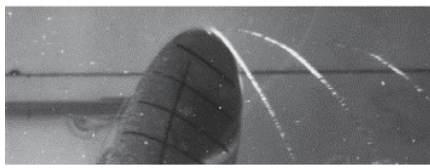
1.1 Cavitation and its Types



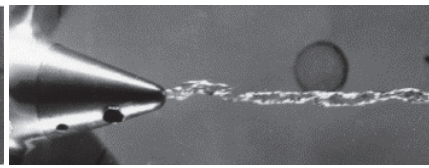
(a) Smooth sheet cavitation (with tip vortex cavitation)



(b) Bubble cavitation (with tip vortex cavitation)



(c) Tip vortex cavitation



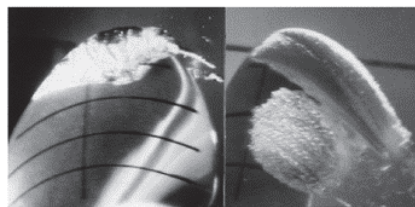
(d) Hub vortex cavitation



(e) Cloud, collapsing sheet cavitation



(f) Collapsing bubble cavitation



(g) Sheet with uneven surface and small bubbles (with tip vortex cavitation)

**Figure 1.1:** Various forms of cavitation. By courtesy: SSPA Sweden AB, Gothenburg, Sweden

## 1 Introduction

condition, sheet cavitation continues to grow on the surface of the blade in both radial and chord-wise direction due to increase of angle of incidence and/or decrease of local cavitation number as the blade rotates. As the blade passes the top region, it then enters regions with higher hydrostatic pressure and smaller angle of attacks, and sheet cavitation begins to shrink on the surface and disappears. Sheet cavitation is usually characterized as being stable, however, under certain circumstances an unstable sheet cavity which forms into cloud cavitation emerges. In the case of negative angle of attack, sheet cavitation may occur on the face (pressure side) of the blade which is strongly linked to erosion and must be avoided (Carlton 2007).

As is apparent from the name, bubble cavitation is characterized by individual bubbles occurring mainly in case of suction peak in the mid-chord region of the blade and due to profiles with high thickness and camber ratios. This form of cavitation can be very harmful and lead to blade surface erosion in case cavitation bubbles collapse on the surface of the blade.

As mentioned earlier, unstable sheet cavitation can result in foamy cavitating structures at the cavity trailing edge. This foam is defined as cloud cavitation and if it collapses on the surface of the blade it can result in erosion.

Vortex cavitation occurs in the core of the vortical structures shed from the propeller blade tip and the hub. Depending on the strength and size of the vortex, pressure at the center of the vortex can become so low that a cavitating tip or hub vortex can emerge.

Cavitation is mostly regarded as a harmful phenomenon because it can have severe effects. For example, extensive and unstable sheet cavitation on the suction side of the propeller blade can cause loss of performance by reducing lift. Noise and vibration is another impact of propeller cavitation. In this context, besides sheet cavitation, tip vortex cavitation plays an important role. When higher-order hull pressure fluctuations are concerned, it has been found that the dynamical behaviour of the cavitating tip vortex plays a significant role (ITTC (2008), Bosschers (2017), Kanemaru and Ando (2015), Wijngaarden et al. (2005), Wijngaarden (2011) and Berger et al. (2016)).

For each type of cavitation one can assume two distinct stages, one being the inception of cavitation, the stage between non-cavitating and cavitating flow and the other being the developed cavitation which refers to a stage when there exists an extent of cavity (Franc and Michel 2004). This distinction will be used throughout the entire thesis to better structure the work.

As discussed in the beginning of this chapter we need to know what the threshold pressure is for the cavitation to occur. For practical reasons, this pressure is usually taken equal to the vapour pressure. Using the two definitions of

## 1.2 Tip Vortex Cavitation

cavitation number (based on the propeller speed  $n$ ):

$$\sigma_n = \frac{p_\infty - p_v}{1/2\rho(nD)^2} \quad (1.1)$$

and the pressure coefficient:

$$C_{pn} = \frac{p - p_\infty}{1/2\rho(nD)^2} \quad (1.2)$$

the following can be used as a criterion for how stable the liquid is:

$$\begin{cases} \text{Cavitating,} & \text{if } -C_{pn,min} \geq \sigma_n \\ \text{Non-cavitating,} & \text{if } -C_{pn,min} < \sigma_n \end{cases}$$

where  $C_{pn,min}$  is the minimum pressure coefficient,  $\rho$  is the water density,  $p_v$  is the vapour pressure and  $n$  and  $D$  are the propeller speed and diameter, respectively. Here it is assumed that cavitation occurs at the point of minimum pressure in the water. With this criterion in mind, modelling of inception comes down to finding the minimum pressure coefficient.

## 1.2 Tip Vortex Cavitation

In general, circulation is not constant along the propeller blade but due to the compensating flow from pressure to suction side around the blade tip, it falls to zero when reaching the blade tip. This in turn results in a sheet of trailing vortices shed from the trailing edge of the propeller blade which is not stable and tends to undergo a roll-up process. The rolled-up portion of the vortex sheet form a distinct vortical structure, which is referred to as tip vortex in this work. Due to the roll-up, the circulation of the tip vortex is not constant rather it is assumed that it increases starting from an initial value ( $\Gamma_0$ ) to a value close to blade bound circulation ( $\Gamma_b$ ) with distance from the tip. Figure 1.2 illustrates growth of the circulation of the tip vortex downstream of the blade.

Tip vortex cavitation is usually the first type that takes place on marine propellers. This is linked to the intense pressure drop towards the center of the vortex which can in turn lead to inception of cavitation at higher cavitation numbers compared to other cavitation types. Experiments show that tip vortex cavitation first occurs at a short distance behind the blade tip and as it develops, it becomes attached to the tip (Franc and Michel 2004, Carlton 2007). This is an indication that the roll-up process has already begun close to the blade tip so that the strength of the rolled-up vortex is large enough for the inception to happen (Franc and Michel 2004). Tip vortex cavitation is known to be a

## 1 Introduction

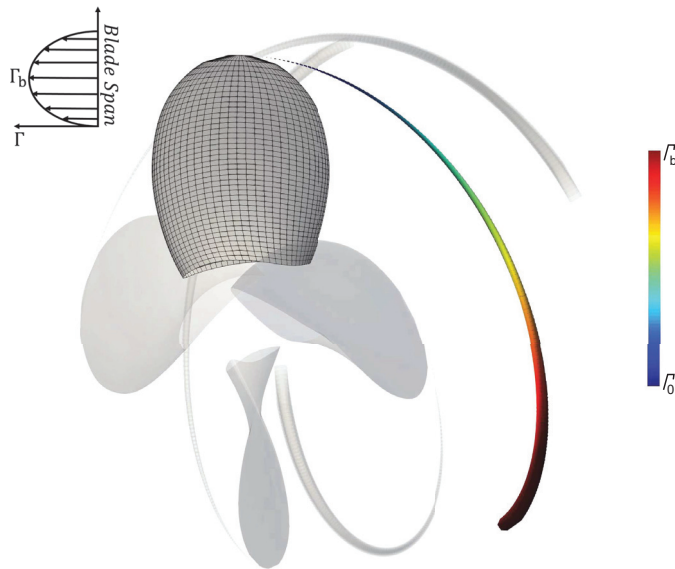


**Figure 1.2:** Schematic of growth of tip vortex strength

rather stable type. This is likely to be related to the way that the vortices are generated. Vortices generated at the tip of propeller blades, are well-shaped, steady structures attached to the solid boundary and are constantly supplied with circulation (Franc and Michel 2004).

Examples of previous studies on scaling and prediction of tip vortex cavitation inception are McCormick (1954; 1962), Kuiper (1981), Arndt et al. (1985), Hsiao et al. (2000) and Arndt (2002). These studies try to find the factors governing inception of cavitation in trailing vortices at the tip of the blade. For instance, McCormick (1962) attempts to estimate minimum pressure in the core of the vortex. This work of McCormick is an extension to his work during his Ph.D. studies (McCormick 1954). In his investigation, he first attempted to develop an analytical expression for predicting critical cavitation index (incipient cavitation number) which ended up with no success. He then carried on with developing a semi-empirical approach to be able to explain the experimental results. McCormick's work represents a good example showing the complexity of this phenomenon and the difficulties associated with predicting minimum pressure along the vortex path. Roll-up and instability of trailing vortex sheet and the effect of viscosity on the vortex strength are the main reasons for diffi-

## 1.2 Tip Vortex Cavitation

culties of this problem (Franc and Michel 2004, McCormick 1962). A conclusion from his work that is also one of the main assumptions behind today's tip vortex cavitation models is that the thickness of the boundary layer on the pressure side at the tip of the trailing edge has an influence on the inception of tip vortex cavitation. In other words, he was able to show that thickening the boundary layer on the pressure side reduces the critical cavitation index (McCormick 1962).

Several authors, e.g. Billet and Holl (1981) and Fruman et al. (1992), proposed the following scaling law for tip vortex cavitation inception:

$$\sigma_i = KC_L^2 Re^{0.4} \quad (1.3)$$

where  $\sigma_i$  denotes the incipient cavitation number,  $C_L$  is the lift coefficient,  $Re$  is the Reynolds number and  $K$  is a constant of proportionality. McCormick (1962) suggests an exponent of 0.35 for the influence of Reynolds number. Franc and Michel (2004) investigate the validity of this correlation based on the measurements provided in earlier studies and they find out that this correlation is not a universal one. For instance, the critical cavitation number and lift coefficient measurements carried out by Pauchet et al. (1994) for NACA 16020 and 0020 elliptic foils reveal that the relation is only linear for a limited range of  $C_L$  and in that range the slope varies depending on the foil section. Also, another study carried out by Fruman et al. (1995) reveals that the effect of the hydrofoil planform on the tip vortex cavitation should not be neglected (Franc and Michel 2004).

Experiments have also shown that for pure liquid inception of tip vortex cavitation does not happen at vapour pressure but at a lower pressure due to large surface tension. However, presence of impurities in the liquid such as dissolved gases or the so-called cavitation nuclei help to accelerate inception. This suggests that in fact water quality has a rather large influence on the inception of cavitation and therefore it is an important factor when considering scaling of inception.

Developed tip vortex cavitation is characterized by a cavitating core varying in diameter along the tip vortex line. This cavitating tube can be attached to the tip of the blade or can be in the form of an intermittent cavitating structure. The latter happens when inception is discontinuous due to flow conditions. The extent of the work done previously on modelling of developed tip vortex cavitation is limited. The phenomenon is complex and the previous studies can be categorized into three major groups. More details regarding different methods will be discussed in the next section.

### 1.3 Existing Methods for Modelling Tip Vortex Cavitation

Tip vortex cavitation is considered to be harmful mainly because of the underwater radiated noise, higher-order hull pressure fluctuations and rudder erosion. First-order pressure fluctuations are mainly caused by the blade loading variation, and periodic growth and collapse of sheet cavitation. However, when it comes to higher-order frequencies, i.e. multiples of the blade passing frequency, the tip vortex cavitation is found to be an important contributor (Berger et al. 2016). Therefore, it is crucial to model this type of cavitation to be able to predict the performance of the propeller with regards to higher-order pressure fluctuations during the design stage. This section gives a brief overview of the available methods and tools for predicting propeller cavitation and hull pressure fluctuations.

There are a large number of studies with the aim of modelling propeller cavitation, mostly sheet cavitation and to a much lesser extent tip vortex cavitation, and the associated hull pressure fluctuations. The methods used to address this problem fall into three major categories. A group of studies that make use of computational fluid dynamics taking into account the viscosity, a group with potential flow based methods assuming an inviscid fluid and a rather small group which make use of semi-empirical formulas.

Research studies that fall into the first category show promising results when it comes to cavitation that develops on the propeller surface and also the first-order hull pressure fluctuations. However, simulations show that capturing the cavitating tip vortex is more challenging because it requires a sufficiently fine grid to resolve the low pressure in the core of the vortex. For example, Shin (2016) used detached-eddy simulation (DES) for a propeller that shows extensive tip vortex cavitation in experiment. He suggests that a subsequent grid refinement based on a preliminary CFD solution can be an effective approach to achieve improved simulation results and he is able to show that. However, there are still deviations compared to the experimental results when it comes to e.g. the length of the cavitating tip vortex. No hull pressure fluctuations data are available in this study to further validate the results.

Similar to this study, is the work of Yilmaz et al. (2017), where DES is used to simulate the cavitation on the benchmark test-case E779a propeller. It is shown that in order to capture the cavitating tip vortex, the grid has to be refined around the propeller tip area. Results after refining the mesh show that the tip vortex cavitation is better captured, however, the extent is shorter compared to the experimental results. Lloyd et al. (2017) reached the same conclusion

### *1.3 Existing Methods for Modelling Tip Vortex Cavitation*

that the effect of mesh refinement is the largest in the tip vortex region, and the extent of the cavity differs based on the grid resolution. It appears from above that viscous CFD methods are able to capture the significant aspects of the problem, but they require very fine meshes in the tip region to be able to resolve the cavitating tip vortex and the work in this area is still an ongoing effort.

An early contributor to the potential flow based models is the work of Szantyr which dates back several decades (Szantyr 1985). In 1991, in an effort to develop a new, improved computer program, he developed an algorithm for detection of inception of sheet, bubble and tip vortex cavitation (Szantyr 1991). He then extended that work in 1994, where he used lifting surface method for the propeller and modified the initial geometry to account for the deformation of the blade surface due to the presence of the sheet cavity. He used vortices to model the hydrodynamic loading and sources to represent blade thickness and sheet cavitation. The cavitating tip vortex core diameter is then found by a simple formula and potential sources are used to model the resulting disturbances. To account for the dynamics of the cavitating tip vortex from one blade angular position to another additional sources are used (Szantyr 1994). In a later study (Szantyr 2007), the model for tip vortex cavitation is further improved in the way that the cavitating core of the vortex is divided into small segments and each segment's dynamical behaviour is solved using the Rayleigh-Plesset equation for a cylindrical bubble.

In the potential flow based category, one can refer to the work of Lee and Kinnas (2001) and later Lee (2002). Simulating a vortex field in potential flow requires the fundamental assumption that all the vorticity is confined in the vortex core and that outside the core the flow is irrotational. Lee (2002) has also assumed that the tip vortex cavitation is already fully developed and attached to the blade tip. His method is basically an extension to the sheet cavitation model developed by Fine (1992), meaning that the potential at an arbitrary point in the fluid domain is obtained by the Green's third identity considering that all surface boundaries including the tip vortex cavity surface are represented by a continuous distribution of sources and dipoles and the blade wake by continuous distribution of dipoles. The final tip vortex cavity shape is obtained in an iterative manner starting with an initial shape (circular cylinder) and satisfying the dynamic boundary condition which requires the pressure to be equal to the known cavity pressure everywhere inside and on the tip vortex cavity. The sheet cavitation and developed tip vortex cavitation results for DTMB N4148 propeller are compared to those from the experiment. There seems to be a qualitative agreement for the tip vortex cavity radius, but there is no hull pressure fluctuations comparison to further validate the results.

## 1 Introduction

The most recent work in the area of modelling tip vortex cavitation and higher-order hull pressure fluctuations is the work of Berger et al. (2016) which is based on a hybrid approach consisting of three components. First, the effective wake field is computed using a coupled RANS-BEM approach. Secondly, boundary element method is used to calculate the unsteady propeller loads and sheet cavitation. Lastly, the dynamics of a cavitating tip vortex is simulated using a model based on Rayleigh-Plesset equation and a model for describing the vortex flow field. The required inputs to the tip vortex cavitation model, i.e. the propeller tip flow in non-cavitating and cavitating conditions are provided by RANS simulations.

The model by Berger et al. (2016) assumes numerous cavitating segments along the tip vortex line (similar to Szantyr (2007)) and the radius of each segment is computed using one of the two formulations suggested in their work. One formulation is based on a bidirectional coupling between the radial and circumferential momentum equations while the second formulation is based on the assumption that the cavitating segment does not alter the surrounding flow. This implies that the influence is only in one direction, i.e. from the vortex flow on the cavitating core. The influence of tip vortex cavitation on the hull pressure fluctuations is taken into account by introducing additional potential sources. In this work, a container vessel conventional propeller has been used for validation and the results for cavitation pattern and pressure fluctuations show good agreement with experimental results.

The third category concerns those studies where semi-empirical formulas are used to account for the influence of tip vortex cavitation on hull pressure fluctuations. Among those, one can refer to the work of Bosschers (2017) and Lafeber and Bosschers (2016) where they have used the ETV model (Empirical cavitating Tip Vortex). This model is based on the tip vortex index method of Raestad (1996) and needs vortex strength as the input to predict the cavity size for a given cavitation number.

### 1.4 Present Method

The objective of the present study is to develop an efficient tool for predicting the inception and dynamics of developed tip vortex cavitation (TVC) and the associated pressure fluctuations. This study serves a broader purpose of having a computationally-efficient and stand-alone tool for the analysis of the propeller performance including prediction of cavitation. To this end, the newly developed tip vortex cavitation model is integrated into the existing DTU-developed propeller panel code called ESPPRO.

ESPPRO is based on potential flow theory and uses boundary element

## 1.4 Present Method

method with constant strength sources and dipoles over quadrilateral panels for the analysis of the propeller performance including prediction of smooth attached blade sheet partial and super-cavitation (the method is described in Fine (1992) and Regener (2016)). The boundary element method is a well-known approach for propeller analysis and is known to be computationally more efficient than RANS methods while having an acceptable accuracy.

For the prediction of inception and dynamics of tip vortex cavitation, propeller tip flow including blade tip circulation and local velocity are required. In this work, this information is provided by the BEM part of the solution in contrast to a method where e.g. separate RANS simulations are performed to obtain input parameters for simulating the cavitating tip vortex. In the present method, first the inception of tip vortex cavitation is investigated (details are discussed in Section 2.2). When inception is signalled, the fully developed cavitating tip vortex is assumed to be attached to the blade tip trailing edge and to follow the tip vortex trajectory which is assumed to be known (the upper edge of the blade trailing wake geometry).

The cavitating vortex tube is then divided in numerous cylindrical segments and the behaviour of each segment in terms of the variation of cavity radius with time is studied independent of the surrounding neighbours (details are discussed in Section 2.3). Variations of the segments' volume over time is translated into potential sources placed along the vortex line. The TVC model communicates the source strengths back to the BEM part of the solution to account for the influence of the cavitating tip vortex on other flow components and also to calculate the hull pressure fluctuations. Figure 1.3 illustrates the sequence involved in analysing propeller performance including prediction of sheet and tip vortex cavitation and propeller-induced pressure fluctuations.

An advantage of having the tip vortex cavitation model as an extension to an existing panel code is that the need to transfer information and data from one computational tool to another is eliminated and therefore, the risk of error and the required time and effort is significantly lowered.

Moreover, the requirement for performing computationally-expensive CFD calculations to provide the required input data and considering assumptions to prepare the input data to be used in the potential domain are eliminated. As an example, sheet cavitation alters blade circulation and therefore also the circulation of the cavitating tip vortex segments. In the current method, the initial circulation of each cavitating tip vortex segment is extracted at a certain span-wise position at the blade trailing edge and therefore, the effect of sheet cavitation on the circulation is taken into account inherently.

In addition, the current method enables to account for the influence of tip vortex cavitation on other flow components in the computational domain in-

1 Introduction

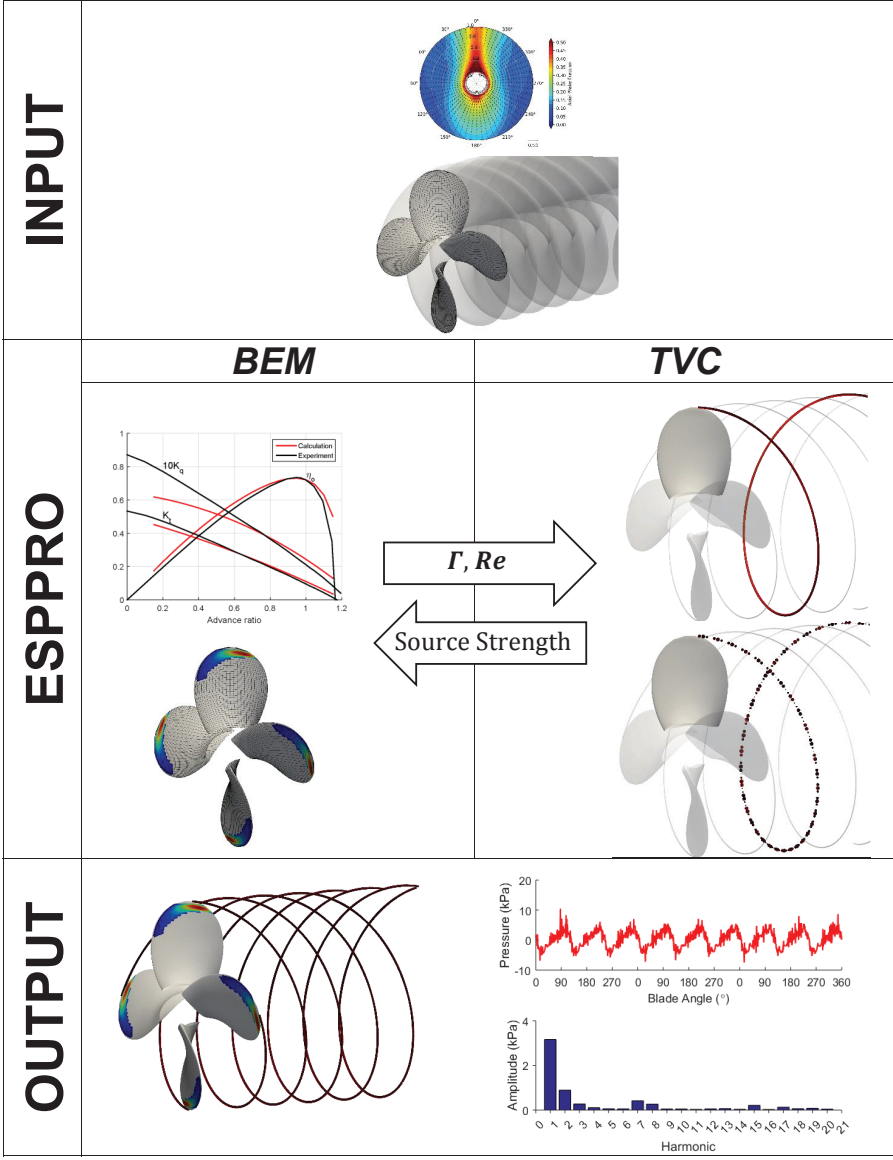


Figure 1.3: Flow chart showing the sequence involved in analysing propeller performance and induced pressure fluctuations

#### *1.4 Present Method*

cluding blade sheet cavitation, simply by adding the influence of the additional sources to the right hand side of the system of equations.

Having the TVC model as an integrated part of the panel code, enables to account for the effect of the roll-up on the vortex strength of the cavitating segments inherently, if the employed wake alignment technique allows for that.

Also, as is shown in the experiments when the blade sheet cavitation extends beyond the trailing edge, it merges into the tip vortex cavitation and thereby influences the cavitating core size. This method reduces the time and effort needed to take this influence into account simply because the two cavitation models are part of the same program which requires less time to perform calculations compared to RANS methods.



## 2 Tip Vortex Cavitation Modelling

In this chapter, the theory and solution strategy behind the tip vortex cavitation model and the applied boundary and initial conditions are described. The developed simulation method consists of a model for predicting inception of tip vortex cavitation and a model for the dynamics of the developed cavitating tip vortex which are explained in detail in the following.

### 2.1 Description of the Vortex Field

The backbone of the entire tip vortex cavitation model is the model for describing the vortex field (i.e. velocity and therefore pressure field near the vortex axis). The two most commonly used vortex models are Rankine and Burgers models with the Rankine model being the simpler one (Franc and Michel 2004). Both models consider two distinct regions, a viscous core within which all the vorticity is confined and an outer potential region. Within the core, the vorticity is constant and the fluid flow follows solid body rotation and therefore the local velocity increases with distance from the center. In the potential region, vorticity is non-existent and the velocity decays with the distance from the vortex center. This implies that the maximum velocity occurs at the boundary between the viscous and the potential region.

According to the Rankine model for two-dimensional vortices, the tangential induced velocity as a function of the radial distance from the vortex axis is:

$$v_T(r) = \begin{cases} \frac{\Gamma}{2\pi r} & r \geq R_c \\ \frac{\Gamma}{2\pi R_c} \left( \frac{r}{R_c} \right) & r < R_c \end{cases} \quad (2.1)$$

$\Gamma$  is the vortex circulation and  $R_c$  is the vortex core radius which is related to the boundary layer thickness in the tip region. Many authors suggest that the viscous core radius is related to the thickness of a fully turbulent boundary layer over a flat plate of the length equal to the chord length at  $0.95R$  (Latorre 1982, Franc and Michel 2004, Szantyr 2007, Hundemer and Abdel-Maksoud 2009):

$$R_c \propto \delta = \frac{0.37C_{0.95R}}{Re^{0.2}} \quad (2.2)$$

## 2 Tip Vortex Cavitation Modelling

where  $\delta$  is the thickness of the boundary layer and  $Re = Vc/v$ .

Using Euler's equation in a cylindrical coordinate system, the Rankine vortex pressure field is obtained:

$$p_{vortex}(r) = \begin{cases} p_{\infty} - \frac{\rho}{8} \left( \frac{\Gamma}{\pi r} \right)^2 & r \geq R_C \\ p_{\infty} + \frac{\rho}{8} \left( \frac{\Gamma}{\pi R_C} \right)^2 \left[ \left( \frac{r}{R_C} \right)^2 - 2 \right] & r < R_C \end{cases} \quad (2.3)$$

where  $p_{\infty}$  is the reference pressure and  $\rho$  is the water density. This leads to an expression for the minimum pressure at the center of the Rankine vortex:

$$p_{min} = p_{\infty} - \rho \left( \frac{\Gamma}{2\pi R_C} \right)^2 \quad (2.4)$$

The tangential velocity and the minimum pressure at the center of the Burgers vortex are as follows:

$$v_T(r) = \frac{\Gamma}{2\pi R_C} \left[ 1 - \exp \left( -1.256 \frac{r^2}{R_C^2} \right) \right] \quad (2.5)$$

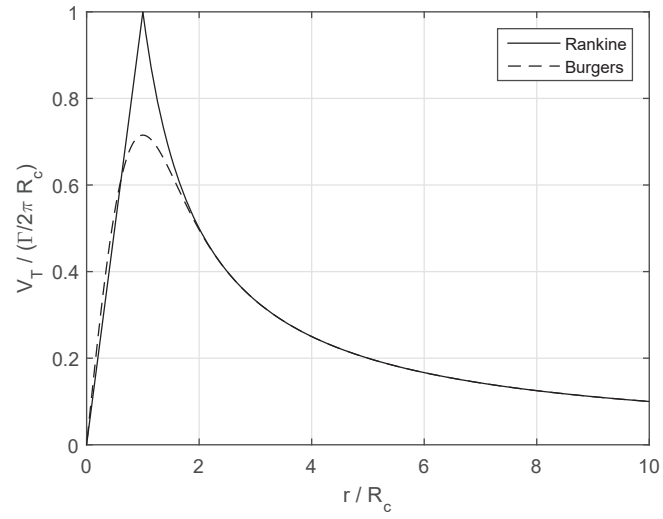
$$p_{min} = p_{\infty} - 0.871\rho \left( \frac{\Gamma}{2\pi R_C} \right)^2 \quad (2.6)$$

Figure 2.1 shows the velocity distribution for both the Rankine and the Burgers vortex models. As can be seen in the figure, the main difference between these models is the value of the maximum velocity. Burgers model suggests maximum velocity that is approximately 30% lower than the maximum velocity predicted by the Rankine vortex model. Hundemer and Abdel-Maksoud (2009) suggest that the real vortices do not reach the minimum pressure predicted by the Rankine vortex model, however in this study, the Rankine vortex model is used primarily because of a more straight-forward implementation.

### 2.1.1 Vortex Strength and Trajectory

The vortex velocity field can be predicted by Equation 2.1 using an estimate for the vortex circulation and the viscous core radius. In this study, it is assumed that the tip vortex trajectory coincides with the upper edge of the blade trailing wake sheet. The tip vortex line is then divided in segments corresponding to the accompanying wake elements in size. This is visualized in Figure 2.2, where an arbitrary segment  $i$  and the tip vortex line are shown in red and black, respectively. Assuming segment  $i$  which is born at  $t = t_i$  at the tip trailing edge, the segment's circulation  $\Gamma_i$  is the circulation at the trailing edge and at

## 2.1 Description of the Vortex Field



**Figure 2.1:** Rankine and Burgers vortex velocity distributions

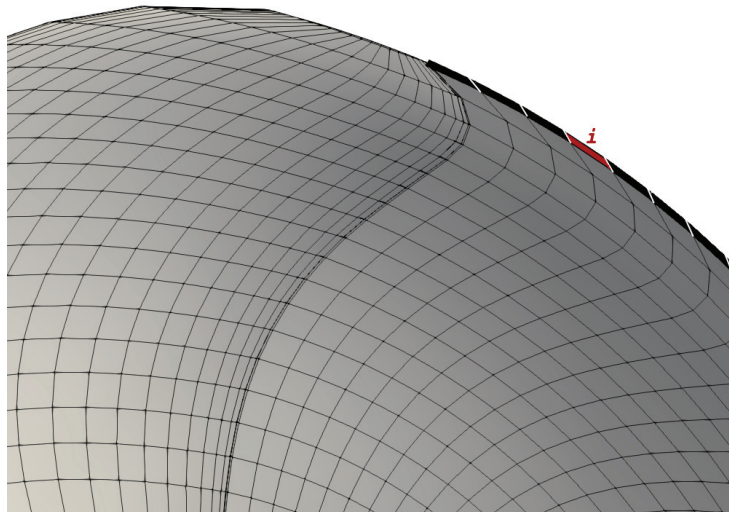


**Figure 2.2:** Tip vortex trajectory following the upper edge of the trailing wake sheet and the tip vortex segments

## 2 Tip Vortex Cavitation Modelling

a specific span-wise position ( $0.95R$  in this work) and  $R_{c_i}$  is obtained using Equation 2.2. This segment is then convected downstream along the vortex line with circulation and viscous core radius approximated by one of the two following implementations.

One implementation assumes that the segment's circulation and viscous core radius are constant as the segment travels downstream, and thus  $\Gamma_t(t) = \Gamma_i$  and  $R_{c_t}(t) = R_{c_i}$ . The other implementation, however, considers that the segment's circulation and viscous core radius grow from their initial value of  $\Gamma_i$  and  $R_{c_i}$  to  $\Gamma_f (= \Gamma_b)$  and  $R_{c_f}$ , respectively.

It is well-known that the trailing vortex sheet rolls up downstream of the blade and as a consequence of that the strength of the tip vortex and the size of the viscous core grow (Franc and Michel 2004). Kuiper shows mathematically and experimentally that the roll-up process has no influence on the cavitating core radius (Kuiper 1981, p. 136 & 144). However, Berger et al. (2016) applied a different approach, assuming that the roll-up has an influence on the cavitating core radius and therefore, employed an empirical function to account for the growth of the vortex strength and core size with time as the propeller rotates.

In this study, both approaches are considered to investigate the influence of the growth of circulation and viscous core size on the radius of the cavitating core and its dynamics. When roll-up is considered, a similar formulation as suggested by Berger et al. (2016) is used to estimate the segment's circulation as it travels along the vortex line:

$$\Gamma_t(t) = \Gamma_b(t_i) (1 - (1 - \lambda) \exp(-\alpha t)) \quad (2.7)$$

where  $\Gamma_b$  is the blade bound circulation at the time when the segment was born ( $t_i$ ),  $\lambda$  is the ratio between initial and blade bound circulation at  $t_i$ , ( $\Gamma_i/\Gamma_b$ ), and  $\alpha$  is a constant which is adjusted so that the segment's circulation reaches the bound circulation after a certain time (half a revolution is selected in this study).

A similar approach is used to approximate the viscous core radius. Here it is assumed that the ratio between the initial and final viscous core radius is the same as for the circulation ( $\lambda$ ) and from that the final viscous core radius ( $R_{c_f}$ ) is found and then a similar formulation is used to estimate the evolution of the viscous core radius over time.

## 2.2 Inception of Tip Vortex Cavitation

As previously mentioned in Chapter 1.2, inception of tip vortex cavitation is a complex phenomenon and influenced by a number of factors and thus, difficult to mathematically model. Despite this complexity, a number of researchers

## 2.2 Inception of Tip Vortex Cavitation

e.g. McCormick (1962), Arndt et al. (1985), Hsiao et al. (2000) and Arndt (2002) have attempted to develop a mathematical model to predict the inception of tip vortex cavitation. In this section, two different approaches to address this problem are presented and discussed, namely the engineering criterion and the bubble growth approach.

### 2.2.1 Engineering criterion

The engineering criterion is a simple criterion based on two main assumptions that cavitation occurs at the point of minimum pressure and that at this point, the pressure is equal to or below the vapour pressure. Therefore, the engineering criterion suggests that cavitation inception occurs when:

$$p_{min} \leq p_v$$

or using Eq. 1.1 and 1.2:

$$-C_{pn,min} \geq \sigma_n \quad (2.8)$$

The negative of the minimum pressure coefficient can be found by using Equation 2.4:

$$-C_{pn,min} = \frac{1}{2\pi^2(nD)^2} \left( \frac{\Gamma}{R_c} \right)^2 \quad (2.9)$$

### 2.2.2 Bubble Growth

The limitation of the simple engineering criterion is that it neglects some of the important factors influencing the inception of tip vortex cavitation, for example, water quality in terms of the size and distribution of cavitation nuclei present in water. Hsiao et al. (2000) carried out a numerical study to investigate the influence of different factors neglected by the simple engineering criterion on incipient cavitation number. In their study, they considered the tip vortex generated by three different sizes of otherwise geometrically similar hydrofoils operating at the same angle of attack. Using a spherical bubble dynamic model coupled with an equation of motion, they monitored the dynamic behaviour of cavitation nuclei of various initial sizes in the imposed flow field. Using two different criteria, acoustic and optical, they obtained the incipient cavitation number for each combination of scale and nuclei initial size. Optical criterion is based on monitoring the bubble size and inception is signalled when maximum bubble size ( $R_{B,max}$ ) gets larger than a given value. Acoustical criterion signals inception when the maximum detected noise ( $P_{max}$ ) gets higher than a given background value. According to their results, the incipient cavitation number

## 2 Tip Vortex Cavitation Modelling

is not well-predicted by Equation 2.8, if a strict detection scheme ( $P_{max} > 90db$  or  $R_{B_{max}} > 100\mu m$ ) is used, especially for the smaller nuclei. However, for less stringent thresholds ( $P_{max} > 130db$  or  $R_{B_{max}} > 400\mu m$ ) the cavitation inception number is insensitive to the nucleus size and is generally well predicted by Equation 2.8.

The approach based on monitoring the dynamic behaviour of a cavitation nucleus in the pressure field of the tip vortex has been used by other researchers as well e.g. Latorre (1982), Latorre and Ligneul (1993) and Szantyr (2007) and is explained in more detail in the following.

The bubble growth approach is based on the coupling of the Rayleigh-Plesset equation for the dynamics of a spherical bubble in the pressure field of a 2-D vortex with the Johnson-Hsieh formulation for the trajectory of the bubble (Latorre 1982). In this approach one or more bubbles with various initial radii are released close to the blade tip and the position and radius of each bubble are monitored over time. Cavitation inception is signalled when at least one bubble undergoes an unbounded growth. The Rayleigh-Plesset equation for the temporal evolution of a spherical bubble radius is as follows (Franc and Michel 2004):

$$\rho \left( R_B \ddot{R}_B + \frac{3}{2} \dot{R}_B^2 \right) = p_v - p - \frac{2S}{R_B} + p_{g_0} \left( \frac{R_{B_0}}{R_B} \right)^3 - 4\mu \frac{\dot{R}_B}{R_B} \quad (2.10)$$

where  $R_B$ ,  $\dot{R}_B$  and  $\ddot{R}_B$  are the bubble radius and its first and second time derivative, respectively.  $S$  is the water surface tension,  $\mu$  is the water viscosity,  $p_{g_0}$  and  $R_{B_0}$  are the initial gas pressure and radius of the nucleus.

One should be mindful how to interpret  $p$  in Eq. 2.10 as it has been treated in two different ways in the literature. The classical approach, used for example by Latorre (1982), is to use the pressure at the bubble center and in the absence of the bubble. However, the modified approach suggested by Hsiao et al. (2000) proposes to use the average of the ambient pressure over the surface of the bubble.

Obviously, the choice of  $p$  results in different bubble growth behaviours. In the simple classical approach, the bubble will undergo unbounded growth once pressure falls below the vapour pressure at the center of the vortex. Hsiao et al. (2000) discuss that this approach may lead to unrealistic results for cavitation inception number and therefore suggest that the modified approach should rather be used. They argue that the modified approach provides more realistic results for inception number because of the more realistic bubble behaviour predictions.

To predict the trajectory of the bubble as it travels towards the center of the vortex, the Johnson-Hsieh formulation is adopted as follows (neglecting the

### 2.3 Developed Tip Vortex Cavitation

buoyancy force acting on the bubble (Latorre 1982):

$$\dot{\vec{U}}_B = \frac{3}{4} (\vec{U}_f - \vec{U}_B) \left| \vec{U}_f - \vec{U}_B \right| \frac{C_D}{R_B} - \frac{3\nabla p}{\rho} + \frac{3}{R_B} (\vec{U}_f - \vec{U}_B) \dot{R}_B \quad (2.11)$$

The first term on the right-hand side is the viscous drag on the bubble, the second term is the force due to the pressure gradient in the liquid and the last term accounts for the variations in bubble volume. For more detailed explanation of each term refer to (Franc and Michel 2004, p. 67). In this equation,  $\vec{U}_B$  and  $\vec{U}_f$  are the bubble and fluid velocity respectively.  $C_D$ , the bubble drag coefficient, is determined by Haberman's empirical equation as follows (Latorre 1982):

$$\frac{C_D Re_B}{24} = 1.0 + 0.197 Re_B^{0.63} + 2.6 \times 10^{-4} Re_B^{1.38} \quad (2.12)$$

$Re_B$ , the bubble Reynolds number based on the relative velocity, is given by:

$$Re_B = \frac{2R_B \left| \vec{U}_f - \vec{U}_B \right|}{\nu} \quad (2.13)$$

where  $\nu$  is the water kinematic viscosity.

Equations 2.10 and 2.11 are solved by integrating in time using the fourth-order Runge-Kutta scheme (RK4). Choosing an appropriate time step size and numerical integration by RK4 result in an approximation of bubble radius ( $R_B$ ), its derivative ( $\dot{R}_B$ ) and the bubble position ( $\vec{X}_B$ ) at each time step. Depending on the cavitation number, the bubble dynamical behaviour will be different and inception occurs when the bubble experiences a continuous growth. The dynamic behaviour of a spherical bubble when the ambient pressure is lowered is analysed and discussed in 3.1.

## 2.3 Developed Tip Vortex Cavitation

In this study, it is assumed that the vortex flow field is not disturbed by the cavitating core. Besides this formulation, Berger et al. (2016) considered another formulation as well, in which the radial and circumferential momentum equations are coupled and solved sequentially. Intuitively, one would expect that the latter gives a more accurate description of the phenomenon. As also emphasized by Franc and Michel (2004), cavitation modifies the pressure and velocity field of the vortex drastically. However, the reason for choosing the former formulation in this study is that Berger et al. (2016) have shown that under certain circumstances the results from the former and latter do not differ drastically and the former provides sufficient accuracy for engineering problems.

## 2 Tip Vortex Cavitation Modelling

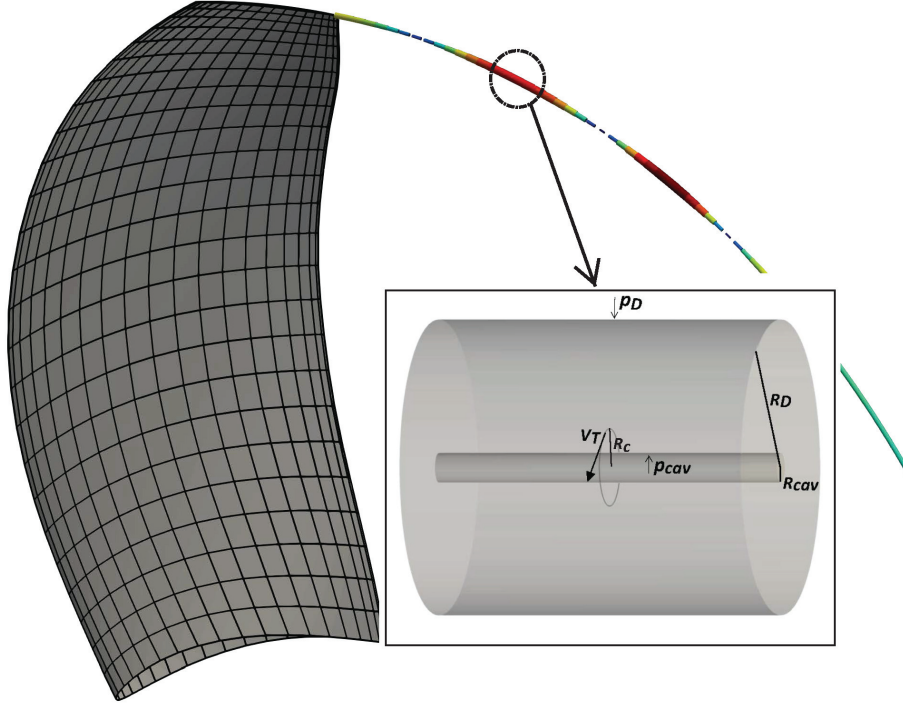


**Figure 2.3:** Configuration illustrating details of a cavitating vortex segment

For numerical simulation of the dynamics of the developed tip vortex cavitation, numerous cylindrical segments are placed on the axis of the vortex and the dynamic behaviour of each segment's radius is computed using the Rayleigh-Plesset equation for a cylindrical bubble (similar to the work of Szantyr (2007) and Berger et al. (2016)). With the assumption that the dynamics of the cavitating core does not have an influence on the vortex flow, Equation 2.1 can be used to define the tangential velocity field. Assuming an axisymmetric cylindrical cavitating vortex core,  $R_{cav}$ , limited by an external circular cylinder with radius  $R_D$  (see Figure 2.3), the Rayleigh-Plesset equation for the temporal evolution of a cylindrical cavity radius becomes (Franc and Michel 2004):

$$\left[ R_{cav} \ddot{R}_{cav} + \dot{R}_{cav}^2 \right] \ln \frac{R_D}{R_{cav}} + \frac{R_{cav}^2 \dot{R}_{cav}^2}{2} \left[ \frac{1}{R_D^2} - \frac{1}{R_{cav}^2} \right] = \frac{p_{cav} - p_D}{\rho} + \int_{R_{cav}}^{R_D} \frac{v_T^2}{R} dr \quad (2.14)$$

### 2.3 Developed Tip Vortex Cavitation

where  $R_{cav}$  is the cavitating core radius,  $R_D$  is the outer domain radius,  $p_{cav}$  is the pressure within the cavitating core and  $p_D$  is the pressure at the outer domain radius. The pressure within the cavity,  $p_{cav}$ , is given by:

$$p_{cav} = p_v + p_{g0} \left( \frac{R_{cav0}}{R_{cav}} \right)^2 - 2\mu \frac{\dot{R}_{cav}}{R_{cav}} - \frac{S}{R_{cav}} \quad (2.15)$$

The pressure integral assuming Equation 2.1 for the tangential velocity becomes:

$$\int_{R_{cav}}^{R_D} \frac{v_T^2}{r} dr = \begin{cases} \frac{\Gamma^2}{8\pi^2} \left( \frac{1}{R_D^2} - \frac{1}{R_{cav}^2} \right) & R_{cav} \geq R_c \\ \frac{\Gamma^2}{8\pi^2} \left( \frac{2}{R_c^2} - \frac{R_{cav}^2}{R_c^4} - \frac{1}{R_D^2} \right) & R_{cav} < R_c \end{cases} \quad (2.16)$$

Solving Equation 2.14 together with Equation 2.15 and 2.16 results in the dynamics of the radius of a cylindrical core placed at the center of the tip vortex. This equation is integrated numerically using a fourth-order Runge-Kutta scheme.

#### 2.3.1 Initial Conditions

To solve Equations 2.14, 2.15 and 2.16 numerically using the RK4 scheme, initial values for the radius of the cavity ( $R_{cav0}$ ) and its first time derivative ( $\dot{R}_{cav0}$ ) should be defined (system of two first order ODEs). A way to estimate an initial value for the cavity radius is to assume that the cavitating core is at equilibrium condition at  $t = 0$  and compute  $R_{cav0}$  using the steady state Rayleigh-Plesset equation. The steady state Rayleigh-Plesset equation which is obtained by setting the time derivatives in Equation 2.14 to zero, gives:

$$\frac{\Gamma^2}{8\pi^2 R_{cav,eq}^2} \left[ 1 - \left( \frac{R_{cav,eq}^2}{R_D^2} \right) \right] = \frac{p_D - p_v}{\rho} \quad (2.17)$$

where it is assumed that  $R_{cav,eq} \geq R_c$ . Here the equilibrium cavity radius is denoted by  $R_{cav,eq}$ . This implies that the first time derivative is selected to be zero at  $t = 0$  (i.e.  $\dot{R}_{cav0} = 0$ ). Experimental results show that when sheet cavitation extends beyond the blade trailing edge, it rolls up into the cavitating tip vortex and they do not remain two individually cavitating structures. Rather, they merge together in a mixing zone, see Figure 2.4. For such a case, the thickness of the sheet cavity at the trailing edge replaces the equilibrium radius for the initial value of the cavity radius. In other words, the initial radius of the cavitating vortex segment is chosen according to the following criterion:

$$R_{cav0} = \max \left\{ R_{cav,eq}, \frac{h_{cav}}{2} \right\} \quad (2.18)$$

## 2 Tip Vortex Cavitation Modelling



**Figure 2.4:** Sheet cavity rolling up into the cavitating tip vortex. By Courtesy: MAN Energy Solutions, Frederikshavn, Denmark

where  $h_{cav}$  is the span-wise average of the sheet cavity thickness at the blade trailing edge. The larger the deviation of the initial radius from the computed equilibrium radius, the higher the amplitude of the radius oscillations. This is discussed in more details in Section 3.3.2.

### 2.3.2 Other Relevant Considerations

In addition to the initial conditions, a number of other variables need special attention for an accurate simulation of the dynamics of the developed tip vortex cavity. These are discussed in the remainder of this section.

#### Time Step Size

There are two levels of time-discretization step size, an inner time step for the numerical time integration using the RK4 scheme ( $\delta t$ ), and an outer time step which is used for the propeller flow including the cavitating tip vortex ( $\Delta t$ ).

Selection of both time step sizes must be done with care to avoid erroneous results or loss of information. Careful selection of the inner time step size  $\delta t$  is important to ensure that the oscillations of each individual cavitating segment's radius is captured by the numerical time integration. Similarly, accurate prediction of the cavitating core radius oscillations along the entire

### 2.3 Developed Tip Vortex Cavitation

vortex line, and the resulting induced pressure fluctuations requires an outer time step size  $\Delta t$  which is smaller than what is commonly used in panel codes. The convergence behaviour of the model for various time step sizes is evaluated in Section 3.4. In the current study, the outer time step  $\Delta t$  is discretized into 400 time steps, i.e.  $\delta t = \Delta t/400$ .

#### Outer Domain Radius

As mentioned earlier in this chapter, each cavitating segment is represented by a cylindrical annulus with inner radius of  $R_{cav}$  and an outer radius of  $R_D$  (see Figure 2.3). The assumption of a finite outer cylinder is required to avoid the singular logarithmic behaviour that emerges in 2-D configurations (Franc and Michel 2004).

Berger et al. (2016) analyse and discuss the importance and the influence of  $R_D$  on the results. In their work,  $R_D$  is in most cases set to approximately ten times larger than the mean cavity radius. According to their investigation, for a single cavitating segment, all quantities, are influenced by the choice of  $R_D$  and the solution does not converge with increasing  $R_D$ . For the case of a propeller, they showed that the results for the higher-order pressure fluctuations are also influenced by the choice of  $R_D$  in a way that the amplitudes of higher harmonics become smaller and the lower-frequent higher harmonics become more pronounced. This investigation conveys that the choice of  $R_D$  must be made with care.

In this study,  $R_D$  is adapted in the simulation in such a way to ensure conservation of angular momentum at each time step. In order for the the angular momentum to be conserved, the area of the annulus ( $R_D^2 - R_{cav}^2$ ) must be kept constant. An initial area of annulus is computed based on the initial choice of  $R_D$  and for the subsequent time steps,  $R_D$  is computed so that the annulus area is constant. The initial  $R_D$  value is chosen to be at least ten times the initial cavity radius. This choice is justified by looking at variations of the vortex pressure with the distance from the vortex axis, see Figure 2.5. According to this figure, for distances larger than approximately ten times the viscous core radius, the pressure converges to a constant value. A numerical investigation of the influence of  $R_D$  on the higher-order pressure fluctuation results will be presented in Section 3.5.

#### Pressure at Outer Domain Radius

Regardless of the choice of the  $R_D$ , pressure at the outer boundary of the annulus must be found. For segments far from the propeller, the ambient pressure far from the vortex axis ( $p_D$ ) equals  $p_{atm}$  plus the hydrostatic pressure

## 2 Tip Vortex Cavitation Modelling

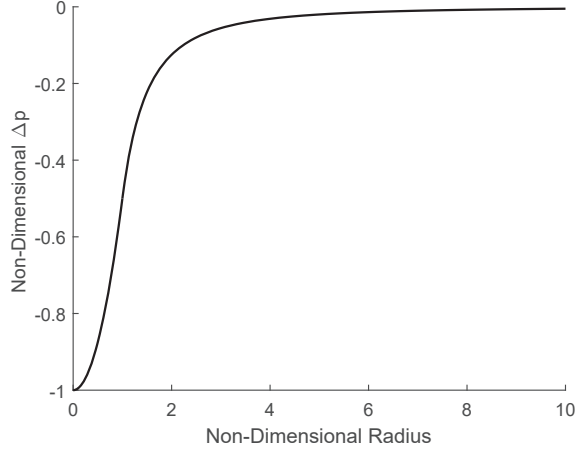


**Figure 2.5:** Rankine pressure distributions. Pressure difference is made non-dimensional by  $\rho \frac{\Gamma}{2\pi R_c}$  and radius by  $R_c$ .

due to the hydrostatic head above the vortex segment. However, for those segments in the vicinity of the propeller, the influence of the propeller flow on the pressure at the outer domain radius must be taken into account as well. This means that  $p_D$  changes as the segment travels downstream.

### Point Source Strength

The disturbance caused by the cavitating vortex segments can be approximated by representing each segment with a potential point source placed at the center of the segment. As the segments are considered to travel with the flow, the strength of the point source associated with segment  $k$  reduces to the following:

$$\sigma_k(t) = \pi dl_k \frac{dR_{cav,k}^2(t)}{dt} \quad (2.19)$$

where  $dl_k$  is the length of segment  $k$ . The potential induced at an off-body point located at  $d_q$  distance from the point source  $\sigma_k$  is given by:

$$\phi_q = -\sigma_k \left( \frac{1}{4\pi d_q} \right) \quad (2.20)$$

The total potential induced by the entire cavitating vortex line is then the sum of all individual induced potentials.

### 2.3.3 Influence of Tip Vortex Cavitation on Blade Flow

In this part, the approach to include the influence of the cavitating tip vortex on the the wetted or cavitating blade flow is explained.

The Green's formula for the field point on the blade surface ( $S_B$ ) is (Fine 1992):

$$2\pi\phi_p = \int_{S_B} \left[ \mu_B \frac{\partial}{\partial n_q} \left( \frac{1}{R_{p,q}} \right) - \left( \sigma_B \frac{1}{R_{p,q}} \right) \right] ds - \int_{S_{CW}} \sigma_{CW} \left( \frac{1}{R_{p,q}} \right) ds + \int_{S_W} \mu_W \frac{\partial}{\partial n_q} \left( \frac{1}{R_{p,q}} \right) ds \quad (2.21)$$

where the subscripts  $p$  and  $q$  denote the field and the variable point respectively, with  $R_{p,q}$  as the distance between the two points.  $n_q$  is the unit vector normal to the surface where point  $q$  lies on. Subscript  $B$  denotes the blade surface (wetted and cavitating),  $W$  denotes the trailing wake sheet surface (non-cavitating and cavitating) and  $CW$  denotes the cavitating portion of the wake surface.  $\mu$  is the continuous dipole and  $\sigma$  the continuous source distributions on their corresponding subscript surface.

To include the influence of the cavitating tip vortex segments on the potential at the field point, an additional term is added to the right-hand side of Equation 2.21. Assuming that the entire cavitating tip vortex can be approximated by a line of continuous source distribution, the additional integral term becomes:

$$- \int_{L_V} \sigma_V \left( \frac{1}{R_{p,q}} \right) dl$$

where  $\sigma_V$  is the strength of the continuous source distribution on the vortex line denoted by  $L_V$ . Adding the above term to Equation 2.21 and discretizing the surface boundaries and the singularities, the following equation is obtained for the potential induced at panel  $i$  on the blade surface :

$$2\pi\phi_i = \sum_{j_B=1}^{n_B} [-A_{ij_B} \mu_{j_B} + B_{ij_B} \sigma_{j_B}] + \sum_{j_{CW}=1}^{n_{CW}} C_{ij_{CW}} \sigma_{j_{CW}} - \sum_{j_W=1}^{n_W} W_{ij_W} \mu_{j_W} + \sum_{j_V=1}^{n_V} V_{ij_V} \sigma_{j_V} \quad (2.22)$$

## 2 Tip Vortex Cavitation Modelling

where  $A_{ij}, B_{ij}, C_{ij}, W_{ij}$  and  $V_{ij}$  are the elements of the influence coefficient matrices  $\mathbf{A}$ ,  $\mathbf{B}$ ,  $\mathbf{C}$ ,  $\mathbf{W}$  and  $\mathbf{V}$  containing the influence of the unit strength dipole or source on blade, wake or tip vortex panel  $j$  on blade panel  $i$ . The additional term does not introduce new unknowns to the system of equations, as the source strengths are already obtained as described in Section 2.3.2.

## 3 Numerical Analysis and Verification

In this chapter, relevant characteristics of the model are examined and verified. Furthermore, the convergence behaviour of the model when applied to a marine propeller is investigated.

### 3.1 Spherical Bubble Dynamic Behaviour

The bubble growth inception model (Section 2.2.2) uses the Rayleigh-Plesset equation for the evolution of the radius of a spherical bubble. To verify this part of the model, a case where a nucleus fixed in space is undergoing a given pressure drop at  $t = 0$  is considered. The results of this case are compared qualitatively with the results presented in Section 3.3 (p. 42) of Franc and Michel (2004) where they use the bubble interface velocity ( $\dot{R}_B$ ) to explain the results. The bubble interface velocity is obtained by using:

$$R_B \ddot{R}_B + \frac{3}{2} \dot{R}_B^2 = \frac{1}{2\dot{R}_B R_B^2} \frac{d}{dt} [\dot{R}_B^2 R_B^3]$$

and analytical integration of Equation 2.10:

$$\begin{aligned} \dot{R}_B^2 = & \frac{2}{3} \frac{p_v - p_\infty}{\rho} \left[ 1 - \frac{R_{B_0}^3}{R_B^3} \right] \\ & + \frac{2}{3(\gamma - 1)} \frac{p_{g0}}{\rho} \frac{R_{B_0}^3}{R_B^3} \left[ 1 - \left( \frac{R_{B_0}}{R_B} \right)^{3(\lambda-1)} \right] - \frac{2S}{\rho R_B} \left[ 1 - \frac{R_{B_0}^2}{R_B^2} \right] \end{aligned} \quad (3.1)$$

In this equation the viscous term is ignored. Moreover, the pressure drop is assumed to occur in such a short time that the transformation of the gas can be considered as adiabatic. Variations of the bubble radius ( $R_B$ ) over time, and variations of the  $\dot{R}_B^2$  over radius are plotted in Figure 3.1.

Looking at the results showed in Figure 3.1, one can distinguish between two main cases. One where the interface velocity  $\dot{R}_B^2$  has two roots ( $R_{B,0}$  and  $R_{B,1}$ ) and one where it only has one root ( $R_{B,0}$ ). When the bubble interface velocity

### 3 Numerical Analysis and Verification

has two roots, the velocity changes sign at these two values and the radius oscillates between the two (see Figure 3.1a, 3.1b). The oscillation behaviour of the bubble depends on the ratio of the roots,  $R_{B,1}/R_{B,0}$ . When the ratio is large, the motion is non-linear and the role of the gas pressure,  $p_{g0}(R_{B0}R_B)^{-3}$ , becomes dominant when  $R_B$  is small and close to  $R_{B,0}$  and less significant when it is close to  $R_{B,1}$ . For small ratio of the roots, however, the motion is harmonic and the frequency can be computed using the following expression (Franc and Michel 2004):

$$f_B = \frac{1}{2\pi R_B} \sqrt{\frac{1}{\rho} \left[ 3\gamma p_{g0} - \frac{2S}{R_B} \right]} \quad (3.2)$$

where  $\gamma$  is the ratio of heat capacity at constant pressure to heat capacity at constant volume,  $c_p/c_v$ . When the square of bubble interface velocity has only one root, the bubble interface velocity never changes sign and the bubble undergoes an unlimited growth (see Figure 3.1c).

The results shown here agree well with the results shown by Franc and Michel (2004). The linear oscillations frequency in this case (Figure 3.1a), matches the value computed using Equation 3.2 and the corresponding input values. In case of unlimited growth, the interface velocity square reaches the value of  $2(p_v - p_\infty)/3\rho$ , which is also reproduced by the model for the test case presented here (Figure 3.1c).

## 3.2 Dynamics of a Cylindrical Bubble Growth

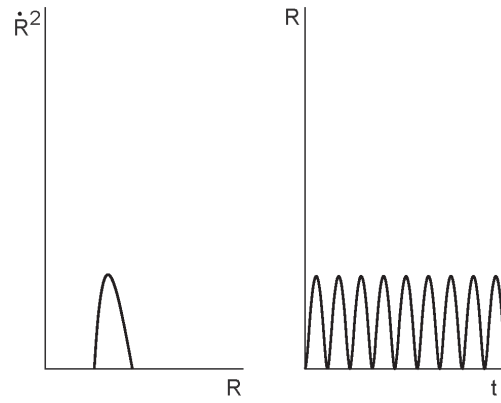
In this section, the tip vortex cavitation model (Section 2.3) is used to predict the dynamics of an isolated cylindrical bubble under reduced external pressure. Here a cylindrical bubble of an initial radius,  $R_{cav0}$ , under equilibrium condition with vapour content,  $p_{cav} = p_v$  is assumed. Reducing the external pressure from an initial value of  $p_{\infty_0}$  to  $p_{\infty_1}$ , breaks down the initial equilibrium and the bubble will eventually reach a new equilibrium state. The qualitative comparison is done with the results presented in Choi et al. (2009) where they investigate the dynamic response of a cylindrical bubble to changes in the far field pressure.

According to Equation 2.17, the new equilibrium radius is approximated by the following:

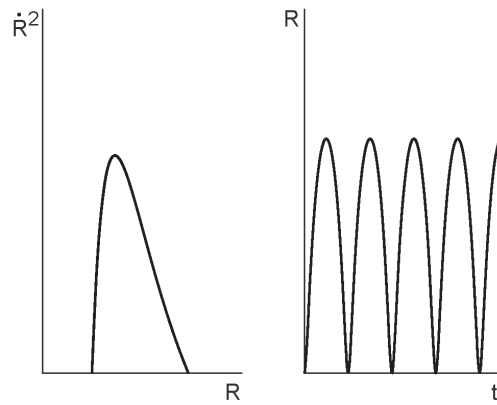
$$R_{cav1} \approx \sqrt{\frac{\rho\Gamma}{8\pi^2(p_{\infty_1} - p_v)}} \quad (3.3)$$

The radius will oscillate around the equilibrium radius with the following

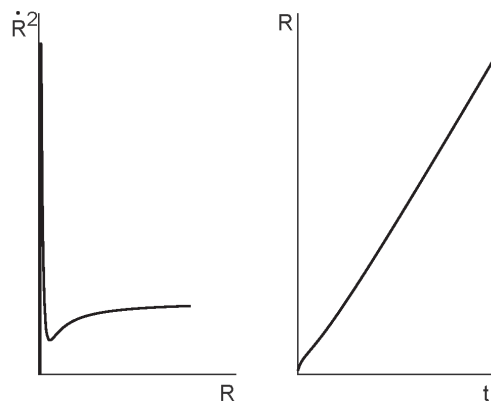
### 3.2 Dynamics of a Cylindrical Bubble Growth



(a) Linear oscillations



(b) Non-linear oscillations



(c) Unlimited growth

**Figure 3.1:** Calculation results for single bubble growth under decreased pressure

### 3 Numerical Analysis and Verification

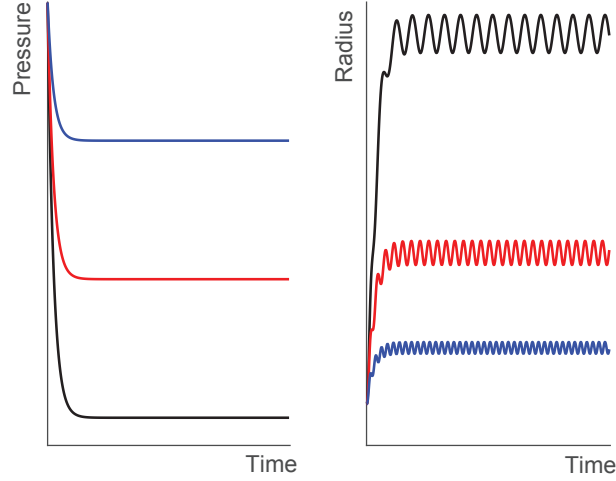


**Figure 3.2:** Growth of a cylindrical bubble as a function of time for varying final pressure value

period of oscillation:

$$T = \frac{4\pi R_{cav_1}^2}{\Gamma} \sqrt{\ln(R_D / R_{cav_1})} \quad (3.4)$$

Calculation results for the growth of a cylindrical bubble after application of a given reduction in the external pressure, over time period of  $\Delta t$  is presented in Figure 3.2 and 3.3. The results obtained in these cases, match the expected values obtained by Equations 3.3 and 3.4 for the final equilibrium radius and the period of oscillations.

As can be seen in Figure 3.2, the radius of the bubble begins to oscillate as soon as the bubble growth begins. After the pressure has reached its final value, the bubble radius begins to oscillate around a mean final value. The oscillations of the radius occur because when a cylindrical bubble placed in the center of a vortex undergoes an expansion, the bubble interface will experience lower tangential velocity at its interface. Lower tangential velocity means higher pressure at the interface which in turn results in decrease in bubble radius. This process repeats itself resulting in oscillations of the radius around a mean value. It can also be seen that the amplitude of the oscillations grows with the increase in applied pressure drop.

Figure 3.3 shows the bubble radius growth history for varying pressures.

### 3.3 Dynamic Behaviour of Developed Cavitating Tip Vortex

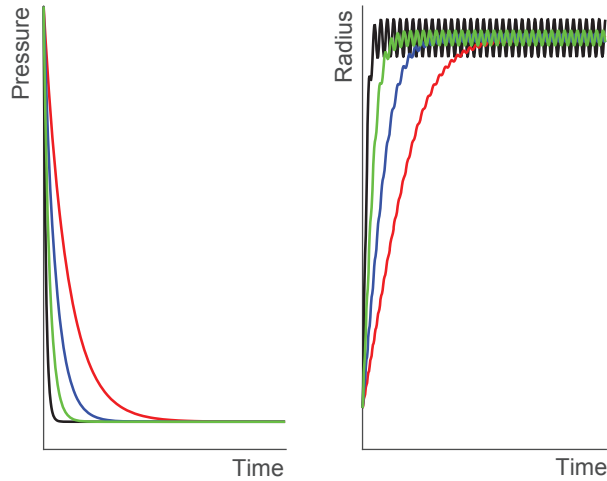


**Figure 3.3:** Growth of a cylindrical bubble as a function of time for varying  $\Delta t$  of the application of the final pressure value

Here the final pressure is the same but the rate of variation is different. It can be seen that the oscillation amplitude grows with the rate of application, i.e. the quicker the pressure reaches its final value, the larger the amplitude of oscillations is. It is also seen that the rate of application has no influence on the final value of the equilibrium radius. These results agree well with the results shown by Choi et al. (2009).

### 3.3 Dynamic Behaviour of Developed Cavitating Tip Vortex

In this part, the aim is to examine different characteristics of developed tip vortex cavitation. Figure 3.5 shows developed tip vortex cavitation attached to the blade tip of a conventional propeller. The conventional blade is the publicly available propeller geometry, Propeller S from Kuiper (1981) with a diameter equal to  $0.340\text{ m}$ , which in this study is run in an artificial non-uniform wake field and an operating condition that ensures inception and development of tip vortex cavitation corresponding to  $J = 0.43$  and  $\sigma_n = 0.68$ . Figure 3.4 shows the wake field used for Propeller S simulations. The simulation is limited to predicting tip vortex cavitation, i.e. sheet cavitation is not included here. Also,

### 3 Numerical Analysis and Verification

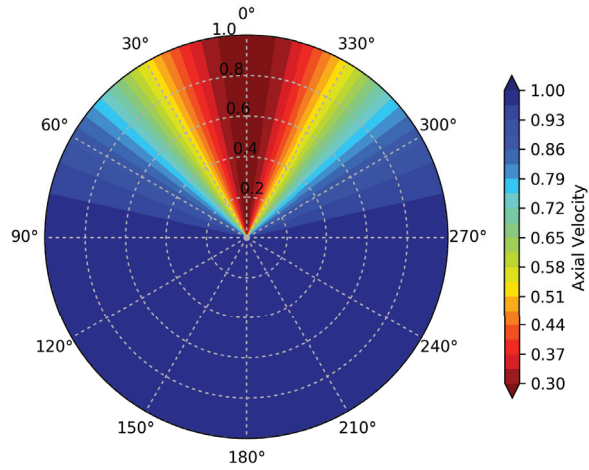


**Figure 3.4:** Artificial inflow field used for simulations with Propeller S

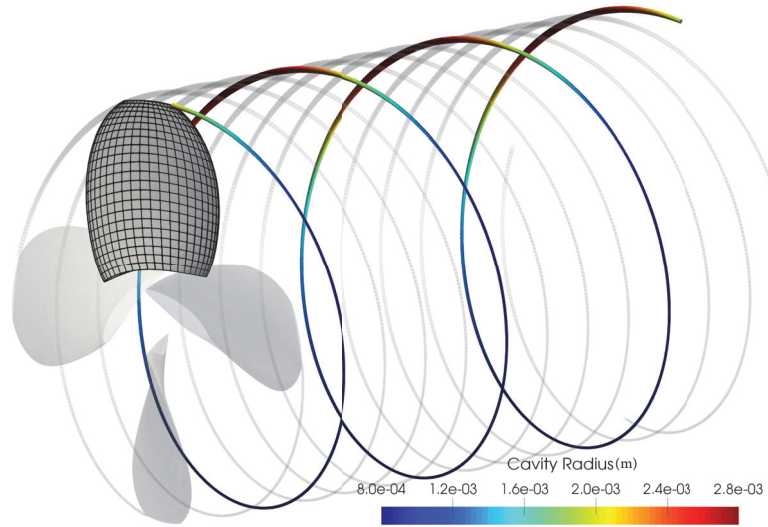
the segment's circulation and viscous core size is assumed to stay constant as the segment moves downstream along the tip vortex trajectory.

#### 3.3.1 Cavitating Vortex Radius Scale

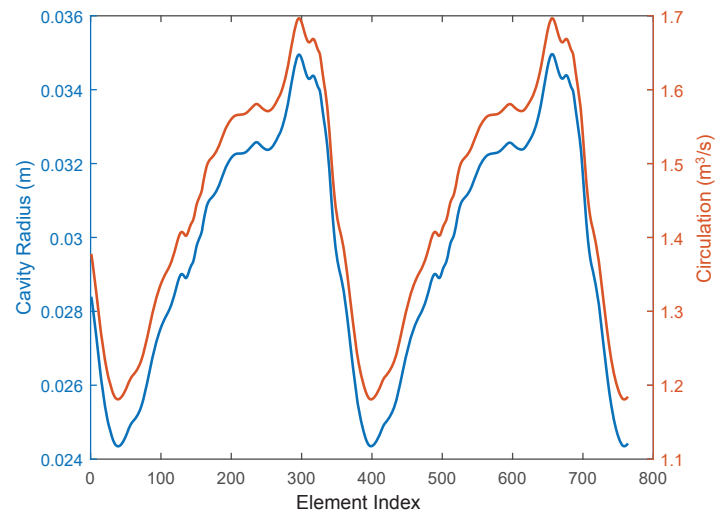
Based on Figure 3.5 the size of the cavitating core along the vortex line compared to the propeller radius appears reasonable; maximum radius is approximately 1% of the propeller radius. Variations of the cavity radius along the vortex line resemble variations of the tip circulation which is caused by the non-uniform inflow field. This can be explained by the Rayleigh-Plesset equation for a cylindrical bubble (Equation 2.14), where the driving force for the temporal evolution of the cavity is mainly the pressure difference exerted at the bubble boundary and the larger the segment's circulation, the stronger the driving force for the cavity to grow.

Figure 3.6 shows the circulation and radius of all segments along the vortex line at an instance of time. The x-axis in this figure shows the element index starting at 0, being the segment that is born at the given time step, and increasing along the tip vortex trajectory. This implies that the segment with element index 1 was born at the previous time step and so forth.

### 3.3 Dynamic Behaviour of Developed Cavitating Tip Vortex



**Figure 3.5:** Schematic of developed tip vortex cavitation. Model-scale propeller geometry (Propeller S)



**Figure 3.6:** Radius of the cavitating segments along the vortex line and the corresponding circulation at a single time-step

### 3.3.2 Cavitating Vortex Radius Oscillations

Figure 3.7 shows the dynamics of the radius of a single segment from the time it is born at the blade trailing edge and as it travels downstream of the blade for two cases of equilibrium and non-equilibrium initial radius. The x-axis shows the simulation time made non-dimensional by the period of oscillation. The equilibrium initial radius is given by Equation 2.17. The non-equilibrium initial radius used here is 1% larger than the calculated equilibrium radius. This is an arbitrary value and is only used to demonstrate the effect of a non-equilibrium initial radius on the final results.

According to this figure, for both cases the radius oscillates around a mean value as expected and explained in Section 3.2. The oscillations amplitude is minor and only slightly larger than 0.01% of the mean value in case of equilibrium initial radius, while it is significantly larger for the case of non-equilibrium initial radius. However, both cases oscillate around the same mean value. The lower part of this figure illustrates this fact more clearly. The dashed lines indicate the mean value around which the segment radius is oscillating. As it can be seen the difference between the two mean values is insignificant.

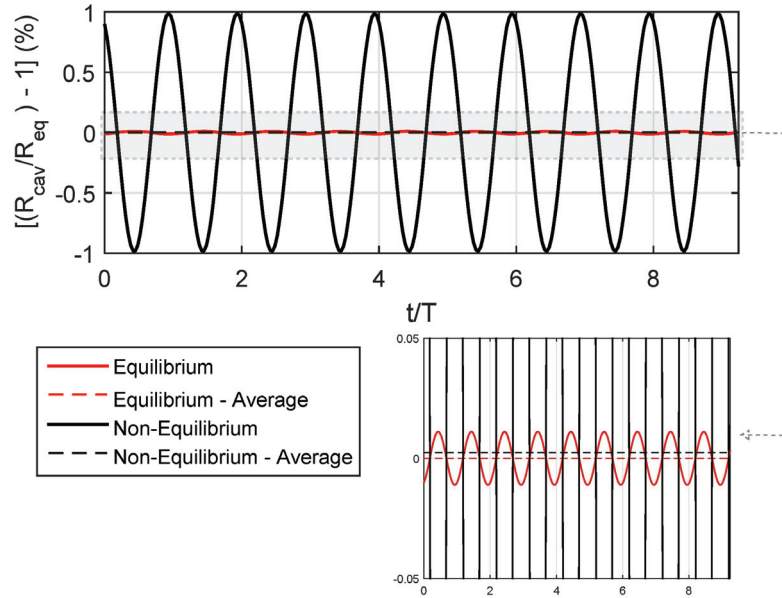
### 3.3.3 Total Volume of the Cavitating Tip Vortex

Figure 3.8 shows the variations in volume of the entire cavitating tip vortex at each time step and over six propeller revolutions. As the length of the tip vortex is set to two full revolutions ( $720^\circ$ ), the cavity volume keeps growing during the first two revolutions ( $\theta/2\pi = 2$ ) and for time steps after the initial growth, the cavity volume is almost constant with minor oscillations.

## 3.4 Convergence Study

As mentioned previously in Section 2.3.2, proper selection of the time step size ( $\Delta t$ ) (which in this work also determines the length of the cavitating vortex segments) is significant to avoid loss of information along the cavitating vortex line. For this reason, one has to do a convergence study to investigate the influence of the time step size on the results and to find an approximation for the appropriate magnitude of the time step.

For this study, the KRISO container ship propeller (KCS) in non-uniform inflow field is used. Section 4.3 provides an overview of this case. The main dimensions of the propeller and the operating conditions are listed in Tables 4.1 and 4.2 on p. 64 and 65. For this study, the model-scale effective inflow field shown in Figure 4.18e and the model-scale operating condition are used.



**Figure 3.7:** Average radius of a single segment when initializing with equilibrium and non-equilibrium radius (followed as it travels downstream)

The study is set up in such a way that the time step size ( $\Delta t$ ) is varied and the pressure signal at an off-body point located at a distance directly above the propeller (pick-up P2 in Figure 4.21) is recorded. By Fourier decomposing the resulting pressure time signal, the amplitudes of various harmonics are obtained. The amplitudes are then compared to study the influence of the time step size on the results.

Figure 3.9 shows the time signal of the total pressure, i.e. the pressure induced by the propeller including TVC, at the off-body point for various segment sizes ( $\Delta t$ ).  $\Delta t$  is given in degrees in the figures, and for this case,  $1.0^\circ$  corresponds to approximately  $10^{-4}$  s. Looking at this figure it seems that the time signals coincide, but when focusing on a smaller portion of the graph (lower plot), the influence of the segment size on the results is clearly noticeable. As it can be seen, for time step sizes larger than  $1.0^\circ$ , some data are lost and the higher-order oscillations are not captured.

Figure 3.10 shows the results of the Fourier decomposition of the pressure signal. One can see the peak that occurs at  $3^{rd}$  harmonic of the blade frequency, which is related to the presence of a cavitating tip vortex. Examining each

### 3 Numerical Analysis and Verification

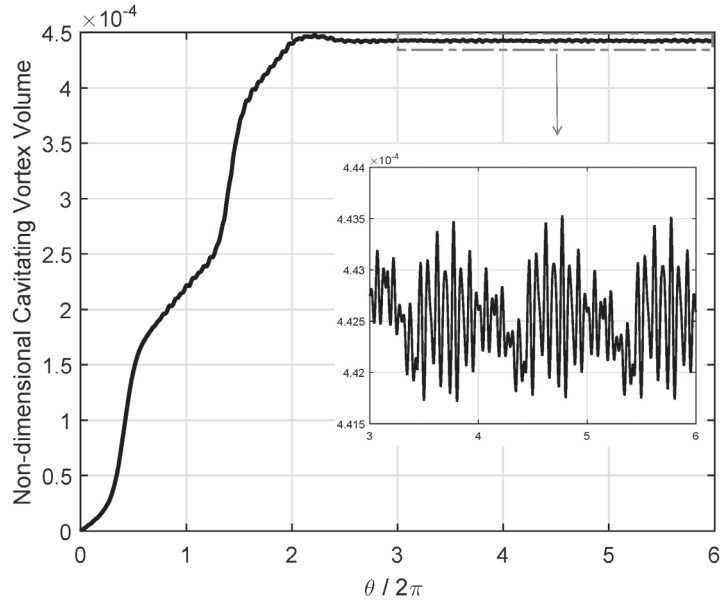


**Figure 3.8:** Cavitating tip vortex volume over six propeller revolutions.  $\theta$  is the angular position of the key blade

harmonic individually for the influence of the segment size, it can be seen that the amplitudes converge to a constant level at time step size corresponding to an angular step size of  $1.0^\circ$ .

Looking at the pressure signal induced by the cavitating tip vortex and its harmonics amplitude (Figures 3.11a and 3.11b), the same conclusion is drawn suggesting that increasing the time step size larger than  $1.0^\circ$  in this case, would lead to misleading results, e.g. in case of  $\Delta t = 4.0^\circ$  the peak has moved to the 4<sup>th</sup> harmonic.

The results presented above are generated assuming that the initial radius for TVC segments is the equilibrium radius. For the case where there is sheet cavitation that extends beyond the trailing edge, the radius of the cavitating segment generated at this time is different from the equilibrium radius (as discussed in Section 2.3.1). In such a case as seen in previous section for non-equilibrium initial radius, one would expect larger oscillation amplitudes of the radius and the cavity volume, which in turn results in larger amplitudes for the higher harmonics.

To investigate the influence of the non-equilibrium initial radius on the appropriate time step size, a similar study but with three different deviations

### 3.4 Convergence Study

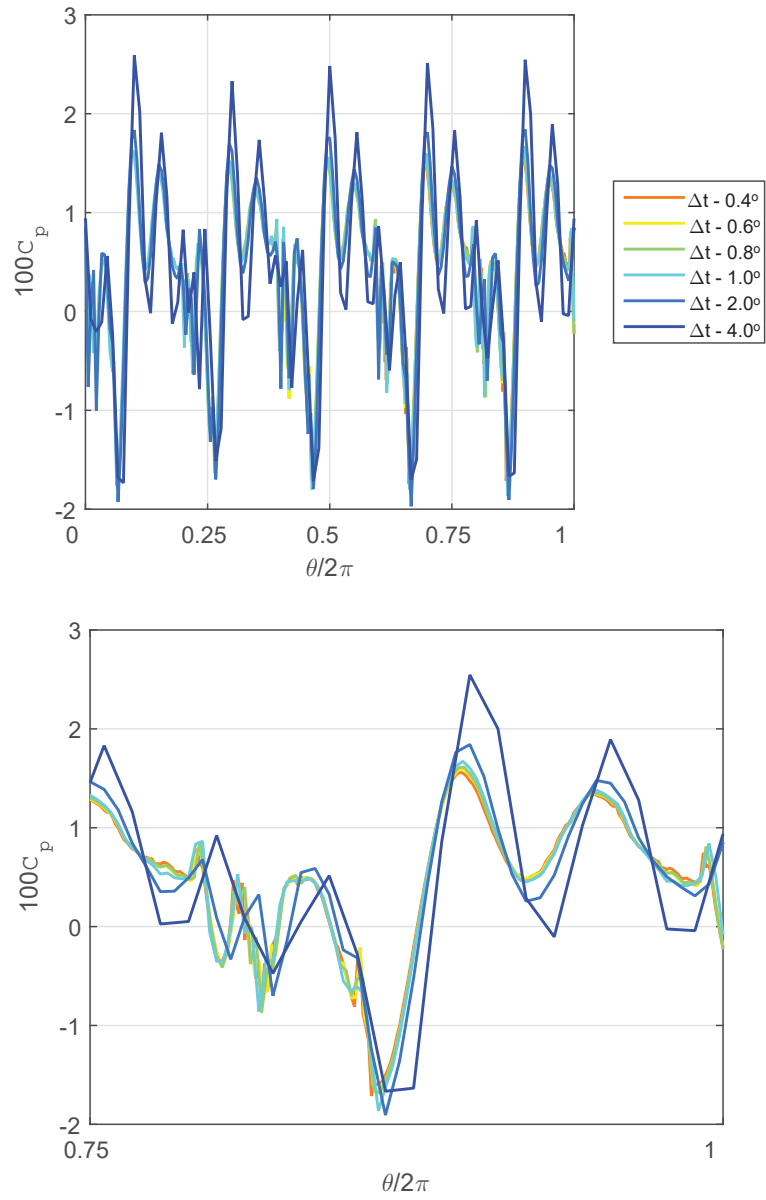


**Figure 3.9:** Total pressure time signal over one revolution (top) and zoom in (bottom) for varying segment sizes

### 3 Numerical Analysis and Verification

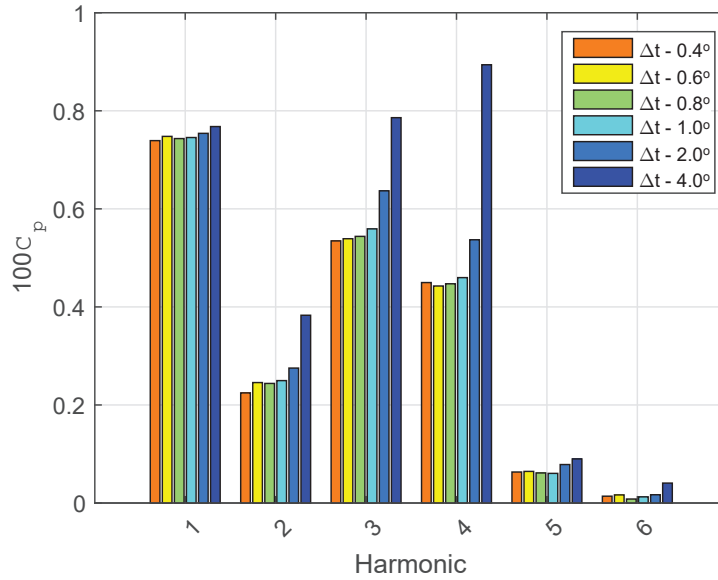
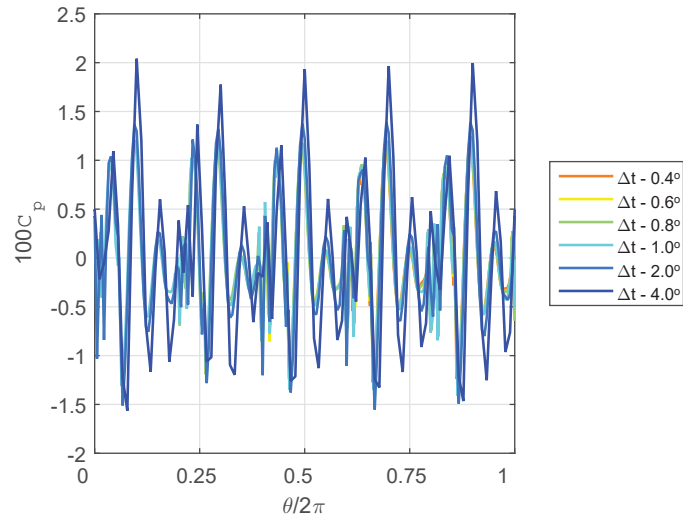


**Figure 3.10:** Harmonics amplitudes of the total pressure signal for varying segment sizes

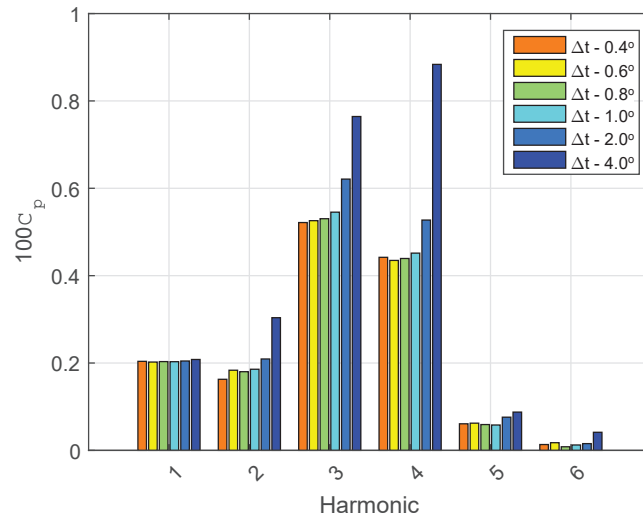
is carried out. The initial radii used here are 2, 5 and 10% larger than the equilibrium radius. Figures 3.12, 3.13, 3.14 and 3.15 show the time signal and harmonic amplitudes for both total pressure signal (induced by all flow components) and the pressure fluctuations induced only by TVC.

It can also be seen in Figure 3.12 that the larger the deviation from the equilibrium radius, the more chaotic the pressure signal becomes. This is also reflected in the harmonics amplitude shown in Figure 3.13, i.e. the larger the deviation, the larger the amplitude of the higher-order harmonics. This is more clearly seen when comparing the different deviations for a single time step size as is shown in Figure 3.16 and 3.17. These figures show that the deviation from equilibrium radius mostly influences the higher-order pressure fluctuations ( $2^{nd}$  order and higher) and that the first order harmonic remains almost constant for different deviations. The analysis above shows that the conclusion regarding the appropriate time step size holds for the case of non-equilibrium initial radius as well.

### 3.4 Convergence Study



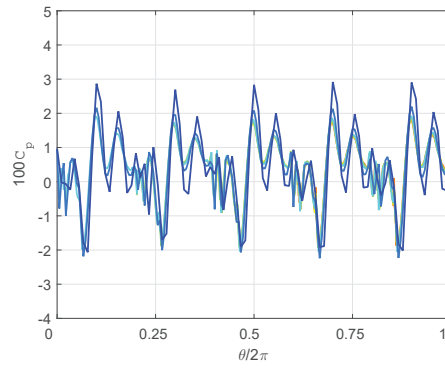
(a) Pressure signal



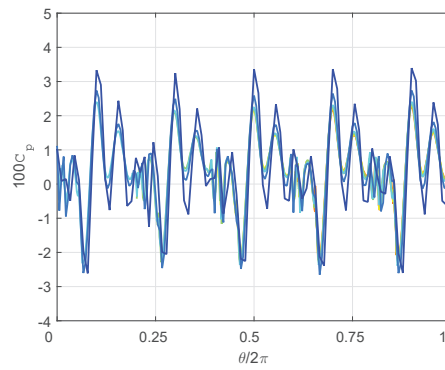
(b) Harmonic analysis

**Figure 3.11:** Pressure time signal induced by the cavitating tip vortex at the off-body point for varying segment sizes ( $\Delta t$ )

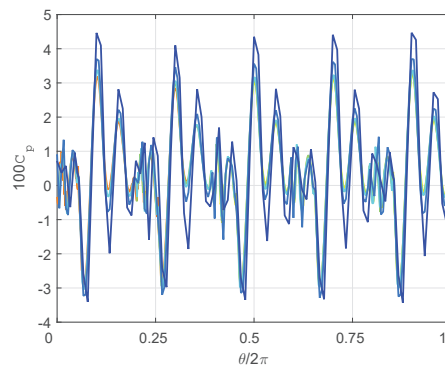
### 3 Numerical Analysis and Verification



(a) 2% Deviation



(b) 5% Deviation



(c) 10% Deviation

**Figure 3.12:** Total pressure time signal for varying deviations from the equilibrium radius

### 3.4 Convergence Study

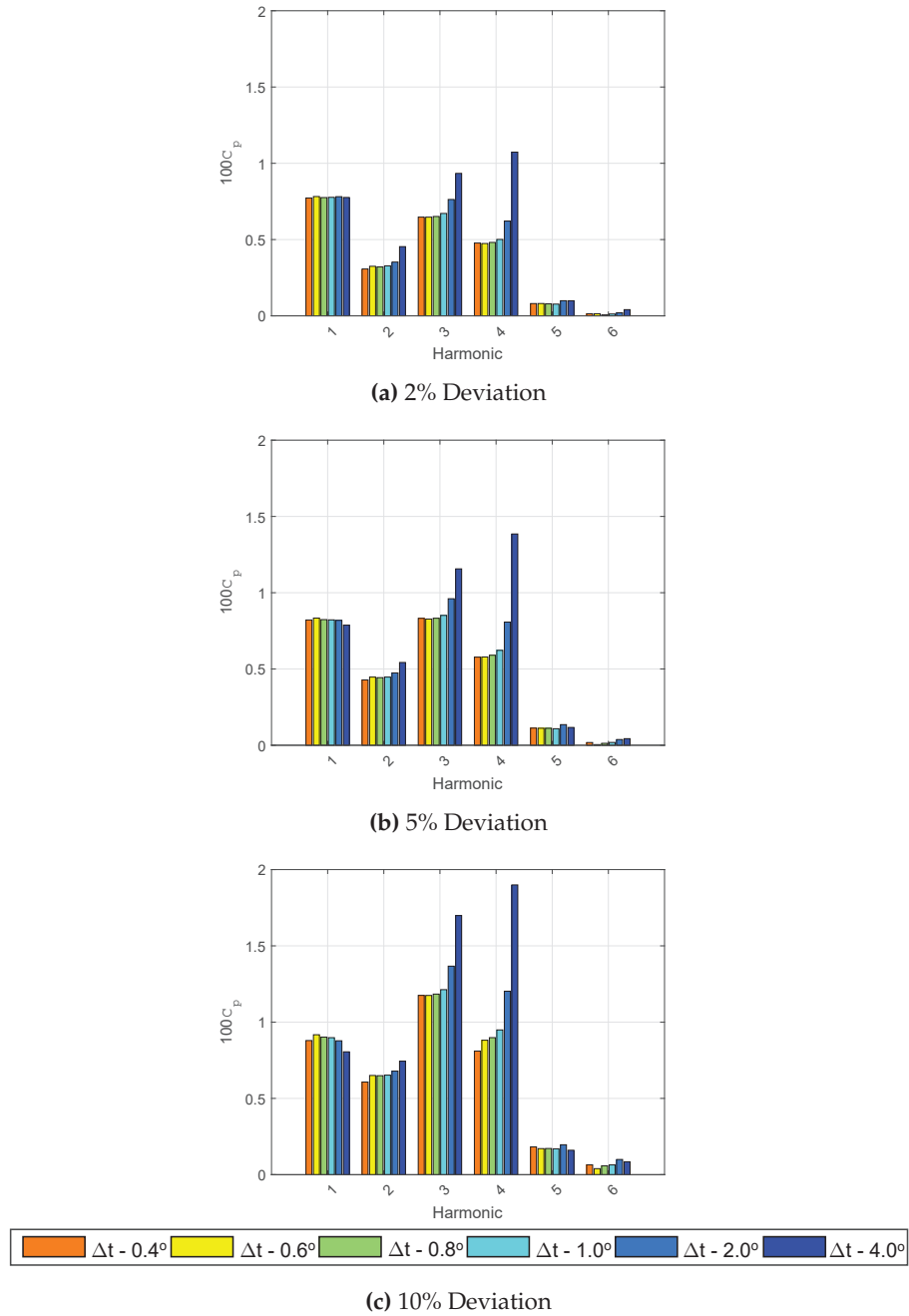
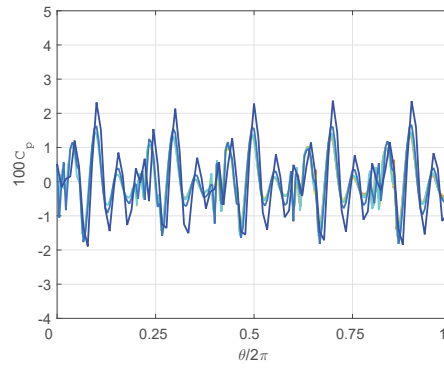
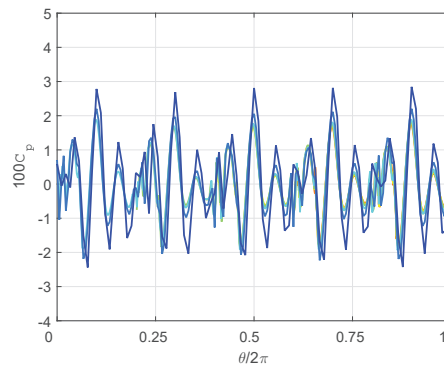


**Figure 3.13:** Total pressure signal harmonics amplitude for varying deviations from the equilibrium radius

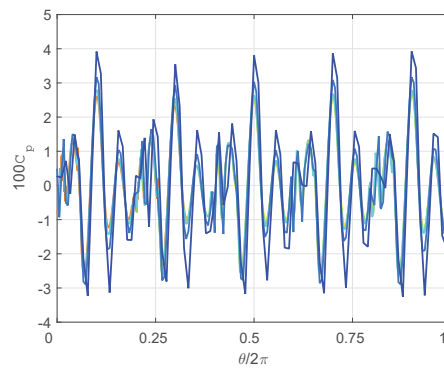
### 3 Numerical Analysis and Verification



(a) 2% Deviation



(b) 5% Deviation



(c) 10% Deviation

**Figure 3.14:** Pressure time signal induced by the cavitating tip vortex for varying deviations from the equilibrium radius

### 3.4 Convergence Study

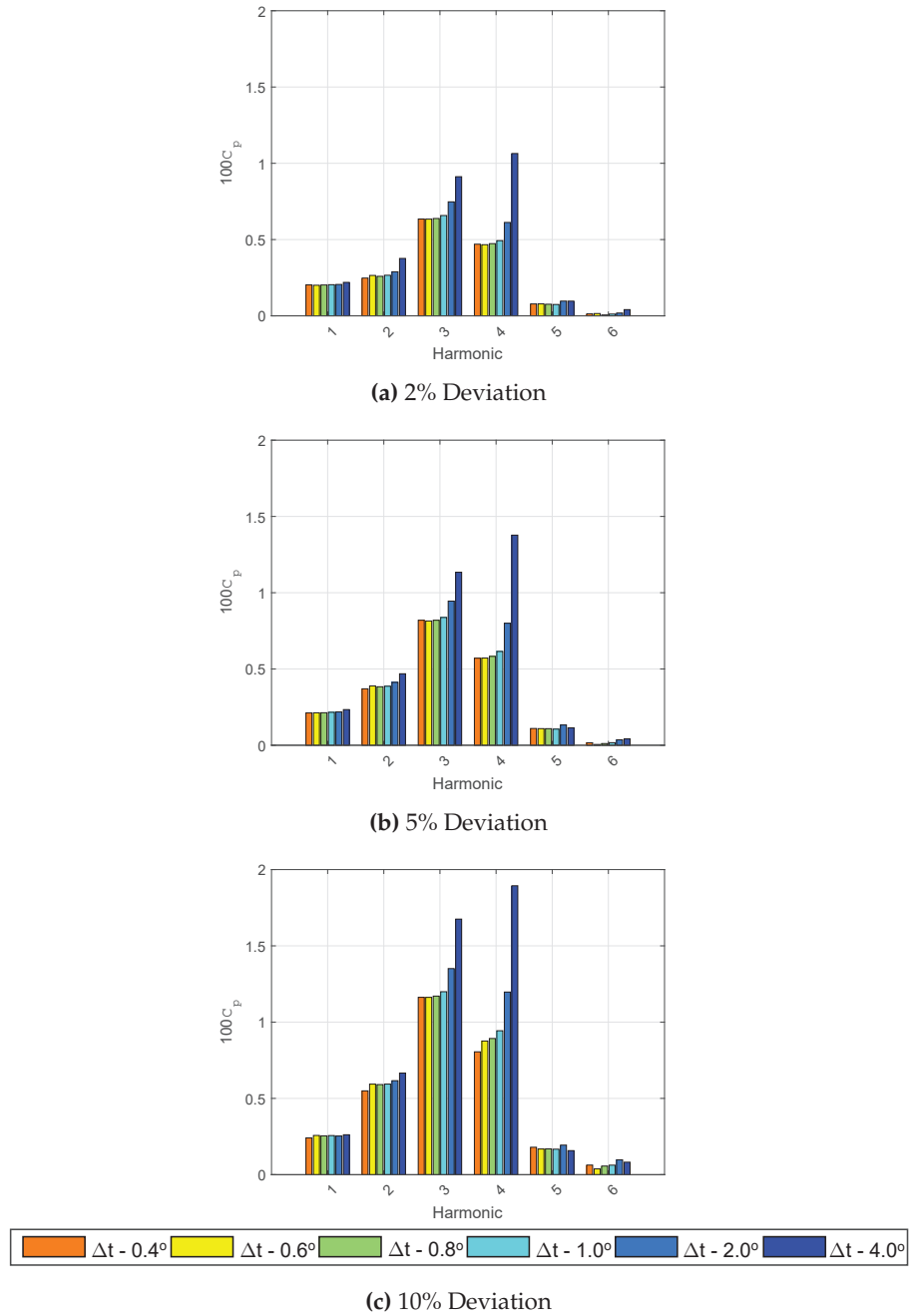
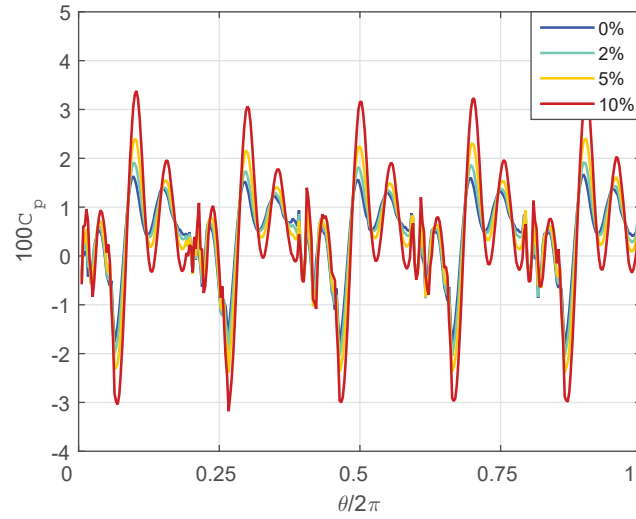
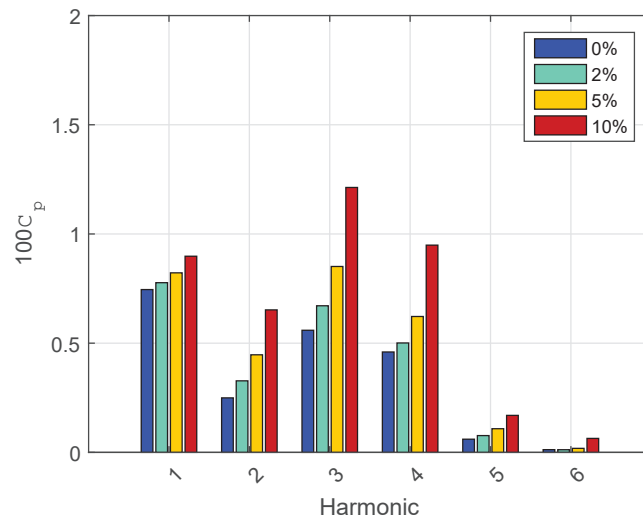


**Figure 3.15:** Amplitudes of the pressure signal induced by the cavitating tip vortex for varying deviations from the equilibrium radius

### 3 Numerical Analysis and Verification



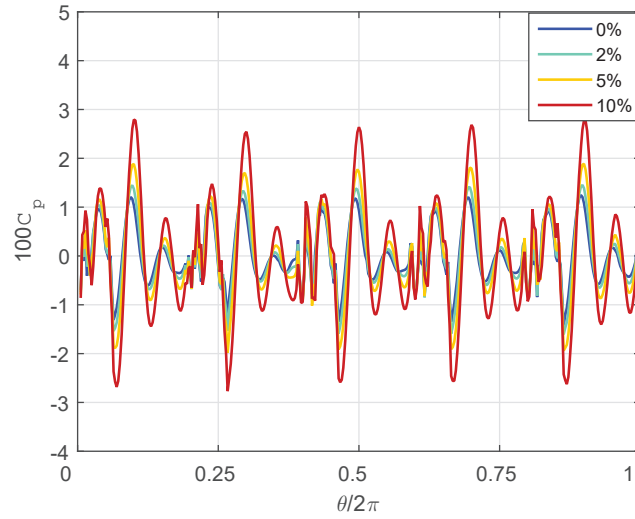
(a) Pressure signal



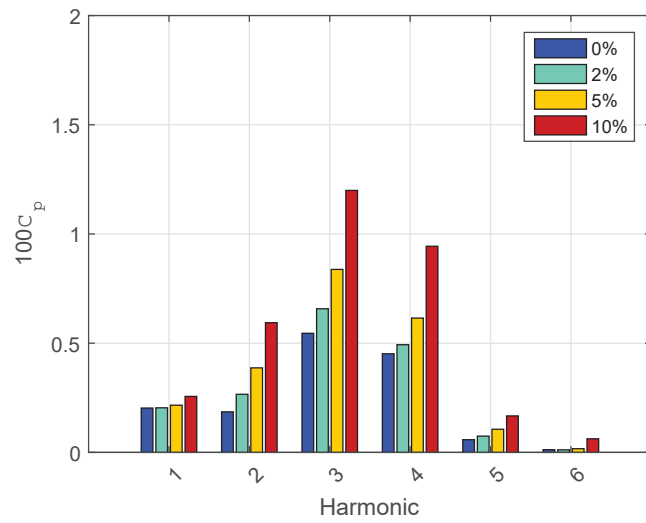
(b) Harmonic analysis

**Figure 3.16:** Total pressure time signal and harmonics amplitudes for  $\Delta t = 1^\circ$  and varying deviations from equilibrium radius

### 3.4 Convergence Study



(a) Pressure signal



(b) Harmonic analysis

**Figure 3.17:** Pressure time signal induced by the cavitating tip vortex and harmonics amplitudes for  $\Delta t = 1^\circ$  and varying deviations from equilibrium radius

### 3.5 Influence of $R_D$ and Growth of the Vortex Strength and Core Size on TVC Dynamic Behaviour

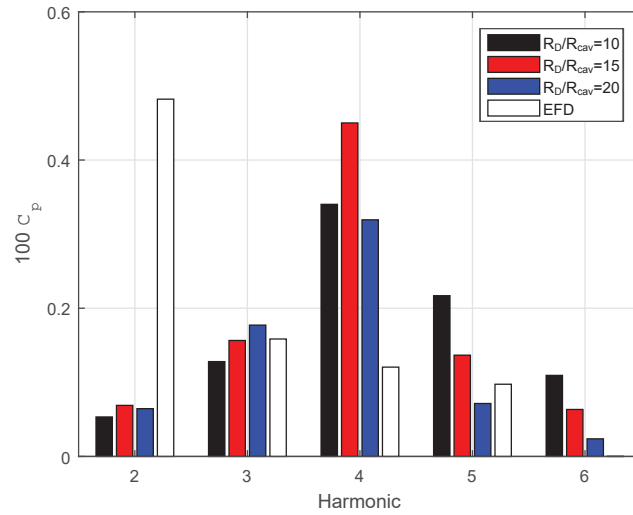
The problem of the outer domain radius ( $R_D$ , see Figure 2.3) has been introduced in Section 2.3.2. As mentioned before, Berger et al. (2016) particularly investigate the influence of this variable on various results of their study and conclude that the choice of this variable must be done with care. They learnt that there is no convergence with increasing  $R_D$  and based on comparing with experimental results an outer domain radius of approximately ten times the average cavitating core radius leads to realistic results for the dynamic behaviour of the vortex cavity.

In this study, the influence of the choice of  $R_D$  on the results is investigated by examining the pressure fluctuations induced at an off-body point directly above the propeller. The purpose of performing a similar study to Berger et al. (2016), is to find out if the results point to the same conclusions regarding the choice of  $R_D$ . To this end, the KCS propeller for which experimental results are available is used. A detailed description of this case is given in Section 4.3. Here, the investigation is performed for both implementations of with and without growth of the vortex strength and the viscous core radius.

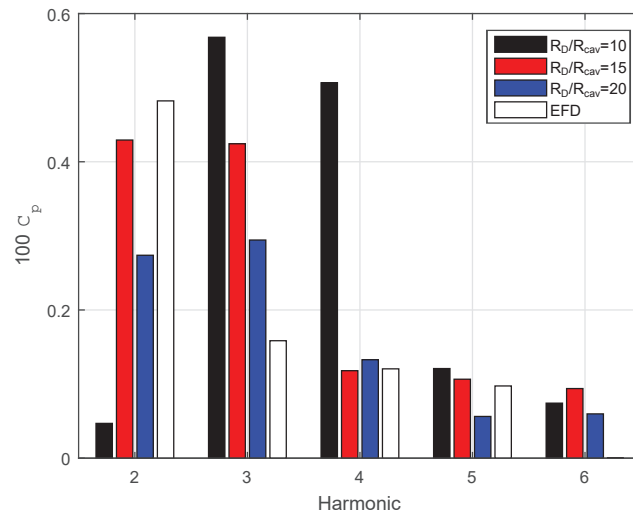
Figure 3.18 shows the amplitude of various harmonics of the pressure induced at a point above the propeller (pick-up P2 in Figure 4.21) for both with and without growth of the vortex strength and the viscous core size. The amplitudes are shown for different ratios between the outer domain radius and the cavitating core radius ( $R_D/R_{cav}$ ). The white bars are the results from the experiment carried out at SVA Potsdam (SVA 2003). In this operating condition and according to the cavitation test results, the propeller has both sheet and tip vortex cavitation. However, it should be noted that the calculation results shown in this figure are without sheet cavitation and only with tip vortex cavitation, which explains the large difference in the second-order oscillation amplitude between the results of the calculations and the experiment.

Looking at the two cases with and without growth of circulation and viscous core size, the difference in results are significant. One can see that the amplitudes are different and the peak occurs at a lower frequency for the case with growth compared to the one without. But the question is at which frequency should the peak occur? To answer this question, the cavitating tip vortex is approximated by a line vortex oscillating around the equilibrium radius as given by Equation 3.4, for which the oscillations frequency is given by (Franc

3.5 Influence of  $R_D$  and Growth of the Vortex Strength and Core Size on TVC Dynamic Behaviour



(a) Without growth of the vortex strength and viscous core radius



(b) With growth of the vortex strength and viscous core radius

**Figure 3.18:** Pressure fluctuations with and without growth of the vortex strength and viscous core size

### 3 Numerical Analysis and Verification

and Michel 2004):

$$f = \frac{1}{T} = \frac{\Gamma}{4\pi^2 R_{cav,eq}^2 \sqrt{\ln(\beta)}} \quad (3.5)$$

where  $\beta$  is  $R_D/R_{cav}$ . Using the definition of cavitation number (Equation 1.1), Equation 2.17 can be rewritten in the following form:

$$\sigma_n = \frac{1}{(2\pi nD)^2} \left( \frac{\Gamma}{R_{cav,eq}} \right)^2 (1 - (1/\beta)^2) \quad (3.6)$$

Dividing Equation 3.5 by 3.6 gives:

$$f = \frac{(nD)^2 \sigma_n}{\Gamma(1 - (1/\beta)^2) \sqrt{\ln(\beta)}} \quad (3.7)$$

Equation 3.7 shows that the frequency of the TVC oscillations is inversely proportional to  $\Gamma$  and the ratio  $\beta$  which is in accordance with the results shown in the Figure 3.18. Approximating the blade bound circulation by the following expression (Isay 1991):

$$\Gamma_b \approx \frac{1}{\kappa} \frac{32}{\pi^2} \frac{K_T}{Z} nD^2 \quad (3.8)$$

and  $\beta = 20$  (as it gives more realistic results based on Figure 3.18b), the frequency of TVC oscillations appears to be approximately three times the blade passing frequency ( $nZ$ ). In this expression,  $\kappa = 1.7-1.9$  and depends on the blade shape,  $K_T$  is the thrust coefficient,  $Z$  is the number of blades,  $n$  is the propeller speed and  $D$  is the propeller diameter.

This investigation reveals that the results with growth of vortex strength and viscous core radius and an outer domain radius approximately twenty times larger than the cavitating core radius are more reasonable and as also concluded by Berger et al. (2016), the results do not converge with increasing  $R_D$ .

## 4 Application to Marine Propellers

In this chapter the results of four different studies are presented. The inception of tip vortex cavitation for a submarine propeller is predicted using the two methods described earlier in Section 2.2. This propeller is selected for this purpose because inception of cavitation is important for submarine propellers. In addition, measurement data in form of margin against tip vortex cavitation inception at different cavitation numbers are available in this case. The two methods of Section 2.2 are used for predicting the inception and the results of the two methods are compared with each other and with experimental data.

INSEAN E779a propeller, a well-known test case, is then simulated in uniform inflow in non-cavitating and cavitating conditions. This study focuses on validating the calculation results for propeller forces, pressure distribution on the surface of the blade and cavity extent against experimental and other numerical data available to the public.

Next, the results for the KRISO container ship propeller (KCS), also a well-known test case, are presented. This propeller has been tested at SVA Potsdam and results for propellers forces, cavitation extent and pressure pulse measurements are available. According to cavitation test results, this propeller develops a stable sheet cavity that rolls up into a tip vortex cavitation and therefore, it is a proper test case for validation of TVC calculation results.

Last but not least, two propellers designed for a modern bulk carrier are used to investigate the effect of hull Reynolds number on cavitation behaviour of propellers. These propellers have also been used in Regener et al. (2017), however in this work, the study is extended to include tip vortex cavitation and the focus is on the influence of wake field *distribution* on the dynamics of tip vortex cavitation and the resulting pressure fluctuations.

### 4.1 Study on Tip Vortex Cavitation Inception

In this section, results from model tests with a submarine propeller of the Kappel type are used for validation of the two methods for predicting tip vortex cavitation inception described in Section 2.2.

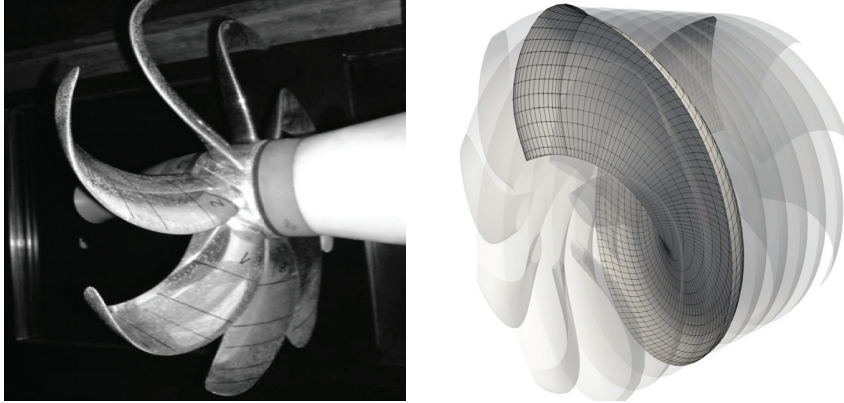


**Figure 4.1:** Kappel propeller model geometry and the panel code input geometry

#### 4.1.1 Case Study

The submarine propeller used here is an eight-bladed Kappel propeller designed within a propeller design development program for a particular submarine case. The propellers were tested at Potsdam Model Basin (SVA), Germany in open water and behind a dummy model of the submarine (for more details see Andersen et al. (2009)). Figure 4.1 shows the propeller used for model testing and the geometry input to the panel code. The wake of the submarine is shown in Figure 4.2.

#### 4.1.2 Cavitation Inception Diagram

A cavitation inception diagram usually illustrates the cavitation number at which cavitation starts to occur as a function of  $K_T$  or  $J$ . However, here the results are presented as relative margin against cavitation as a function of submergence, see Figure 4.3. In this figure,  $K_T$  is the design thrust coefficient, and  $\Delta K_T$  is the difference between design thrust coefficient and the thrust coefficient at which cavitation starts. This way of presenting the results is motivated by the fact that for the case of submarine propellers and according to the design objectives defined within the design program, the propeller must be totally free of cavitation with an adequate margin.

As described in Section 2.2, there are two approaches to predict inception of tip vortex cavitation, comparing local minimum pressure and vapour pressure and the bubble growth approach. Both of these approaches depend on a reliable prediction of the vortex strength and the viscous core radius at the

#### 4.1 Study on Tip Vortex Cavitation Inception

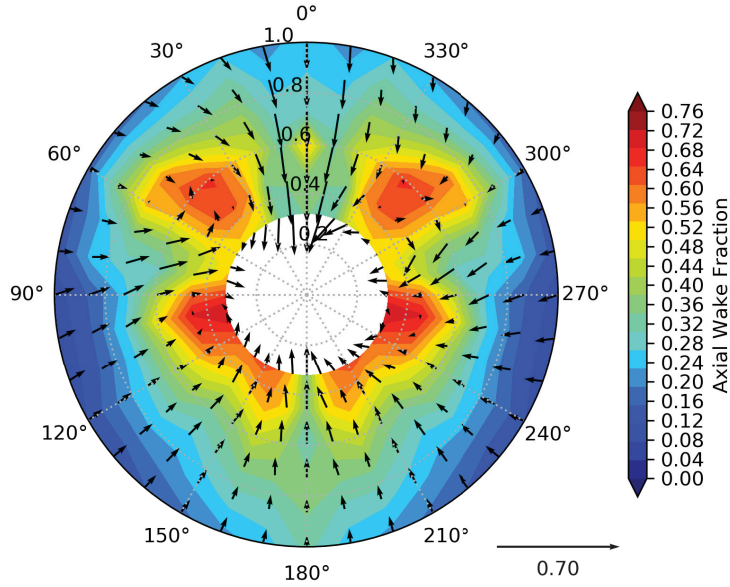


**Figure 4.2:** Wake field of the submarine

tip. As discussed previously and according to Equation 2.2, the viscous core radius is related to the boundary layer thickness at the tip. However, since the potential flow method is not able to compute this parameter, the model has to be calibrated using experimental or viscous flow calculations. For this purpose, a calibration factor  $\tau$  is defined and the viscous core radius is written as:

$$R_c = \tau \sqrt{\delta C_{0.95R}} \quad (4.1)$$

where  $\delta$  is the boundary layer thickness obtained by Equation 2.2 and  $C_{0.95R}$  is the chord length at  $r/R = 0.95$ . The calibration factor is in general not constant and is dependent on the thrust coefficient. Berger (2018) carried out a study on the dependency of vortex parameters such as ratio between initial circulation of the tip vortex and bound circulation as well as viscous core radius. He also came to the conclusion that these parameters are not constant but change with the blade load.

Here, the first and last data points of the measured inception curve shown in Figure 4.3 are used for calibration. The procedure employed for calibration assumes that cavitation occurs at the point of minimum pressure and

#### 4 Application to Marine Propellers

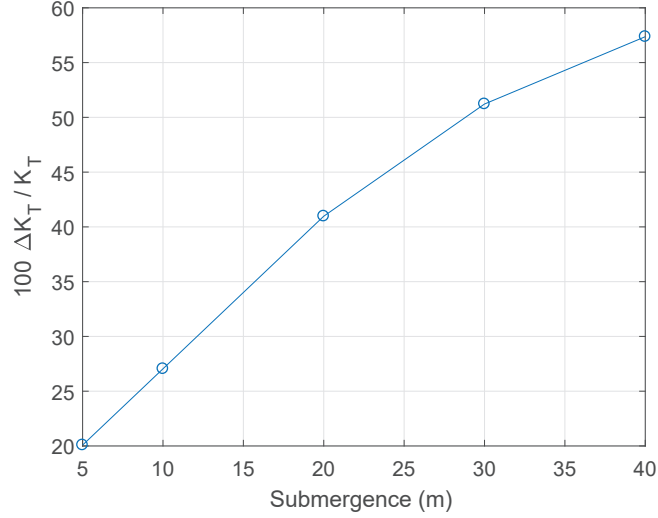


**Figure 4.3:** Measured relative margin against tip vortex cavitation

when pressure is equal to the vapour pressure (engineering criterion). Using Equation 2.9, the inception cavitation number can be written as:

$$\sigma_i = \frac{1}{2\pi^2 (nD)^2} \left( \frac{\Gamma}{R_c} \right)^2 \quad (4.2)$$

The problem is now reduced to finding the factor for the model (Eq. 4.1 and 4.2) that best fits the data from the experiment at the two end points. Here, the circulation is taken at a fixed position along the blade span, i.e. at  $r = 0.97R$ . For the remainder of the operating points the factors are found by linear interpolation between the factors found for the first and last data points.

The simulated inception curve based on the engineering criterion is shown in Figure 4.4. It can be seen that the predictions for the remainder of the operating points are in good agreement with the experimental data.

For the bubble growth approach a release zone with a radius equal to four times the viscous core radius is considered where 500 cavitation nuclei with randomly generated size and location are distributed. For these bubbles, an average radius of  $100 \mu m$  and a minimum radius of  $10 \mu m$  are assumed. Using Equation 4.1 to calculate the viscous core radius and taking the circulation at  $r = 0.97R$ , the simulation is initialized with bubbles at their initial position and with their initial radius and they are then monitored for unbounded growth.

#### 4.1 Study on Tip Vortex Cavitation Inception

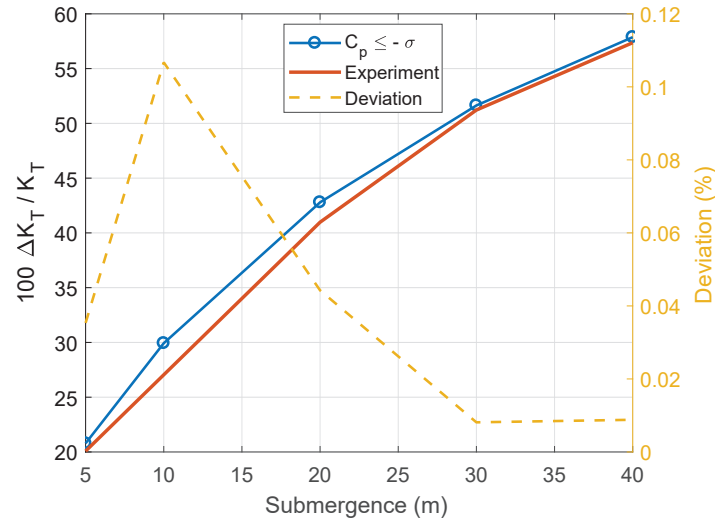


**Figure 4.4:** Relative cavitation margin predicted by the engineering criterion, Eq. 2.8, and compared to the experimental results

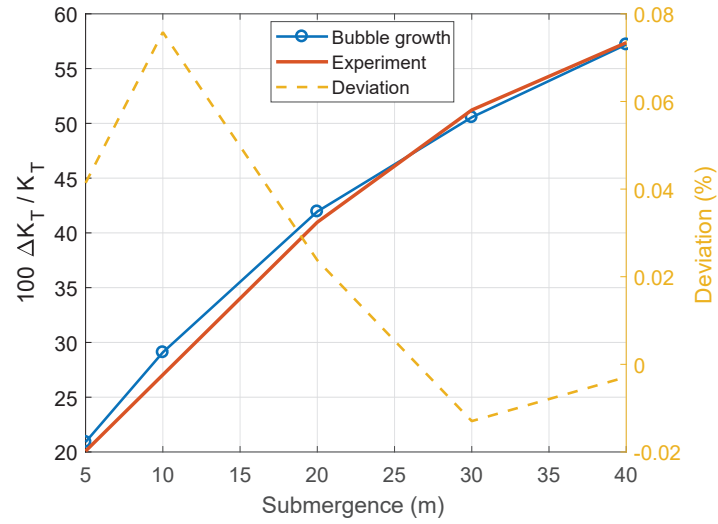
Unbounded growth is signalled when the radius of at least one of the bubbles reaches fifty times its initial radius.

Figure 4.5 shows the relative margin against tip vortex cavitation predicted by this approach and compared to the model test results. Comparison of the predictions of the two methods is shown in Figure 4.6. The results of both methods are very similar with the bubble growth approach being the more conservative of the two, i.e. predicting smaller margin against cavitation. A similar study carried out by Hsiao et al. (2000) also shows that the bubble growth method predicts larger inception cavitation number compared to the engineering criterion.

To investigate the influence of input parameters on the results of the bubble growth method, a set of simulations with varying inputs for number of bubbles and bubbles average radius were performed. Figure 4.7 shows the variations considered for this parameter study.

The effect of varying the number of bubbles on the cavitation margin is shown in Figure 4.8, where the results for variation 2 to 7 are plotted and compared with the engineering criterion for each submergence. Simulation with only one bubble (variation 1 in Figure 4.7) shows no inception of tip vortex cavitation for all submergence values and simulation with ten bubbles, shows no inception at submergence of 30 and 40 m. One can see that with increasing

#### 4 Application to Marine Propellers



**Figure 4.5:** Relative cavitation margin predicted by the bubble growth method and compared to the experimental results

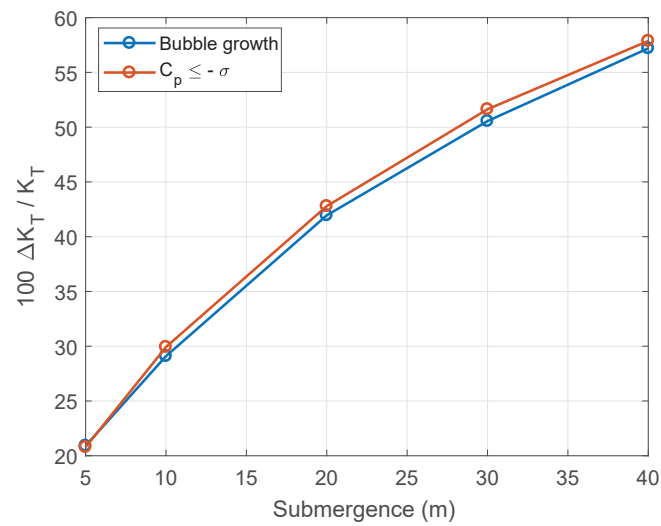


**Figure 4.6:** Comparison of bubble growth and engineering criterion results for the inception of tip vortex cavitation

## 4.2 INSEAN E779a Propeller in Uniform Inflow Conditions

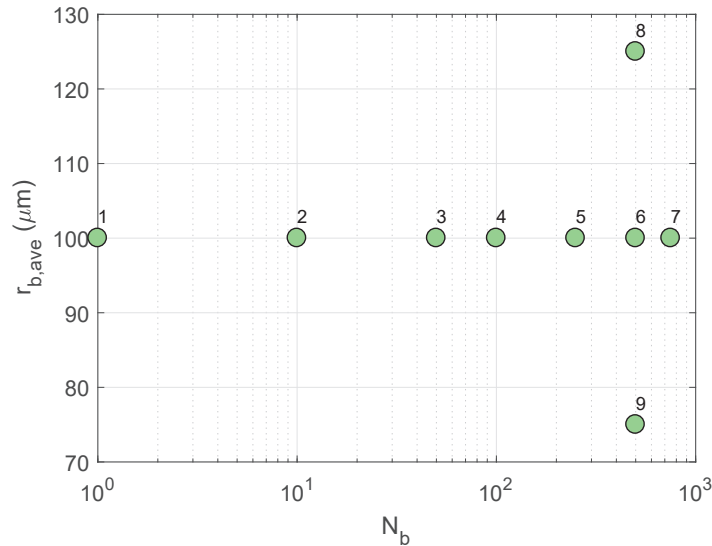


**Figure 4.7:** Variations simulated as part of sensitivity analysis of the bubble growth approach to input parameters

the number of bubbles, the predicted margin against cavitation decreases and converges at around 250 bubbles.

Varying the bubbles average radius (variation 6, 8 and 9 in Figures 4.7) has a rather minor influence on the results. These results are shown in Figure 4.9 for each submergence. In these simulations the minimum radius of the bubble has been limited to  $10 \mu\text{m}$  to avoid numerical instabilities.

## 4.2 INSEAN E779a Propeller in Uniform Inflow Conditions

In this section, the well-known benchmark case INSEAN E779a propeller operating in uniform inflow condition is used for validation purposes. The E779a propeller is chosen because it has been the subject of many studies and there are large amounts of experimental and numerical data available to the public. For instance, at the First International Symposium on Marine Propulsors in 2009 (SMP-2009), the results from the “VIRTUE 2008 Rome Workshop on Modelling Propeller Cavitation” were presented. There, seven computational models are compared using the E779a propeller as test case in uniform and

#### 4 Application to Marine Propellers

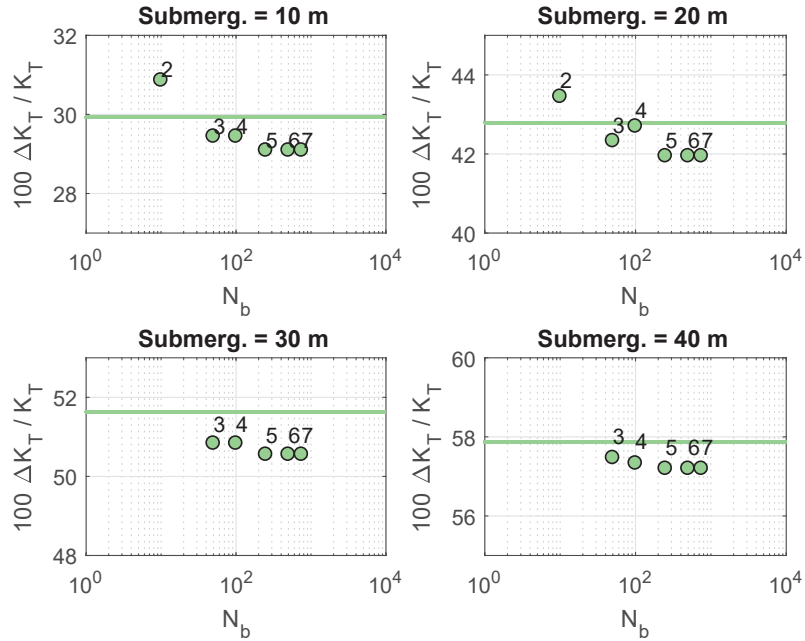


**Figure 4.8:** Influence of number of bubbles on the inception prediction by bubble growth. • indicates the prediction by bubble growth method and solid line shows the prediction based on the engineering criterion

non-uniform inflow conditions (Salvatore et al. 2009).

Later at the Fourth International Symposium on Marine Propulsors in 2015 (SMP-2015), Vaz et al. (2015) presented the results obtained for the same propeller simulated in open water and in behind condition by ten different institutions as part of the SHARCS (*Ship Hydrodynamic Advanced RANS Cavitation Simulations*) working-group with the aim of investigating the performance of the state-of-the-art CFD tools for predicting pressure fluctuations on ships due to cavitating propellers.

Among more recent studies using E779a propeller as a test case, one can refer to Perali et al. (2016), Yilmaz et al. (2017) and Lloyd et al. (2017) where in the two latter attempts have been made to improve the prediction of the tip vortex cavitation as well.

## 4.2 INSEAN E779a Propeller in Uniform Inflow Conditions

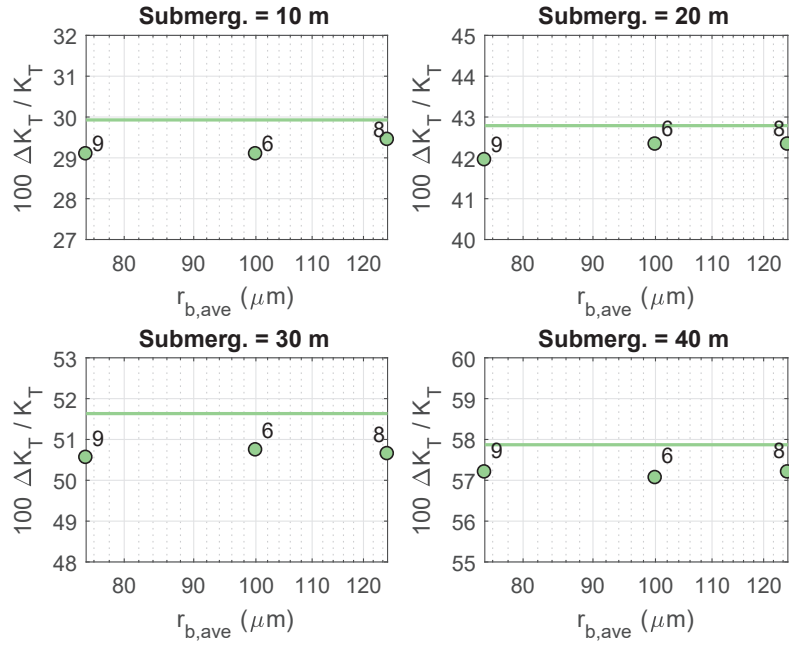


**Figure 4.9:** Influence of average bubble radius on the cavitation margin. ● indicates the prediction by bubble growth method and solid line shows the prediction based on the engineering criterion

### 4.2.1 Propeller Geometry and Test Case Setup

The E779a propeller is a fixed-pitch, four-bladed, right-handed propeller with low skew designed in 1959 (INSEAN 2006). Figure 4.10 shows the model geometry and the geometry description used for ESPPRO simulations generated based on the data given in INSEAN (2006). The model propeller diameter is  $D = 227.27 \text{ mm}$  with nominal pitch ratio of  $P/D = 1.1$  that is almost constant in radial direction.

The operating condition that is mostly used by other studies and therefore also considered here is uniform inflow velocity of  $V_{in} = 5.81 \text{ m/s}$  and propeller speed of  $n = 36.0 \text{ s}^{-1}$  which corresponds to an advance ratio of  $J = 0.71$ . For the cavitating flow condition, a cavitation number of  $\sigma_n = 1.763$  is considered.

## 4 Application to Marine Propellers

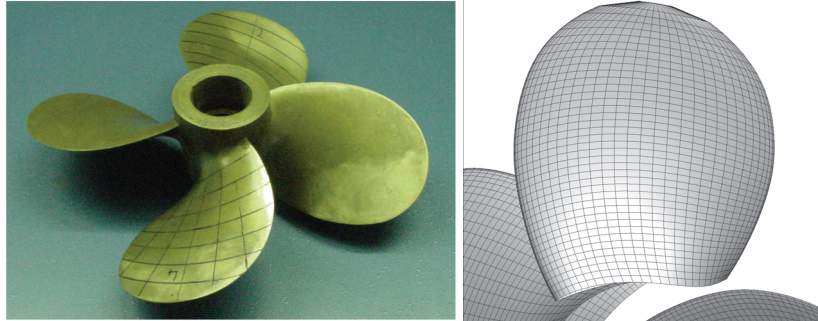


Figure 4.10: E779a model geometry and the panel code geometry input

### 4.2.2 Open Water Diagram

The calculated open water performance of the propeller is shown in Figure 4.11 where it is also compared to the experimental data and to the numerical results presented in Vaz et al. (2015). Comparing ESPPRO results and the results from experiment, at the nominal  $J$  value of 0.71, it can be seen that  $K_T$  is over predicted by 2% while  $K_Q$  is under predicted by 2%. This results in an over prediction of the open water efficiency by 4%. However, at lower  $J$  values the difference between the results are larger especially for  $K_Q$ , which can be expected because of the simple wake alignment approach and simple approximation of the blade friction by ESPPRO. Since the agreement between the results is good at the nominal  $J$  value, the propeller is used for further analysis and validation in non-cavitating and cavitating conditions.

Referring to Figure 4.11, Vaz et al. (2015) show that the averaged differences when comparing the numerical results and the results from experiment are lower than 5%. It can be seen that the potential flow code (PROCAL v2.2), has over predicted  $K_Q$  at all advance ratios while  $K_T$  is consistently well predicted. These predictions have led to an open water efficiency curve which is different in shape and magnitude especially close to and at the peak.

### 4.2.3 Sectional Pressure Distribution

Figures 4.12a and 4.12b show results from ESPPRO for pressure distribution in the chord-wise direction at two radial sections of  $0.7R$  and  $0.9R$  for both non-cavitating and cavitating conditions. The Lloyd et al. (2017) results using CFD code *ReFRESH* are also shown in Figure 4.12b for comparison.

Comparing ESPPRO results with results from Lloyd et al. (2017) for  $r/R = 0.9$ , Figure 4.12b, one can see that the difference is limited to the vicinity of the

## 4.2 INSEAN E779a Propeller in Uniform Inflow Conditions

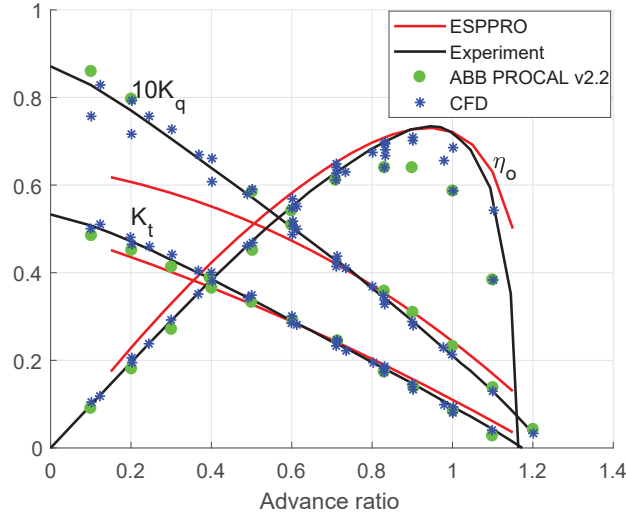


**Figure 4.11:** Open water curve for wetted flow condition  $J = 0.71$ . CFD results refer to the results presented in Vaz et al. (2015)

trailing edge (the last 20 – 30% of the chord length) which can be caused due to using a linear Kutta condition.

For the cavitating condition, however, differences are slightly more pronounced. For instance, ESPPRO predicted a sharper leading edge pressure drop and the cavity extent is smaller (cavity extends up to  $\approx x/c = 0.65$ ) before the pressure begins to recover, while the CFD results show an extent of all the way to  $x/c = 0.8$ . The pressure distribution abaft the cavity and up to the trailing edge is different as well. However, both models have obtained  $-C_{pn} = \sigma_n$  for the cavitating part of the section. In general, there seem to be a good agreement between the methods and the differences are mainly due to differences that are inherent to each method.

### 4.2.4 Surface Pressure Distribution

The ESPPRO results for the surface pressure distribution are compared qualitatively to the *ReFRESH* and the PROCAL v2.2 results in Figures 4.13 and 4.14 for both non-cavitating and cavitating conditions, respectively (Lloyd et al. 2017, Vaz et al. 2015). There seems to be an overall good agreement between the methods. Differences are mainly as discussed in the section above with the addition that there are differences in regions close to the root and that can be

## 4 Application to Marine Propellers

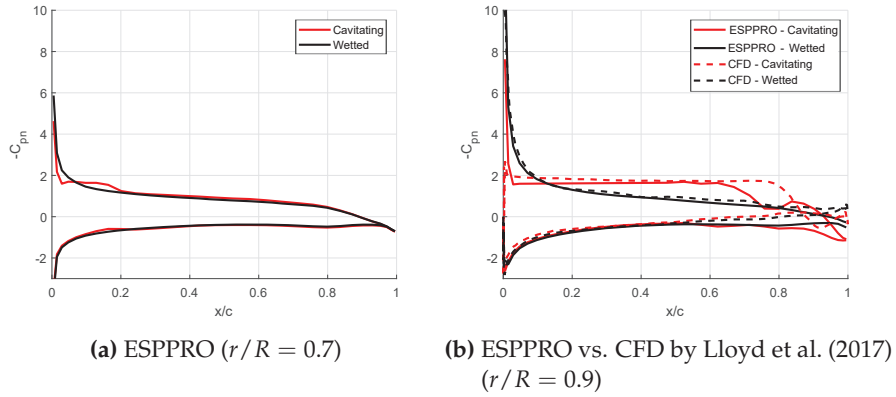


**Figure 4.12:** Open water sectional pressure distribution for both wetted and cavitating flow conditions -  $J = 0.71$  and  $\sigma_n = 1.76$

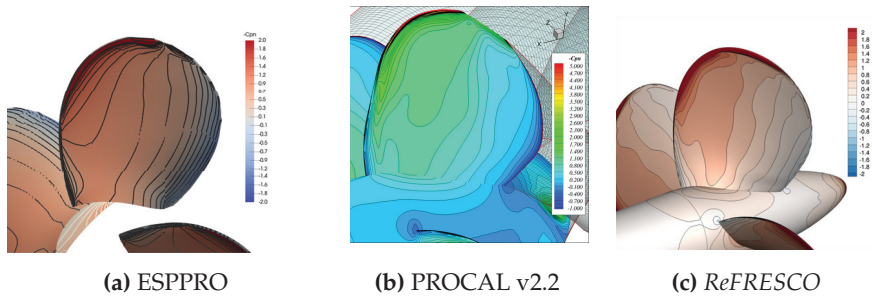


**Figure 4.13:** Propeller surface pressure distribution ( $-C_{pn}$ ) in wetted flow condition  $J = 0.71$

caused by the absence of a hub model in ESPPRO.

### 4.2.5 Cavity Extent

The results of the cavitation extent predicted by ESPPRO is presented and compared qualitatively to other methods and experiment in Figure 4.15 for  $J = 0.71$  and  $\sigma_n = 1.76$ . The agreement between the computational results and the experiment is considered good for sheet cavitation extent. However, one can see that the tip vortex cavitation is missing in PROCAL v2.2 results (due to lack of a model for capturing TVC), and in the *ReFRESKO* results although the tip vortex cavitation is captured, the extent seems to be shorter than in the

4.2 INSEAN E779a Propeller in Uniform Inflow Conditions

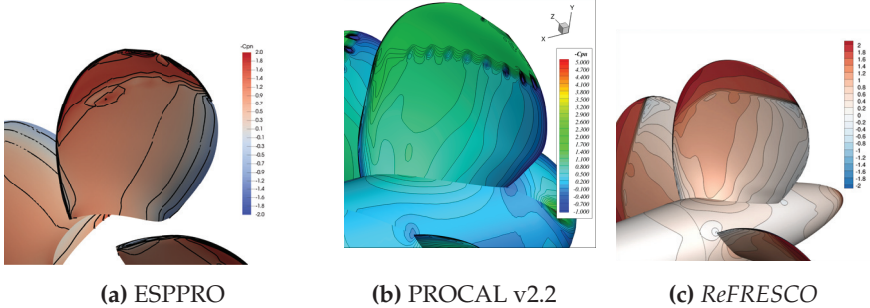


Figure 4.14: Propeller surface pressure distribution ( $-C_{pn}$ ) in cavitating flow condition  $J = 0.71$  and  $\sigma_n = 1.76$

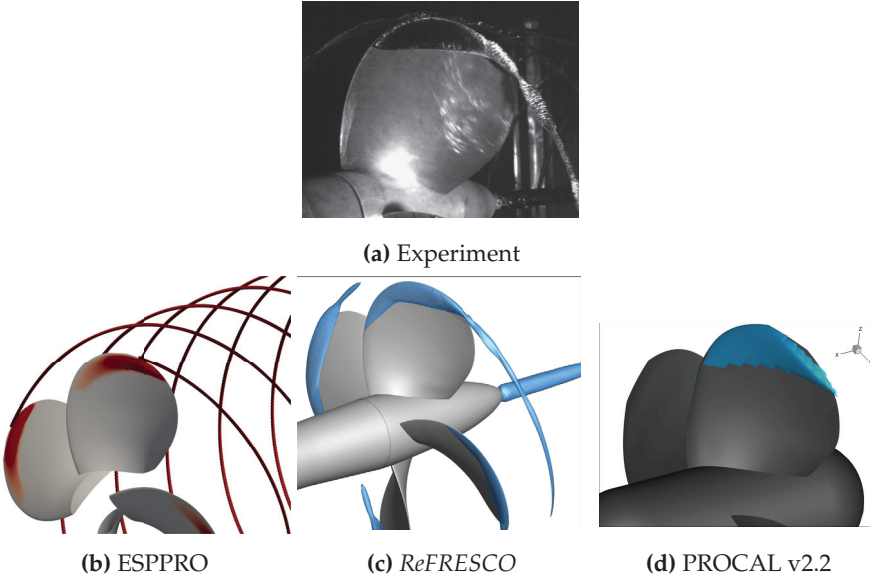


Figure 4.15: Open water cavity extent  $J = 0.71$  and  $\sigma_n = 1.76$

experiment. Tip vortex cavitation is captured by ESPPRO and the radius of the cavity core and the extent are in good agreement optically with the experimental results. The roll-up of the sheet cavitation into the cavitating tip vortex (as can be seen in the experimental results) is not captured by ESPPRO. The reason is the simple criterion for the selection of the initial radius of the cavitating segments explained in Section 2.3.1.

## 4 Application to Marine Propellers

**Table 4.1:** KRISO container ship hull and propeller particulars (SVA 2003)

<i>Ship</i>			
Length between perpendiculars	$L_{pp}$	m	7.278
Draught	$T$	m	0.342
Breadth	$B$	m	1.019
Scale ratio	$\lambda$	-	31.59
<i>Propeller</i>			
Diameter	$D$	m	0.25
Pitch ratio	$P/D_{0.7R}$	-	0.9967
Number of blades	$Z$	-	5
Hub ratio	$r_{hub}/R$	-	0.18
Area ratio	$A_e/A_o$	-	0.8

Based on the above analysis, the agreement between the ESPPRO results and the results from the experiment or other research studies is good. The differences exist mainly due to the fundamental assumptions and simplifications in each method. For example, the propeller performance predicted by ESPPRO (or in general any panel method) is significantly influenced by the blade trailing wake model and the prediction of the blade friction especially at lower  $J$  values. In addition, the cavitating blade pressure distribution is influenced by the choice of the pressure recovery law in sheet cavitation model. Also, the Kutta condition plays an important role in the sectional pressure distribution especially close to the trailing edge. With regards to the tip vortex cavitation model, the choice of the initial radius, which in this work is done by simple criterion of Eq. 2.18, affects capturing of the interaction between sheet and tip vortex cavitation and thus the dynamics of the cavitating tip vortex.

### 4.3 KCS Propeller in Non-Cavitating and Cavitating Flow Conditions

The KRISO container ship (KCS) has been used as a test case for many numerical studies including CFD workshops over the years. KCS is a single screw modern container ship which only exists in model scale. The ship hull and the propeller particulars are listed in Table 4.1.

SVA Potsdam has carried out propeller open water and cavitation tests with two different dummy models of the KRISO container ship. The difference between the two models are in the additional wires (mesh screens) used at the aft-body. The addition of the screens is to mimic the right model and

### 4.3 KCS Propeller in Non-Cavitating and Cavitating Flow Conditions

**Table 4.2:** KCS operation conditions (Full scale refers to the wake field and the Reynolds number)

		<i>Model scale</i>	<i>Full scale</i>
Velocity	m/s	5.338	5.415
Propeller speed	rps	30.000	30.027
J	-	0.712	0.721
$K_T$	-	0.172	0.170
$K_Q$	-	0.287	0.288
$\sigma_n$ (non-cavitating)	-	6.634	6.623
$\sigma_n$ (cavitating)	-	1.489	1.487
$Re$	-	$1.479 \times 10^7$	$2.387 \times 10^9$

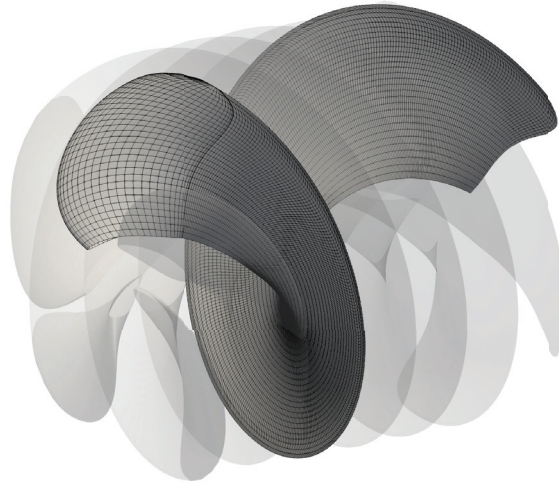


**Figure 4.16:** KCS blade and trailing wake geometry

full-scale ship wake distributions (SVA 2003). The results of these model tests are used here as a basis for the validation of the simulation results. The two different operation conditions used in this study corresponding to model and full-scale flow conditions used by SVA Potsdam are given in Table 4.2. For the calculations here, a model propeller is run in both model and full-scale wake field distributions (Figure 4.18e and 4.18f) using the corresponding operation conditions listed in Table 4.2. The geometry of the propeller blade and the blade trailing wake are shown in Figure 4.16.

## 4 Application to Marine Propellers

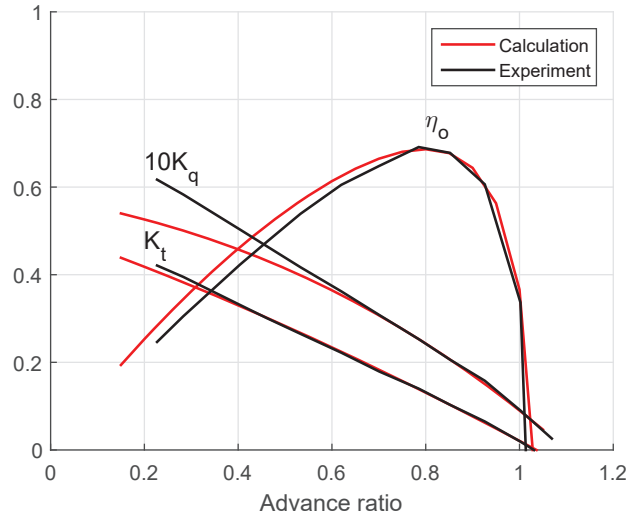


**Figure 4.17:** Comparison of open-water performance - calculation and experiment

### 4.3.1 Propeller Open-Water Characteristics

In Figure 4.17  $K_T$ ,  $K_Q$  and  $\eta_o$  results between calculation and experiment in an open-water diagram are compared (SVA results are with  $n = 15$  rps). It can be seen that  $K_T$  is predicted well over the entire range of advance ratios.  $K_Q$  however, falls below the experimental results for low  $J$  values which again can be expected due to very simple modelling of blade frictional forces and simple trailing wake model. This in turn results in over-prediction of the open water efficiency at lower  $J$  values. At nominal  $J$  value of 0.721, the error is 2% on  $K_T$  and  $\eta_o$  while  $K_Q$  is predicted with almost zero deviation.

### 4.3.2 Unsteady Analysis in Non-Cavitating Flow condition

Figure 4.18 shows six wake fields, arranged in two columns and three rows. The left column corresponds to the model-scale and the right column to the full-scale condition. The first row, Figures 4.18a and 4.18b, are the measured model-scale and estimated full-scale wake fields provided by SVA. The second row, Figures 4.18c and 4.18d, are the calculated nominal wake fields, and the last row, Figures 4.18e and 4.18f, are the calculated effective wake fields.

The effective wake fields are determined using the RANS-BEM coupling

### 4.3 KCS Propeller in Non-Cavitating and Cavitating Flow Conditions

approach at model and full scale. RANS-BEM coupling is an approach where Reynolds-averaged Navier-Stokes equations are solved for the hull while the propeller is represented by body forces provided by the boundary element method. The effective wake field distribution is obtained in an iterative process and the details can be found in e.g. Rijpkema et al. (2013). For this study, commercial SHIPFLOW XCHAP solver is used on the RANS side where the steady-state RANS equations are solved using the finite volume method on structured grids. Also, the EASM (Explicit Algebraic Stress Model) turbulence model is employed. The same RANS solver is used to determine the nominal wake fields at model and full scale, however, the propeller model is switched off.

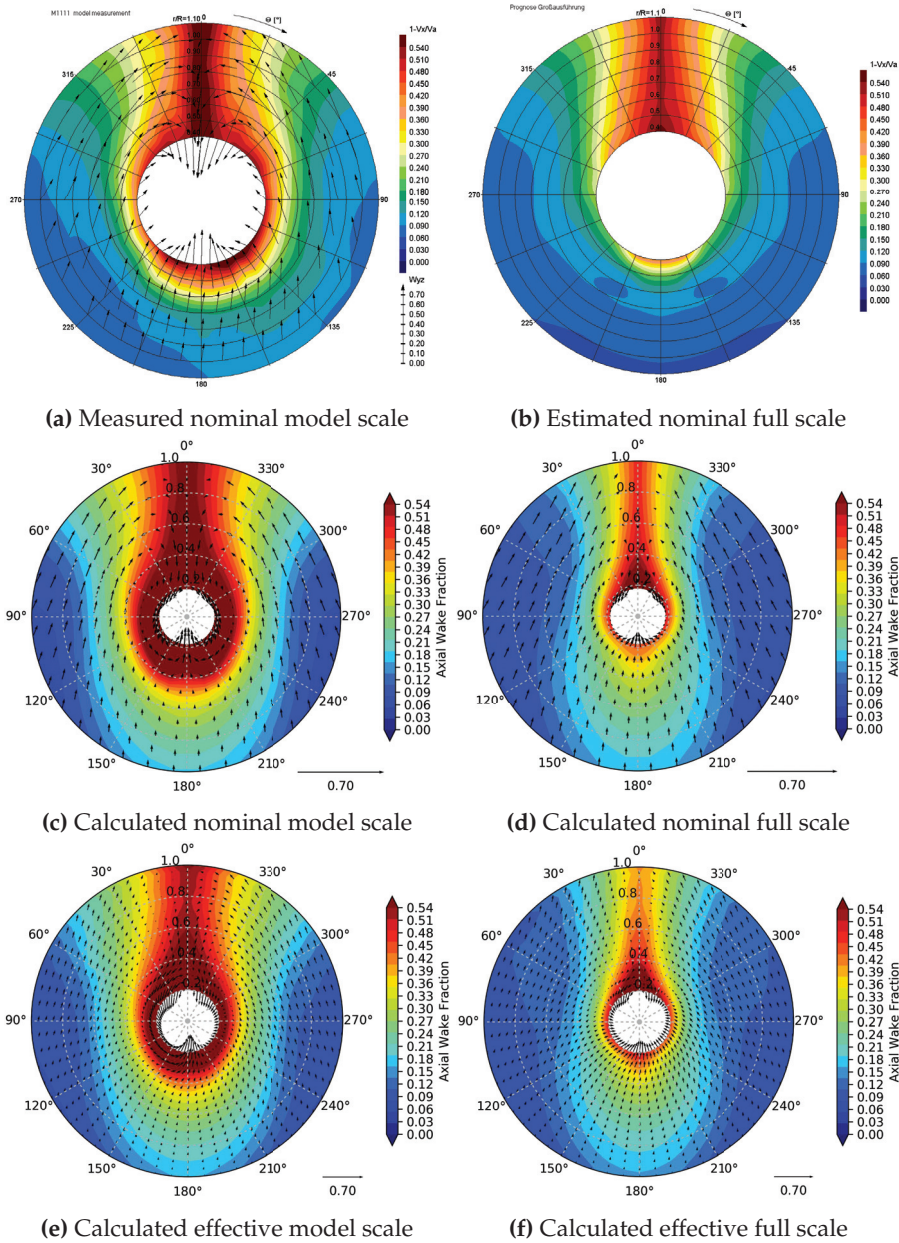
As can be seen, the qualitative agreement between the measured (estimated) and calculated nominal wake fields are good both for the axial velocities and also the in-plane velocity components. Since the agreement between the results for nominal flow fields are good, it is assumed that the effective wake fields are also a good approximation of the actual effective fields in model and full scale and therefore, are suitable to be used for further study of the propeller performance and cavitation behaviour.

Figure 4.19 shows the propeller loads when running in behind condition for both model and full-scale effective wake fields. According to the experimental results,  $K_T$  and  $10K_Q$  are respectively 0.174 and 0.288 in model-scale wake and, 0.173 and 0.292 in full-scale wake. The average values for  $K_T$  and  $10K_Q$  obtained by the simulations are in good agreement with these results. The average  $K_T$  and  $10K_Q$  values are 0.1701 (2%) and 0.2857 (0.8%) in model-scale wake and 0.1709 (1.2%) and 0.2904 (0.5%) in full-scale wake (figures in parentheses are the absolute deviation from the experimental results).

Figure 4.20 shows the blade surface pressure distribution in the form of  $-C_{pn}$  (for model-scale condition). Results from ESPPRO calculations are shown in the top row and results from SVA viscous flow calculations taken from the report (SVA 2003) are shown in the bottom row. It can be seen that the agreement between the results of the two calculation methods is good. In the non-cavitating condition, as the blade passes the low velocity region around 12 o'clock position, the low pressure region on the surface of the blade grows from being limited to the vicinity of the leading edge only and in the mid-span area to a larger extent while moving up towards the blade tip.

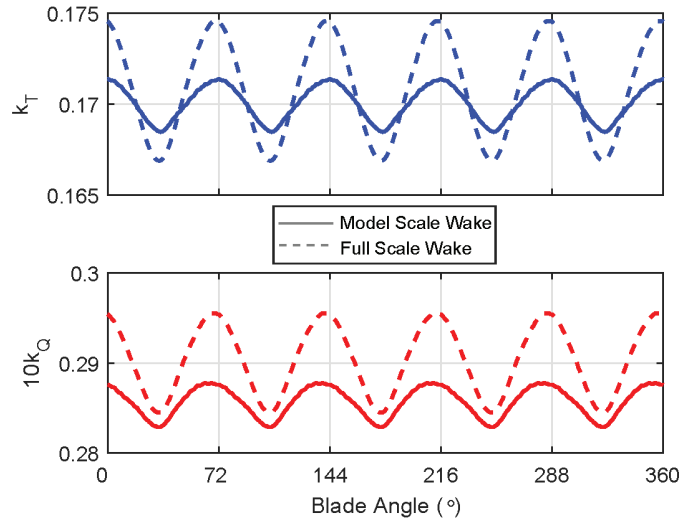
Figure 4.21 shows the arrangement of the five pressure pick ups used in the cavitation test to record induced pressures on the ship hull. Pressure pick ups P2, P3 and P4 are located in the propeller plane, with P2 being directly above the propeller while P5 and P1 are located in a longitudinal plane. The pick ups have different elevations (z-coordinate), which is not shown in the figure.

#### 4 Application to Marine Propellers



**Figure 4.18:** KCS wake field distributions in model and full scale - nominal and effective distributions. The measured and estimated model and full-scale wake fields are provided by SVA. The calculated wake fields are obtained by SHIPFLOW-ESPPRO coupling.

### 4.3 KCS Propeller in Non-Cavitating and Cavitating Flow Conditions



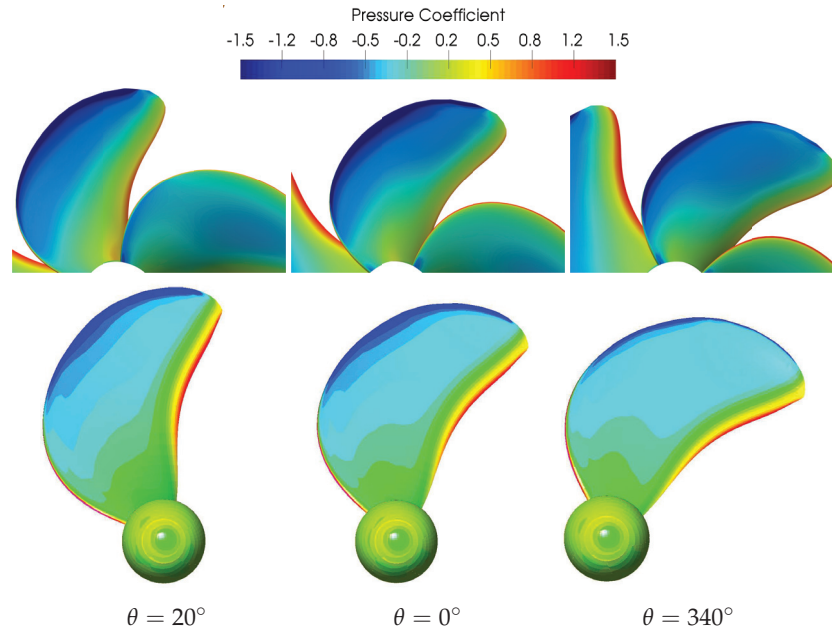
**Figure 4.19:** Non-cavitating propeller loads in behind condition for effective model and full-scale wake fields

Figure 4.22a shows the comparison between the calculated and experimental results for the harmonic amplitudes (up to five times the blade passing frequency) at each of the five pick ups for the non-cavitating condition. In order to approximate the effect of the hull, a solid boundary factor of 2 has been used (accounting for the most unfavourable case) throughout the entire thesis when analysing induced pressure fluctuations on the hull surface. The amplitudes are shown in  $100C_p$  where  $C_p = 1/2C_{pn}$  (see Equation 1.2).

The drop in amplitude from 1<sup>st</sup> order to higher orders is sharp which is expected because the propeller is not cavitating in this condition. A good agreement can be seen between the ESPPRO and the experimental results except for P5 where the deviation is significant for the first harmonic. Figure 4.22b shows a similar comparison but for propeller running in effective full-scale wake. In this case, the deviations are more pronounced and a rather general tendency of under-prediction in ESPPRO results is identified. A likely cause for the deviations is the difference in calculated and estimated inflow fields. The calculated wake fields are obtained using the exact model or full-scale hull at exact model and full-scale Reynolds numbers. Whereas, SVA has used dummy models equipped with net screen to simulated the right model and full-scale wake patterns.

The results of harmonic amplitudes for P2 between simulations with pro-

#### 4 Application to Marine Propellers



**Figure 4.20:** Blade surface pressure distribution ( $-C_{pn}$ ) for model-scale flow conditions. Top row: ESPPRO results, bottom row: SVA viscous flow calculations (color legend only applies to the ESPPRO results)

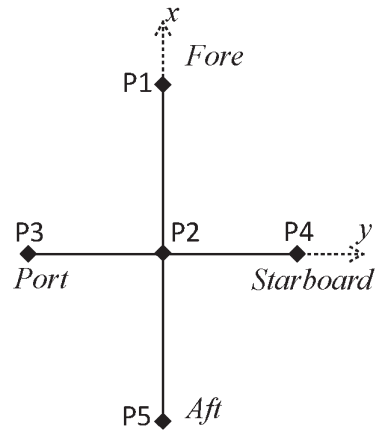
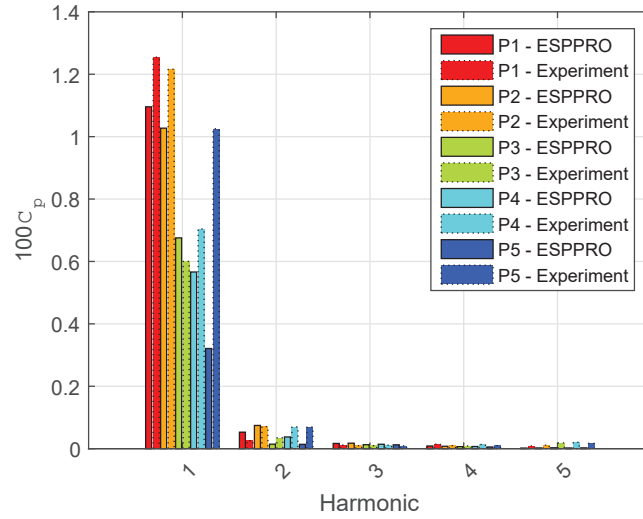
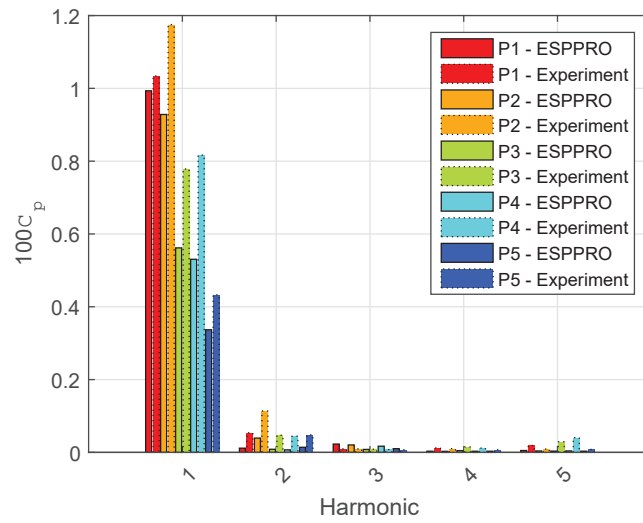


**Figure 4.21:** Arrangement of the pressure pick ups

### 4.3 KCS Propeller in Non-Cavitating and Cavitating Flow Conditions



(a) Model-scale wake field



(b) Full-scale wake field

**Figure 4.22:** Comparison of the ESPPRO results with the results of the experiment for model and full-scale wake fields in non-cavitating condition

## 4 Application to Marine Propellers

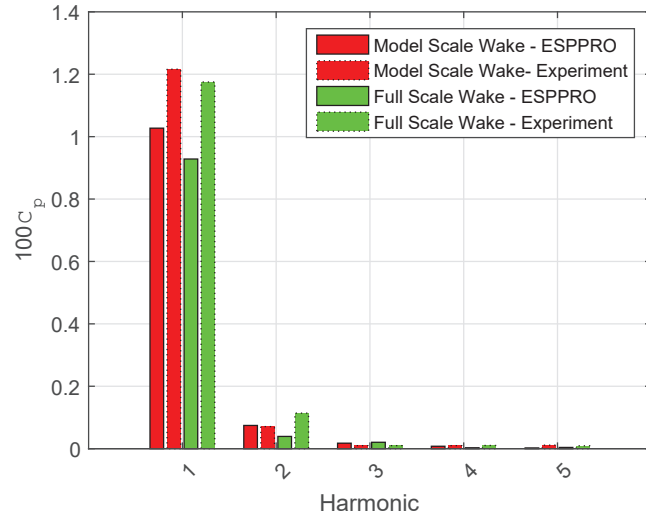


**Figure 4.23:** Comparison of pressure amplitude for P2 (directly above the propeller) between model and full-scale wake fields for both the ESP-PRO and the experimental results in non-cavitating condition

propeller running in model and full-scale wake fields and the corresponding experimental results are compared in Figure 4.23. Comparing the two sets of results from ESP-PRO, the amplitudes are very similar for each harmonic which is also the case according to the experimental results.

### 4.3.3 Unsteady Analysis in Cavitating Flow Condition

In Figure 4.24 the cavitating propeller forces when running in model and full-scale wake fields are compared. Thrust and torque coefficients found in experiment for the cavitating flow in model and full-scale wakes are 0.165 and 0.278, and 0.168 and 0.285, respectively. The deviations between the test and simulation results are  $\approx 4\%$  on both  $K_T$  and  $10K_Q$  in model-scale wake and  $\approx 2\%$  on both  $K_T$  and  $10K_Q$  in full-scale wake.

Figure 4.25 shows the blade surface pressure distribution for the cavitating flow condition. There are no viscous flow calculations in this case for comparison, however, the results appear to be reasonable. It can be seen that the low pressure area develops as the blade rotates and passes the wake peak region.

In Figure 4.26 the sketches from the cavitation test are compared with the results of ESP-PRO cavitation simulations for three different angular positions.

### 4.3 KCS Propeller in Non-Cavitating and Cavitating Flow Conditions

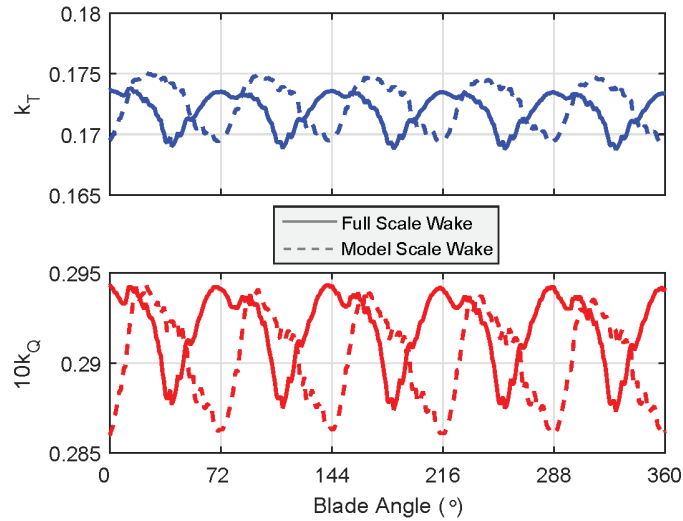


**Figure 4.24:** Calculated propeller forces in cavitating condition for model and full-scale effective wake fields

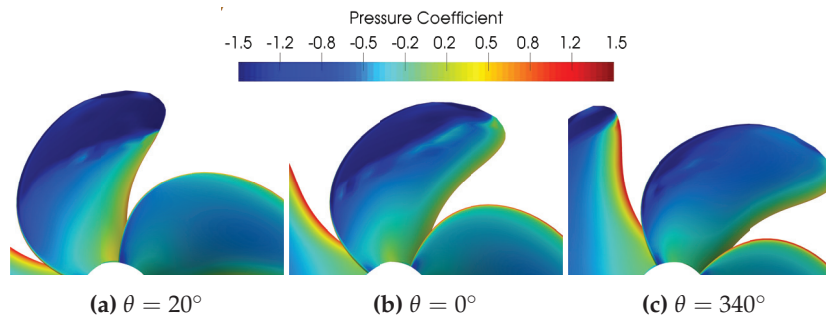


**Figure 4.25:** Blade surface pressure distribution ( $-C_{pn}$ ) in cavitating and model-scale flow conditions ( $\sigma_n = 1.489$ )

An overall good agreement can be seen between the results. There seems to be a slight tendency of over-predicting the extent of the sheet cavitation especially in chord-wise direction. The tip vortex cavitation core size and extent seem to correlate well with the results of the model test.

There are a number of important factors that need to be taken into account when comparing the numerical results and the results from the experiment. First of all, as mentioned earlier, there are uncertainties with regards to the

#### 4 Application to Marine Propellers

inflow fields. The simulations are carried out with calculated effective model (or full)-scale wake field obtained using the actual hull size and model (or full)-scale actual Reynolds number. The cavitation tests, however, are performed with dummy hulls modified to simulate the right wake patterns. Although the same effective wake *fraction* has been used for the simulations as is reported in the model test report, the difference in wake field *distribution* will have a significant influence on the cavitation performance of the propeller.

A more general remark that applies to all boundary element methods is the difficulty associated with modelling the tip flow which is caused by simple modelling of the blade tip geometry. Some flow phenomena such as the unsteady sheet cavitation that forms into a cloud happening at  $340^\circ$  angular position and between  $0.7R$  and  $0.8R$ , cannot be captured by the current model.

In addition, it seems that at  $340^\circ$  angular position the sheet cavitation integrates into the cavitating tip vortex which is not entirely captured by the simulations. The reason is that simulations treat the two types of cavitation as two individual cavitating structures, that can influence each other, e.g. sheet cavitation can widen the size of the cavitating core if it extends beyond the trailing edge, but capturing the integration of the two per se is out of the scope of this model.

In Figure 4.27 the ESPPRO cavitation results using model (right column) and full-scale (left column) effective wake fields are compared. One can see a larger cavitation extent both radially and in chord-wise direction for the propeller in model-scale wake compared to full-scale wake. Also, the thickness of the cavity appears to be larger in model-scale wake. Both cases have intermittent tip vortex cavitation, but inception occurs earlier for the case of model-scale wake. There is also inception and development of tip vortex cavitation happening around 6 o'clock position for the case of full-scale wake.

In Figure 4.28 three sets of results for harmonic amplitudes are compared. Two sets are showing the calculation results with and without tip vortex cavitation and one the results from the experiment. The same type of comparison is represented in a different way in Figure 4.29. The arrangement of the sub-plots in this figure follows the arrangement of pressure pick ups as shown in the left bottom corner.

The first-order fluctuations are over-predicted except for P5, which may be partly due to larger extent and thicker sheet cavitation predicted by calculations compared to the experimental results. The agreement for the second and third-order fluctuations seem to be good but the fourth and fifth-order fluctuations have been over-predicted. It can also be seen that the first harmonic is barely influenced by including the tip vortex cavitation in the calculations while the higher-order harmonics are more influenced. In general, the influence of TVC

### 4.3 KCS Propeller in Non-Cavitating and Cavitating Flow Conditions

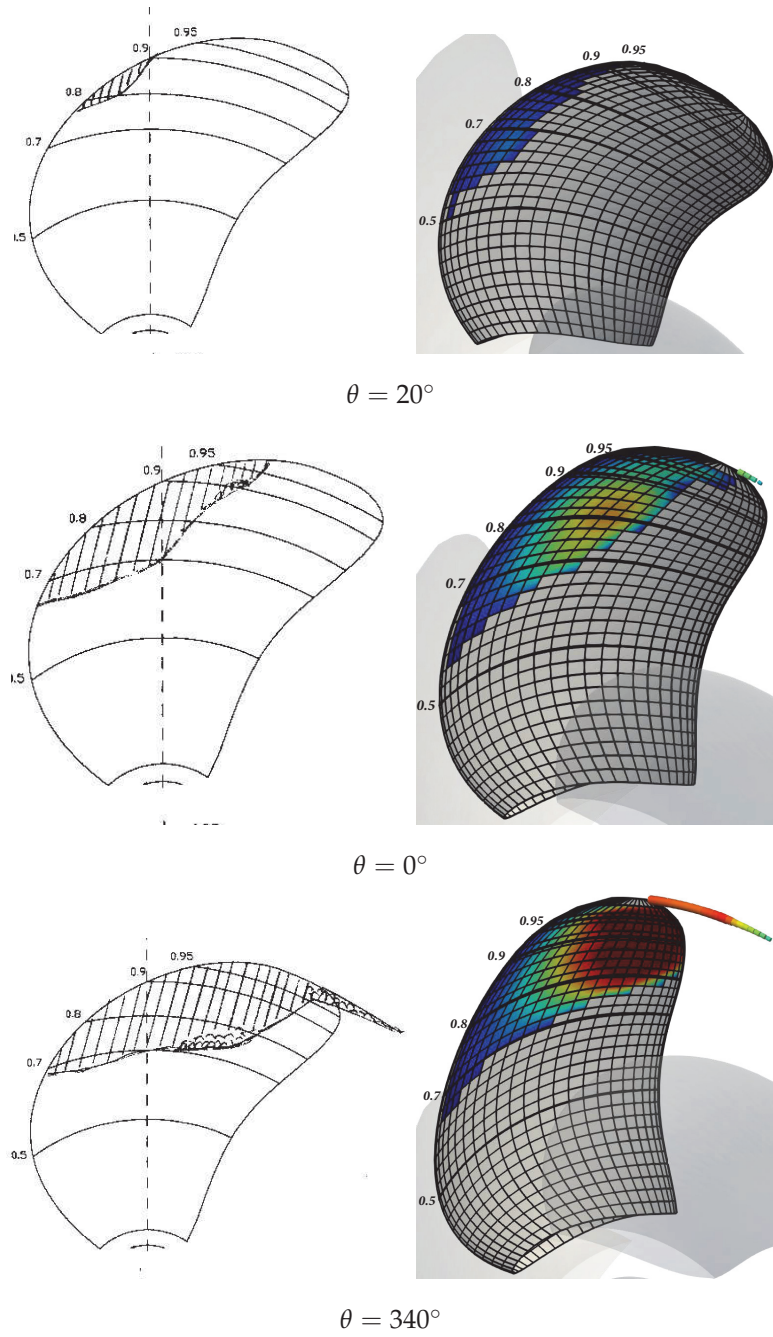


**Figure 4.26:** Comparison of cavitation extent between the ESPPRO results and the results from experiment for model-scale wake field

4 Application to Marine Propellers

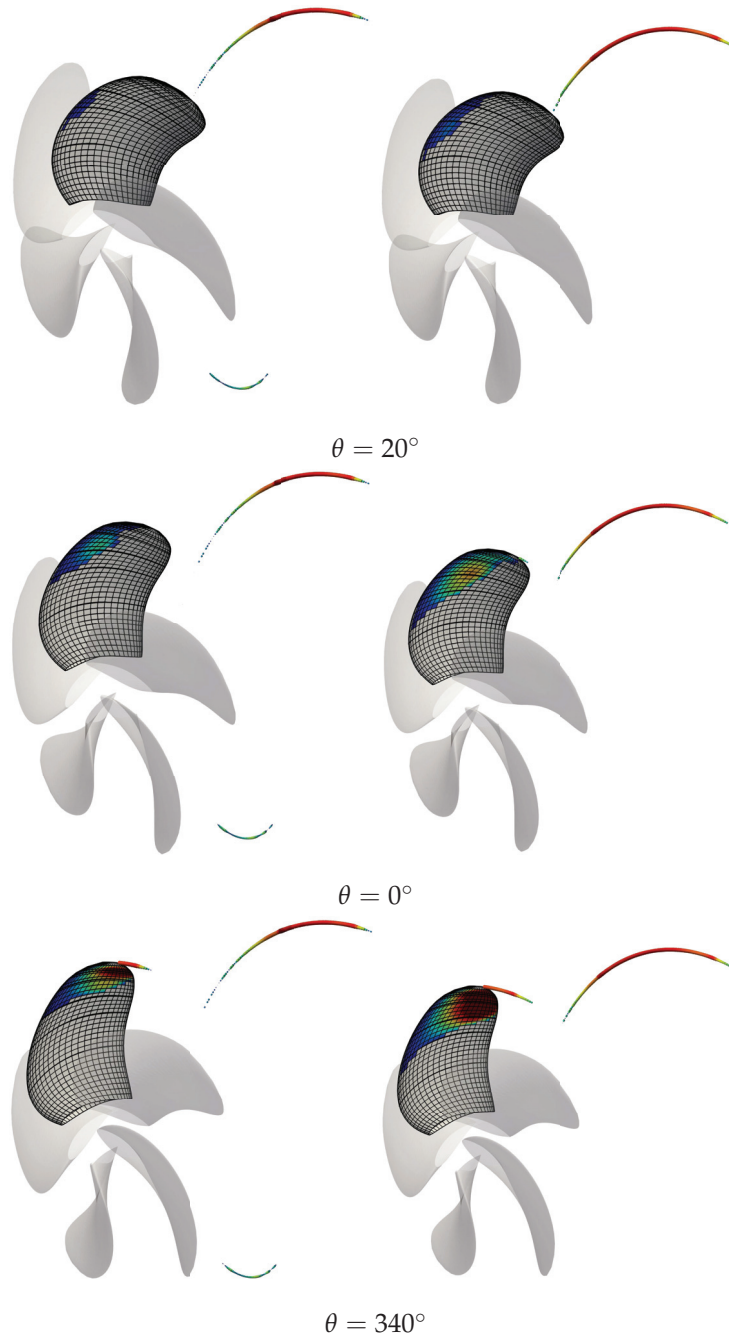


**Figure 4.27:** Comparison of cavitation extent between full-scale wake (left) and model-scale wake (right)

#### 4.4 Impact of Hull Reynolds Number on Propeller Cavitation

is small in this case.

Including tip vortex cavitation in the calculations has influenced the results in a similar way for the different pressure pick ups. However, the deviation between the calculations and experimental results differ depending on the position of the pressure pick up. Relative to the other pick ups, the results for P5 seem to have larger deviations compared to the experimental results especially for first and second-order fluctuations. This might be due to the fact that P5 is located abaft the propeller and closer to the trailing wake sheet and therefore, is more influenced by the wake geometry and strength compared to other pick ups.

Figures 4.30 and 4.31 compare the harmonic amplitudes between the calculated and the experimental results for the full-scale effective wake field. For the first-order harmonic deviation from the experimental results varies for different pick ups while for the higher-order harmonics (except the fifth-order) they are all under-predicted. In this case, all the harmonics have been influenced and in general, the deviations have been decreased by including tip vortex cavitation in the calculations.

The pressure fluctuations for pick up P2 are compared in Figure 4.32 when calculating in model and full-scale wake fields and the corresponding experimental results. According to the experimental results, there is a noticeable increase in higher order pressure fluctuations going from model-scale wake to full-scale wake (except the fifth-order) which is not entirely captured by the calculations.

The KCS propeller has been used here to validate the ESPPRO results with regards to the propeller performance and cavitation behaviour, particularly tip vortex cavitation. Based on the cavitation test results, this propeller develops sheet cavitation on the back side as it rotates and passes the wake peak and an intermittent tip vortex cavitation which is rather short in extent. ESPPRO has been able to capture this behaviour and the pressure fluctuations at various pick ups show a good agreement with the experimental results, especially for calculations in model-scale wake field. The influence of tip vortex cavitation is rather small in this case because of its short extent.

#### 4.4 Impact of Hull Reynolds Number on Propeller Cavitation

In this section, two marine propellers designed for a modern bulk carrier are analysed in two different wake fields. The two wake fields are the nominal model-scale and the effective full-scale wake field distributions. The pur-

#### 4 Application to Marine Propellers

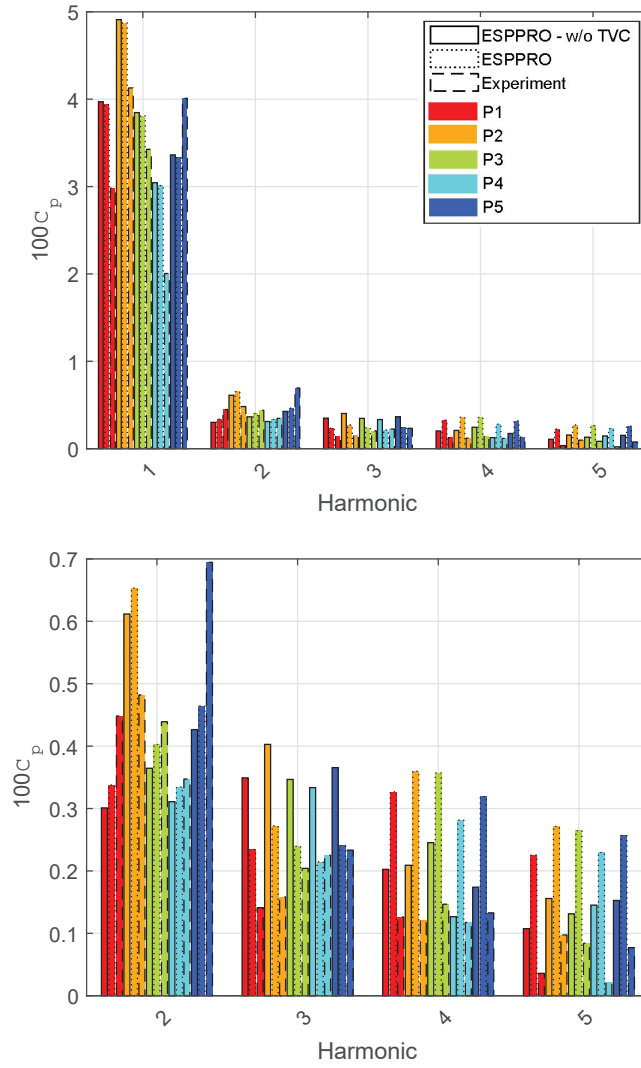


**Figure 4.28:** Harmonics of the pressure signal for cavitating condition showing with and without TVC and comparing with experimental results for model-scale wake (top) and zoom in (bottom)

#### 4.4 Impact of Hull Reynolds Number on Propeller Cavitation

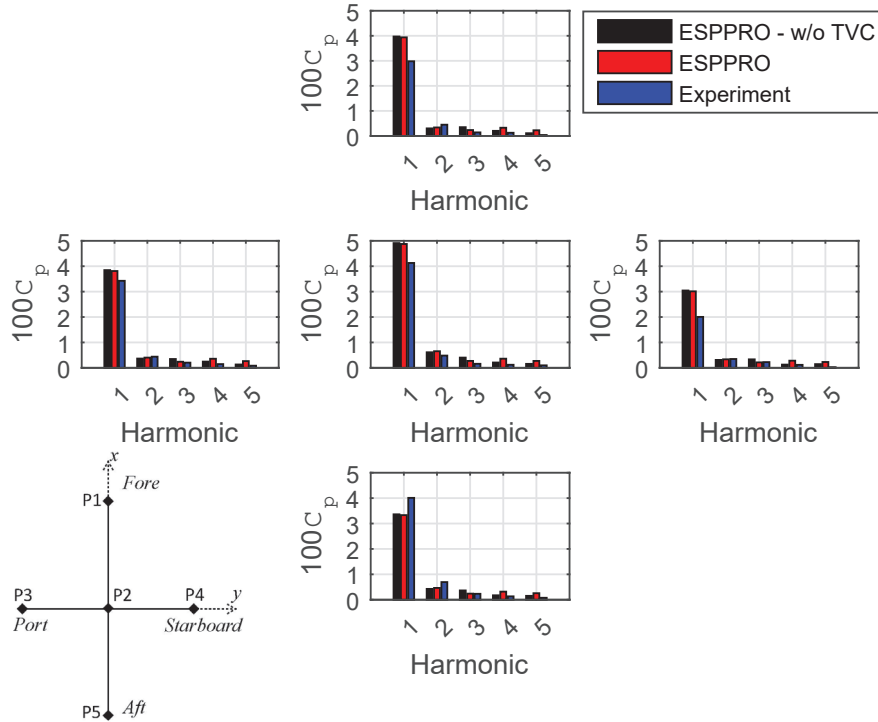


**Figure 4.29:** ESPPRO results with and without TVC compared to experiment results for model-scale wake field simulations - the arrangement of the plots follow the pick ups arrangement

pose is to investigate the influence of hull Reynolds number on the cavitation behaviour of the propellers, in particular the tip vortex cavitation, and to emphasize the importance of the availability of the correct wake field distribution when designing propellers. To this end, the two propellers are first calculated allowing only tip vortex cavitation to form, and then, both tip vortex and sheet cavitation are allowed. A similar study but without tip vortex cavitation was carried out by Regener et al. (2017).

##### 4.4.1 Description of the Case Study

The two propellers are referred to as propeller  $M$ , designed for the nominal model-scale wake field, and propeller  $F$ , designed for the effective full-scale wake field. The particulars of the hull and the two propellers are listed in

#### 4 Application to Marine Propellers

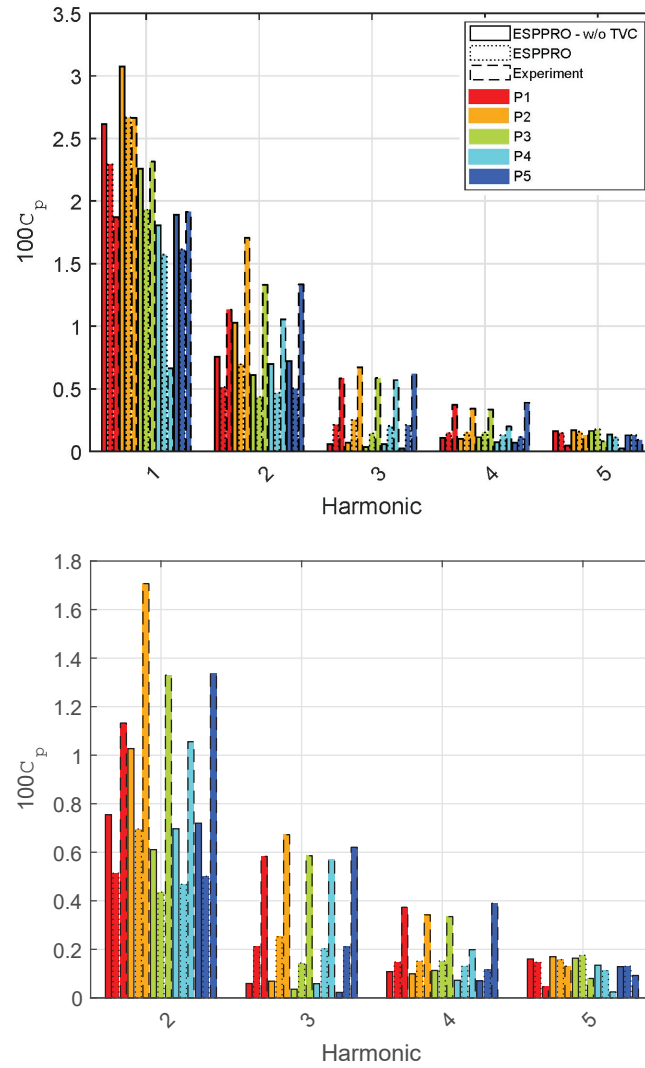


**Figure 4.30:** Harmonic amplitudes of the pressure signal for the KCS propeller in cavitating condition showing with and without TVC and comparing with experimental results for full-scale wake (top) and zoom in (bottom)

#### 4.4 Impact of Hull Reynolds Number on Propeller Cavitation

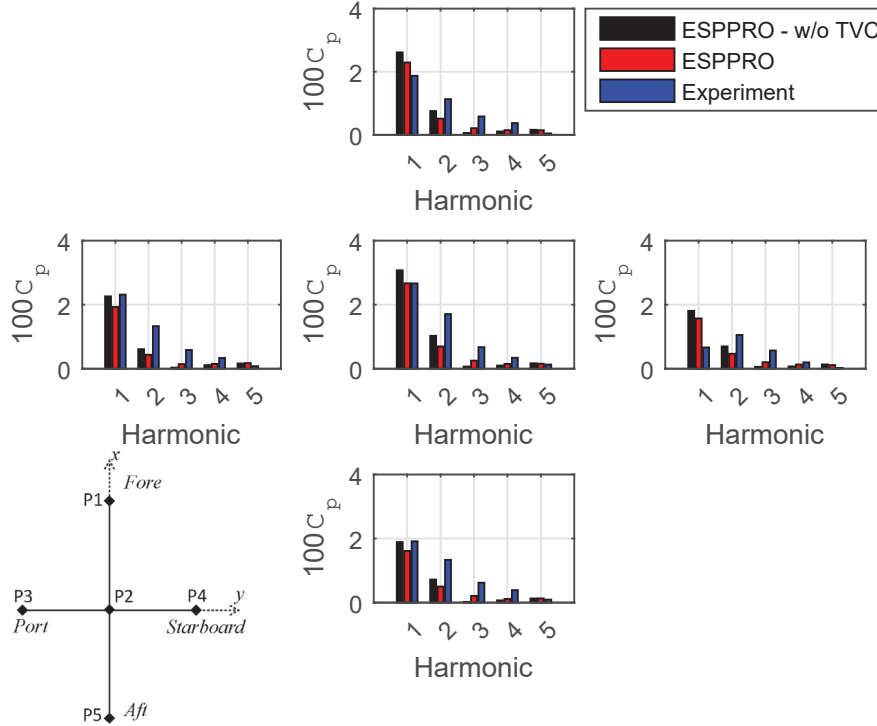


**Figure 4.31:** ESPPRO results for the KCS propeller with and without TVC compared to the experimental results for full-scale wake field - the arrangement of the plots follow the pick ups arrangement as shown on the left bottom corner

Table 4.3 and 4.4. For this ship, the nominal wake field at model-scale and the effective wake field at full-scale are obtained by running steady-state RANS and the hybrid RANS-BEM approach, respectively. This approach has been briefly discussed in Section 4.3.2. Figure 4.33 shows the calculated nominal model-scale and effective full-scale wake fields used for this analysis. As it can be seen, the full-scale effective wake distribution has a narrower wake peak compared to the nominal model-scale and the two bilge vortices apparent in the model-scale wake field are not present in the full-scale field.

The simulations include calculating propeller  $M$  in nominal model-scale and effective full-scale wake fields and propeller  $F$  in effective full-scale field. Both calculations are carried out with propellers in full-scale size. The axial components of both wake fields are uniformly scaled to the same axial wake fraction

#### 4 Application to Marine Propellers

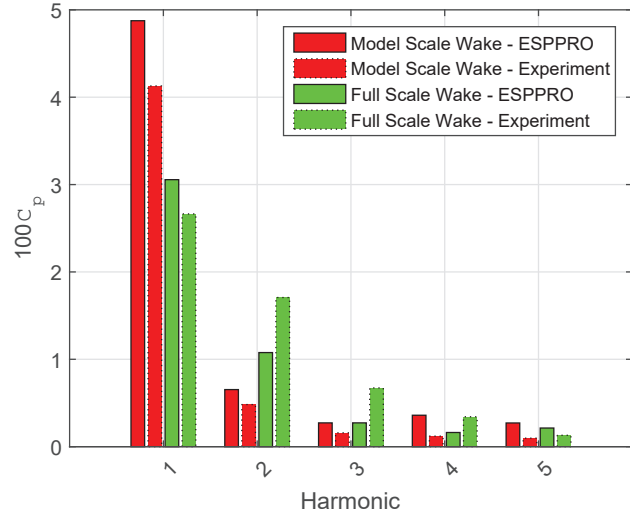


**Figure 4.32:** Comparison of pressure fluctuations for pick up P2 directly above the propeller between model and full-scale wake fields for the KCS propeller in cavitating condition

**Table 4.3:** Ship particulars

<i>Ship</i>				
Length between perpendiculars	$L_{pp}$	m	176.7	
Draught	$T$	m	10.1	
Breadth	$B$	m	30.0	
Block coefficient	$C_B$	-	0.82	

**Table 4.4:** Propeller *M* & *F* particulars

<i>Propeller</i>			<i>M</i>	<i>F</i>
Diameter	$D$	m	5.9	5.9
Pitch ratio	$P/D @ 0.7R$	-	0.9056	0.8852
Number of blades	$Z$	-	3	3
Hub ratio	$r_{hub}/R$	-	0.20	0.20
Area ratio	$A_e/A_o$	-	0.31	0.31

#### 4.4 Impact of Hull Reynolds Number on Propeller Cavitation

**Table 4.5:** Propeller *M* & *F* operating condition

Velocity	m/s	7.202
Propeller speed	rps	1.716
Effective wake fraction	-	0.250
$J$	-	0.711
$\sigma_n$	-	2.12
$Re$ (full scale)	-	$1.00 \times 10^9$
$Re$ (model scale)	-	$1.04 \times 10^7$

of  $w = 0.25$  (determined from self-propulsion test with a stock propeller) to eliminate any difference that comes from the difference in mean inflow velocity. Therefore, the differences that are to be shown and discussed here are solely due to the difference in axial velocity *distribution* and in-plane velocity components. For the cavitation simulations, cavitation number of  $\sigma_n = 1.8$  has been used. The operating conditions are listed in Table 4.5. For more details on propellers geometry, the design procedure and the calculation methods (except for tip vortex cavitation) see Regener et al. (2017).

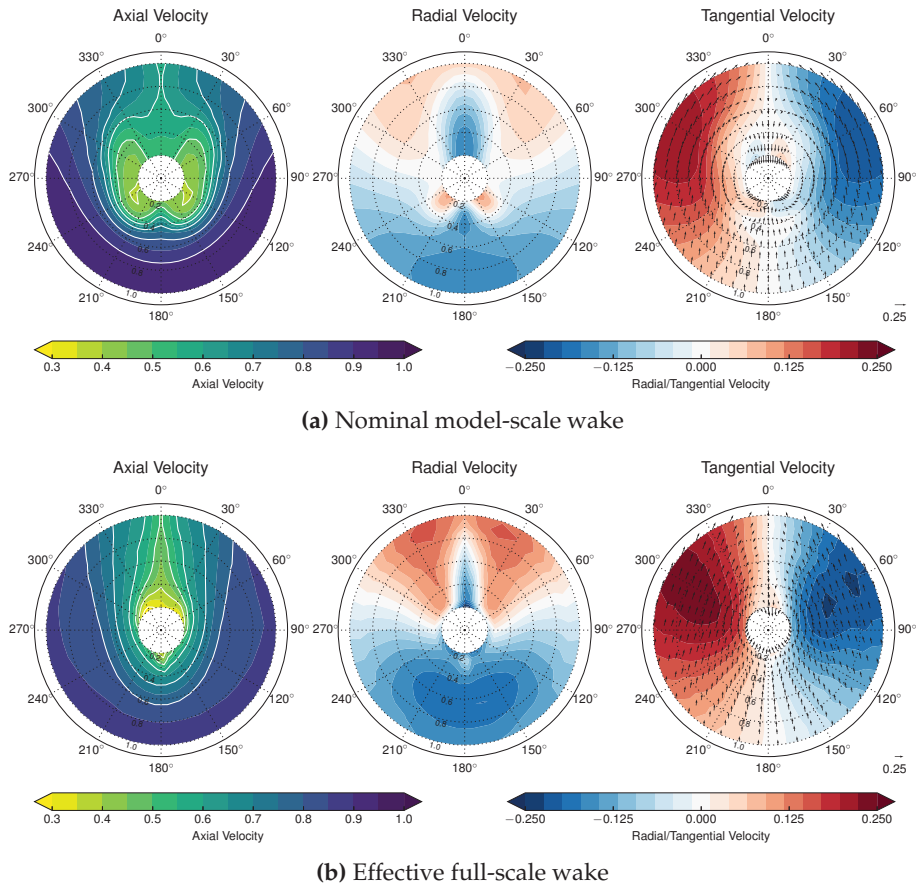
#### 4.4.2 Impact of Hull Reynolds Number on Tip Vortex Cavitation

Figure 4.34 shows the radius and circulation of the cavitating segments along the entire tip vortex line of the key blade when the blade is at 12 o'clock position. The circulation is made non-dimensional by the time-averaged maximum blade bound circulation approximated by Expression 3.8 on p. 50. The circulation for each segment corresponds to the blade tip circulation at the time when the segment was initially born.

Figure 4.34 shows the variation in cavitating core radius along the vortex line and the variation in the tip circulation as the blade rotates in the wake fields. The variations of cavity radius and circulation along the tip vortex line resemble each other which is expected according to the Rayleigh-Plesset equation (see Section 3.3.1). Propeller *M* has larger cavitating core radius along the most part of the vortex line when running in the effective full-scale field, whereas, propeller *F*, designed for this wake field, has smaller cavitating core size along the vortex line due to its lower loading at the tip. However, the main question is: do these differences influence the performance of the propellers when it comes to the higher-order pressure fluctuations?

To answer this question, a point is considered at a distance above the propeller and the pressure is computed there by taking the influence of different

#### 4 Application to Marine Propellers

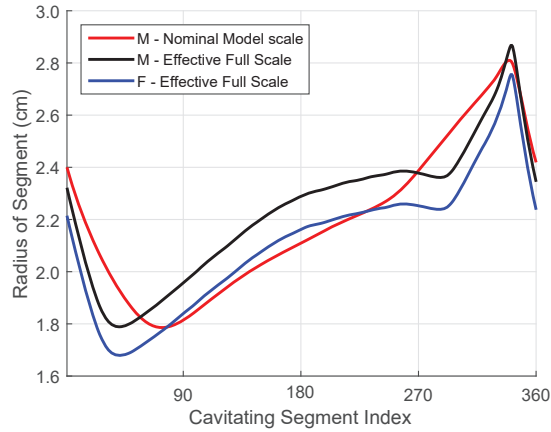


**Figure 4.33:** Calculated wake fields for the bulk carrier

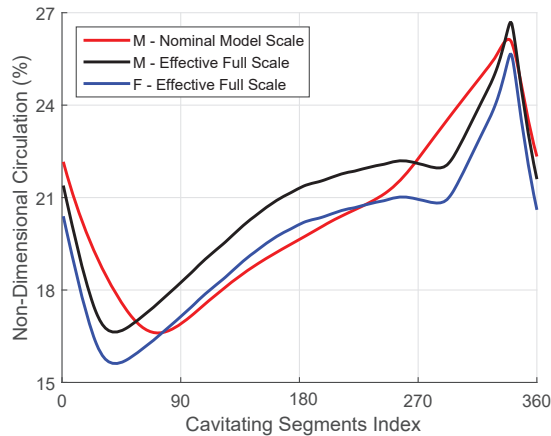
flow components into account. This approach makes it possible to include or exclude flow components based on the purpose of the investigation. Here, first the pressure fluctuations solely due to the presence of a cavitating tip vortex and then the total pressure are shown and discussed.

Figure 4.35 depicts the pressure fluctuations induced by the cavitating tip vortex and the corresponding harmonic analysis. Based on this figure, the pressure signals appear to be very similar, especially in case of propeller *M* and *F* in full-scale effective wake field. The harmonic analysis of the pressure signals points to a similar conclusion, that propeller *M* and *F* have approximately the same amplitude at the peak which in this case occurs at the 6<sup>th</sup> harmonic. An

#### 4.4 Impact of Hull Reynolds Number on Propeller Cavitation



(a) Radius



(b) Circulation

**Figure 4.34:** Radius and circulation of the cavitating segments along the tip vortex line of the key blade (blade at 12 o'clock position and without sheet cavitation)

important note here is that although the harmonic analysis shows differences between propellers, the amplitudes are so small that they will most likely be insignificant when it comes to the total pressure fluctuations.

Figure 4.36 confirms this point. As can be seen, the pressure signal oscillations are mainly of first order (blade frequency) which is also shown in the lower bar graph. The harmonic analysis shows that the amplitudes fade out

## 4 Application to Marine Propellers

quickly for all propeller variants and the presence of a cavitating tip vortex has a negligible effect.

The induced pressure fluctuations are directly related to the second-order time derivative of the cavity volume ( $p \propto \frac{d^2 V_{cav}}{dt^2}$ ). Figure 4.37 shows the volume of the entire cavitating core along the vortex line at each blade angle and over three propeller revolutions along with its harmonic analysis, and it is again confirmed that higher-order fluctuations are insignificant over time.

### 4.4.3 Impact of Sheet Cavitation on Tip Vortex Cavitation

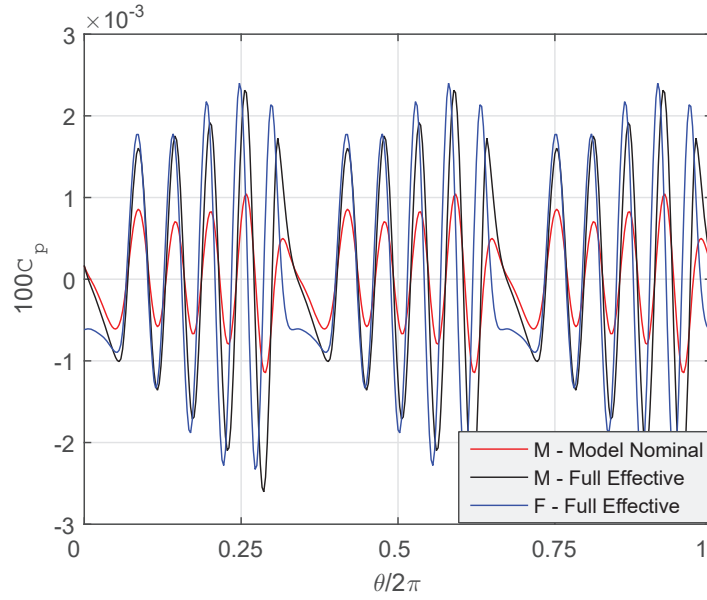
So far the conclusion has been that the propellers perform similarly with regards to higher-order pressure fluctuations (for which the source is assumed to be the cavitating tip vortex). As discussed in earlier chapters and according to the Rayleigh-Plesset equation for a cylindrical bubble (Equation 2.14), the dynamics of the developed tip vortex cavitation is mainly influenced by the vortex strength and the initial radius. Since the presence of sheet cavitation affects both these variables, it is relevant to investigate the influence of sheet cavitation on the dynamics of the developed tip vortex cavitation.

Figure 4.38 shows the circulation along the tip vortex line for the three cases both with and without sheet cavitation. It can be seen that the presence of sheet cavitation has altered the circulation distribution almost along the entire vortex line except for those segments that are born at a non-cavitating time step.

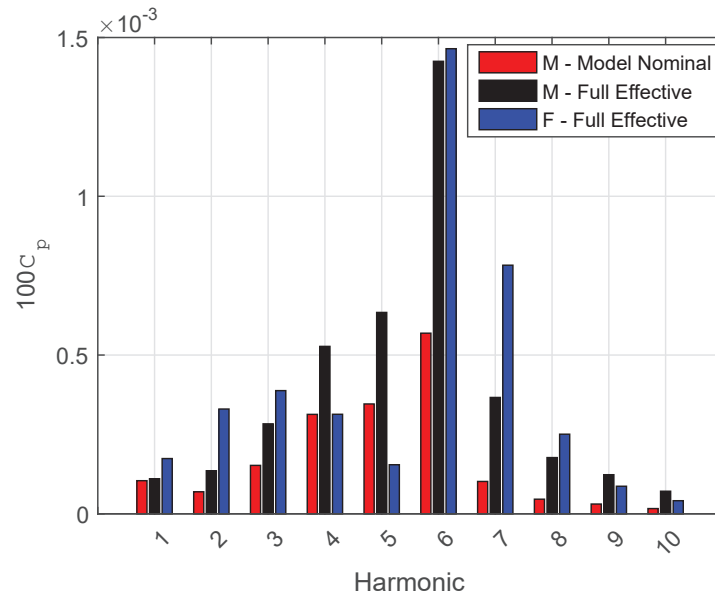
For propeller *M* in nominal model-scale wake field, Figure 4.39 depicts the equilibrium radius, the average sheet cavitation thickness at the trailing edge and the chosen initial radius. According to this figure, the initial radius is not always the equilibrium radius.

As discussed previously, an initial radius that is not equal to the equilibrium radius should lead to larger oscillations. This can be confirmed by examining the radius of the cavitating segments as they move along the vortex line which is shown in Figure 4.40 for a number of time steps. The black curves show the radius of segments along the entire vortex line at 4 different time steps when sheet cavitation is allowed. The blue curves, however, show the cavitating core radius along the vortex line when sheet cavitation is not allowed. It is clear that the presence of super-cavitation has led to larger oscillations of the cavitating tip vortex core radius. The red and green curves show the radius of one segment since the time it is born and as it travels downstream for both with and without sheet cavitation. In other words, the red and green curves show how the radius of a single segment develops from the time it is shed and as it moves along the tip vortex line and downstream. In addition, it is clear that the oscillation amplitude is larger and the frequency is lower in case the

#### 4.4 Impact of Hull Reynolds Number on Propeller Cavitation



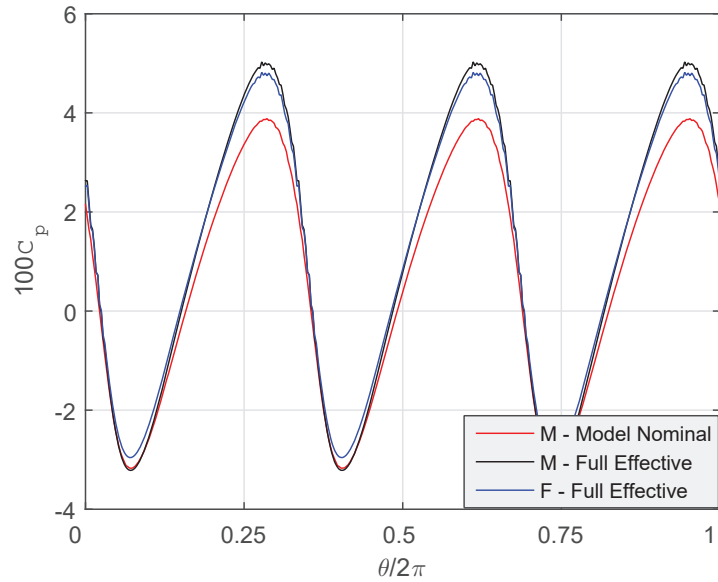
(a) Pressure ( $\theta$  indicates the key blade position)



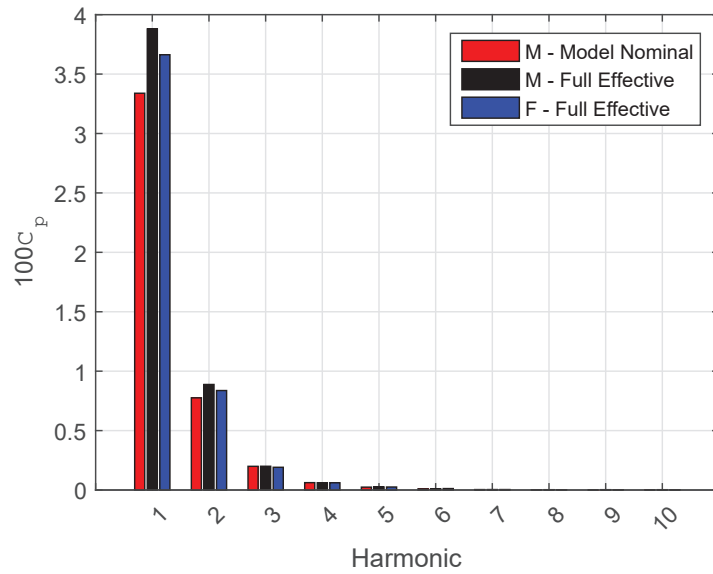
(b) Harmonics

**Figure 4.35:** Pressure signal induced by only the cavitating tip vortex and the harmonics amplitudes

#### 4 Application to Marine Propellers



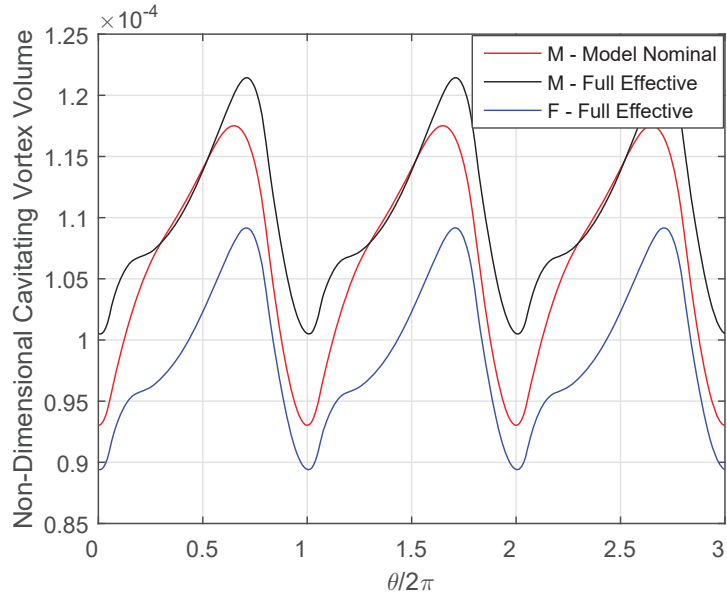
(a) Pressure ( $\theta$  indicates the key blade position)



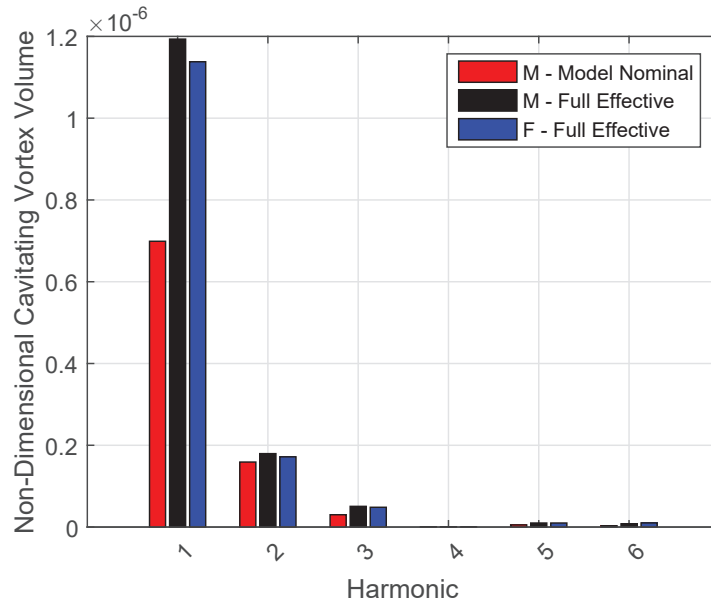
(b) Harmonics

**Figure 4.36:** Total pressure signal and the harmonic analysis (without sheet cavitation)

#### 4.4 Impact of Hull Reynolds Number on Propeller Cavitation



(a) Tip vortex cavity Volume



(b) Harmonics

Figure 4.37: Volume of the entire cavitating tip vortex and its harmonic analysis

#### 4 Application to Marine Propellers

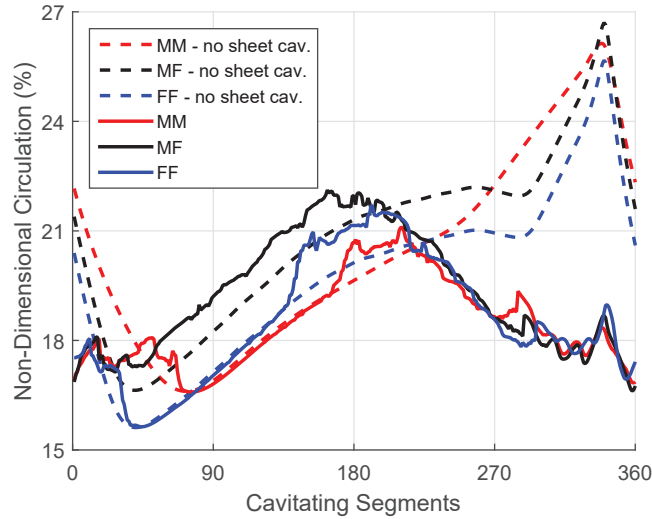


**Figure 4.38:** Cavitating segment’s circulation along the tip vortex line for the three cases both with and without sheet cavitation. *MM* and *MF* refer to propeller *M* in model nominal and full effective wake and *FF* to propeller *F* in full effective wake

segment is born at a supercavitating time step.

Cavity extent for propeller *F* in effective full-scale wake field is shown in Figure 4.41. The top figure shows the case where interaction between sheet and tip vortex cavitation is included in the calculation and the bottom figure where it is not.

To investigate the performance of the propellers, pressure fluctuations and cavity volume of the three cases are examined. Figure 4.42 shows the pressure fluctuations induced only by the cavitating tip vortex and the resulting harmonic analysis. Comparing this figure with Figure 4.35, one can realize the difference in order of magnitude between the two cases. In case of not allowing sheet cavitation the amplitude of the peak is  $\approx 0.8 \times 10^{-3}$  kPa which is shown to be insignificant when analysing the total pressure. However, in the case with sheet cavitation the amplitude of the peak is larger, approx. 0.8 kPa, which is certainly significant in the overall performance. This is confirmed by Figure 4.43.

Comparing Figure 4.43 and 4.36, one can see that the first and second order harmonics amplitudes are increased significantly which is mainly because of the presence of blade sheet cavitation. Previously, the harmonic amplitudes

#### 4.4 Impact of Hull Reynolds Number on Propeller Cavitation

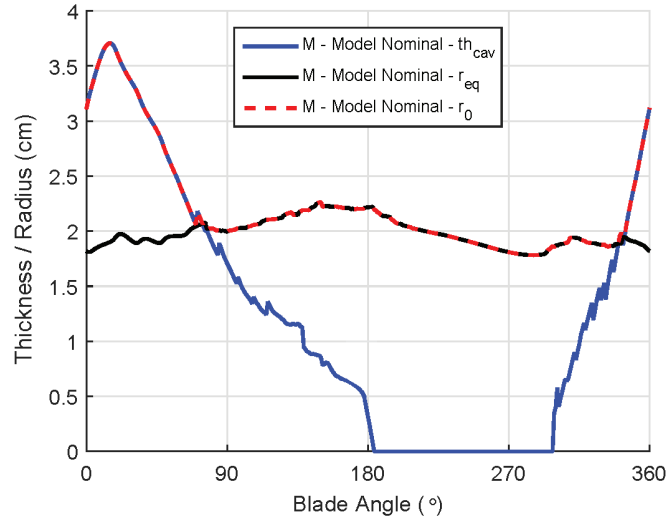


Figure 4.39: Initial radius for propeller  $M$  in nominal model-scale wake field

faded out quickly after  $2^{nd}$  order, however, now the amplitudes pick up again at  $7^{th}$  or  $8^{th}$  (depending on the propeller and wake combination). The higher order peaks are known to be mainly due to the presence of an oscillating tip vortex cavitation. Comparing the performance of the propellers, one can see that the propeller  $M$  when operating in full-scale condition, shows higher pressure amplitudes. However, propeller  $F$  that is designed for that condition, performs better in effective full-scale wake field. This once again emphasizes the importance of having the right inflow velocity distribution when designing propellers.

Figures 4.37 and 4.44 show that the magnitude of the cavity volume is not changed significantly. However, there are significantly larger oscillations in case sheet cavity develops on the blade and extends beyond the trailing edge.

#### 4.4.4 Impact of Tip Vortex Cavitation on Sheet Cavitation

As discussed earlier, each cavitating tip vortex segment is represented by a point source travelling with the flow. The influence of these potential sources on the blade (and sheet cavitation) is considered in this implementation as discussed in Section 2.3.3. Therefore, it is possible to investigate the effect of the dynamics of a cavitating core at the center of the tip vortex on the blade sheet cavitation. The propeller used for this purpose is propeller  $F$ . The propeller is

#### 4 Application to Marine Propellers

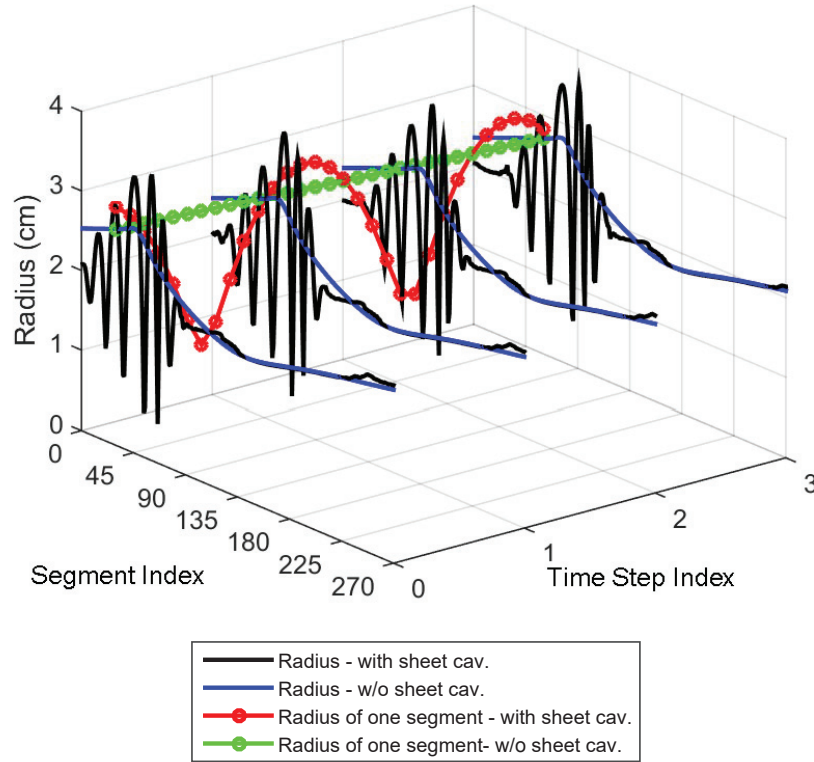
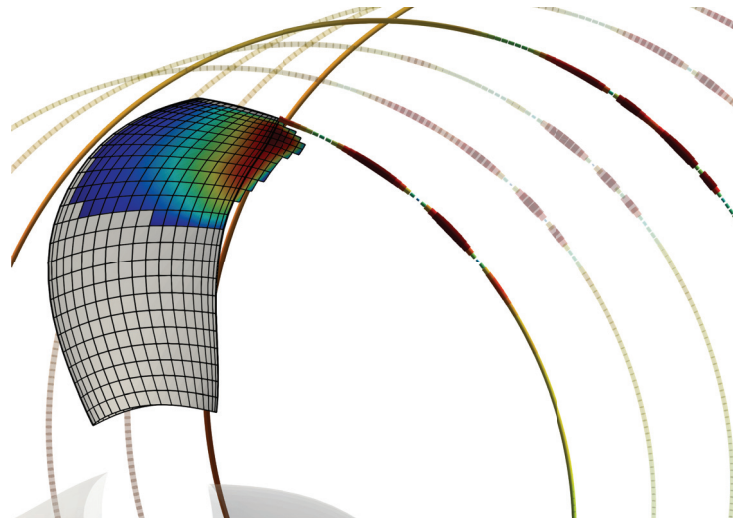


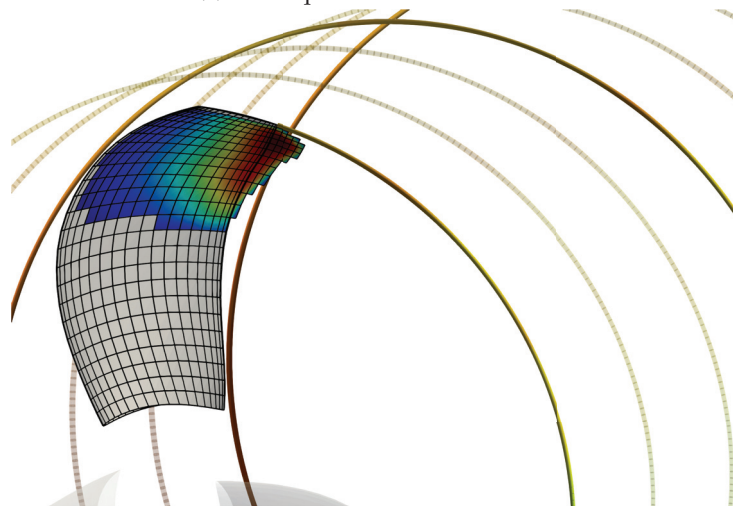
**Figure 4.40:** Radius of the cavitating segments at 4 different time steps for propeller *M* in effective full scale wake field

allowed to develop both sheet and tip vortex cavitation, but two simulation cases are considered. One where the influence of the tip vortex cavitation on sheet cavitation is included and one where it is not. The results are shown in Figure 4.45. In this figure, the blade sheet cavitation volume is displayed for both cases with and without TVC influence included. For this propeller and this running condition and given the scope and capabilities of the current models, the influence of the cavitating tip vortex on the sheet cavitation exists but is insignificant.

4.4 Impact of Hull Reynolds Number on Propeller Cavitation



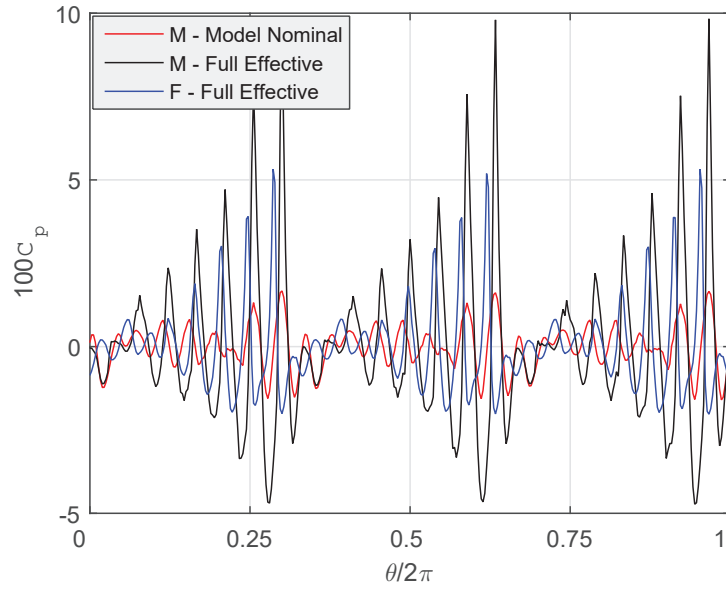
(a) Non-equilibrium initial radius



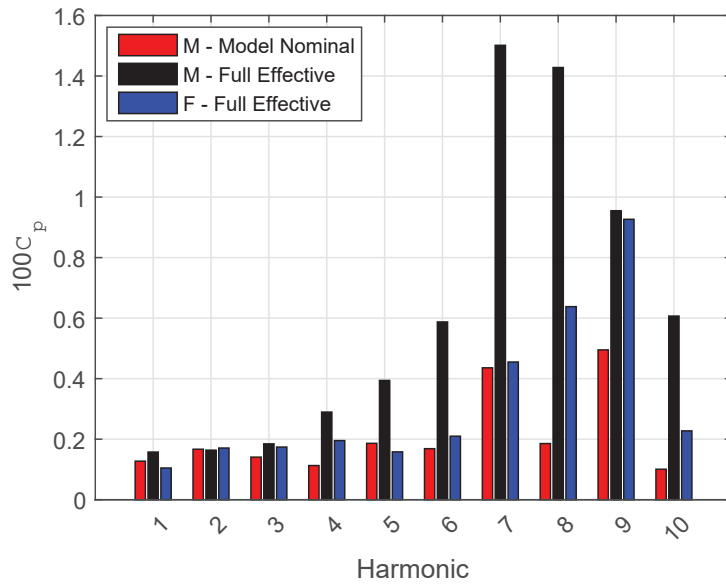
(b) Equilibrium initial radius

Figure 4.41: Propeller  $F$  in effective full-scale wake distribution

#### 4 Application to Marine Propellers



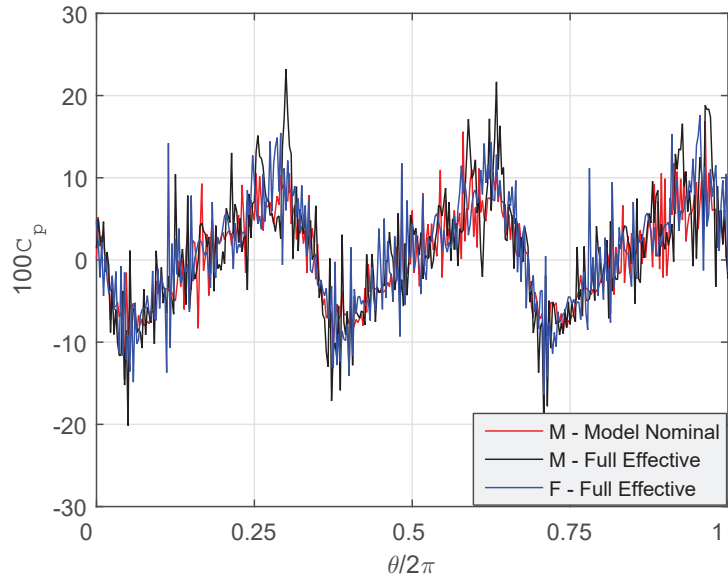
(a) Pressure



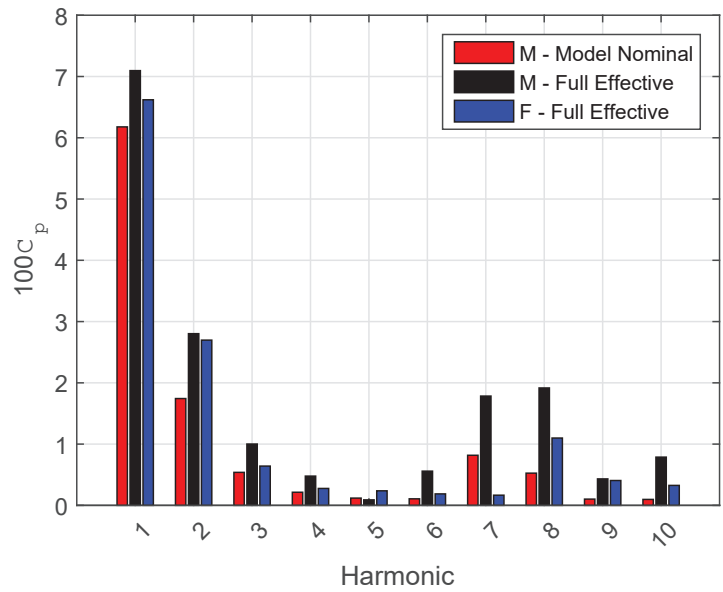
(b) Harmonics

**Figure 4.42:** Pressure signal induced by only the cavitating tip vortex and harmonics amplitude

#### 4.4 Impact of Hull Reynolds Number on Propeller Cavitation



(a) Pressure



(b) Harmonics

**Figure 4.43:** Total pressure signal and its harmonic analysis

#### 4 Application to Marine Propellers

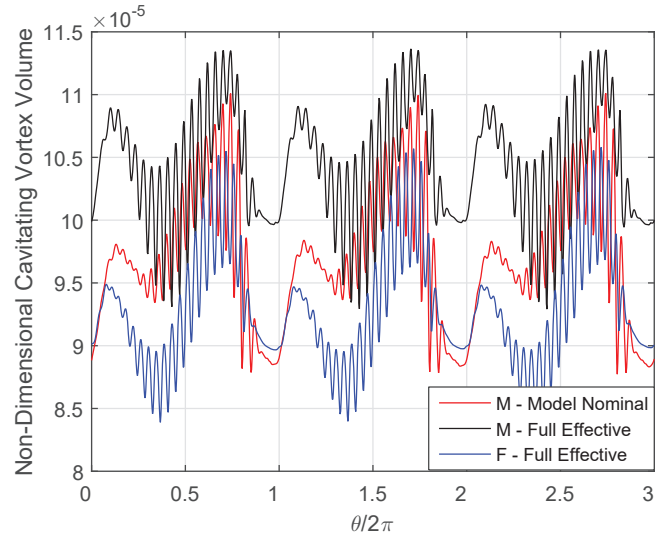


**Figure 4.44:** Volume of the cavitating tip vortex

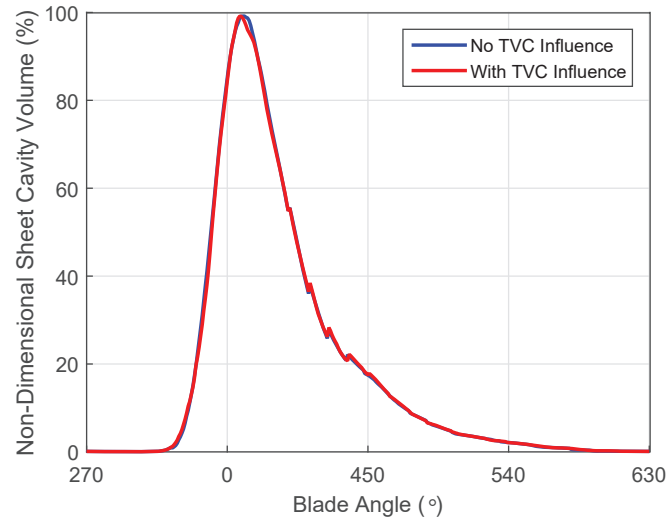


**Figure 4.45:** Sheet cavitation volume on propeller *F* with and without TVC influence

## 5 Conclusions and Outlook

In this thesis, a numerical model for the prediction of inception of tip vortex cavitation and dynamics of cavitating tip vortex has been developed and integrated into an existing panel code for the analysis of the cavitating propeller flow. It is believed that the developed model and the analysis tool presented here offer the features required for an analysis tool that can be used within the propeller design process, namely a stand-alone tool that is fast and efficient and has the accuracy needed for simulation-based propeller design optimisation, especially at early design stages.

### 5.1 Discussion and Conclusions

As an integral part of the numerical study, the model for developed tip vortex cavitation has been checked for convergence. Significant variables when considering convergence here, are the time step size and the outer domain radius. Applying the model to a propeller that develops tip vortex cavitation for a range of time step sizes and analysing the induced pressure fluctuations, revealed that there is convergence in terms of time step size and it should be as small as  $1.0^\circ$  to avoid erroneous conclusions.

The study regarding the choice of  $R_D$  (Section 3.5) showed that the influence of the outer domain radius on the results is significant and there is no convergence with increasing the outer domain radius. This and also Figure 2.5 suggest that the ratio between the outer domain radius and the cavitating core should be larger than 10, as the vortex pressure reaches an approximately constant level at a distance around 10 times the viscous core radius. Based on the results of the case used in this study, a value of less than twenty results in unrealistically large third or fourth harmonics amplitudes.

Two methods for predicting inception of tip vortex cavitation have been used for a submarine propeller of type Kappel and the results have been compared to each other as well as to the experimental results. The inception model requires the viscous core radius of the tip vortex as input. Since this variable cannot be computed with the present method, the model has to be calibrated. Here, experimental data have been used for this purpose. Both methods, the engineering criterion and the bubble growth method, generate very similar

## 5 Conclusions and Outlook

results, however, the bubble growth method in general predicts smaller margin against cavitation.

For validation purposes, the model has been applied to two well-known public test cases for which experimental and/or numerical results obtained by other methods are available. Results of tip vortex cavitation model depends on the input parameters for the vortex model which are provided by the BEM part of the solution and therefore, it is necessary to check and validate the results of the BEM part as well. For example, inflow field, propeller forces, non-cavitating and cavitating surface pressure distributions and sheet cavity extent have been compared to the available benchmark values. Results from the tip vortex cavitation model have been validated indirectly by comparing higher-order induced hull pressure fluctuations at the measurement points. The results obtained in these studies reveal that the individual parts of the method work well and the deviations are generally within the acceptable range when compared to other available results.

Furthermore, as mentioned previously, it is assumed that the interaction between sheet and tip vortex cavitation is the main contributor to higher-order pressure fluctuations. This emphasizes that an isolated tip vortex cavitation results in nearly insignificant hull pressures, but combined with sheet cavitation the influence is pronounced. This influence is mainly on the higher-order pressure fluctuations suggesting that the tip vortex cavitation should definitely be included in a cavitation analysis. In reality, tip vortex cavitation might be the first type of cavitation that takes place but it is very seldom that it is the only type of cavitation that occurs.

Comparing pressure fluctuations with experimental results has only been possible in case of the KCS propeller and for the two conditions considered in the model test. An overall good agreement is observed, especially for the case of model-scale wake field. The experimental results for the case of full-scale wake, show rather high levels of higher order fluctuations which has not been captured by the current method. Since the second-order pressure fluctuations are also quite considerable, the reason could lie in the growth and shrinkage of the sheet cavity. However, it is not possible to prove this point as no experimental results are available in this regard.

Propeller designers highly depend on the wake field provided to them for their design. It is shown that it is significant that the correct full-scale effective wake field is the basis for the design. This result is obtained by considering two propellers designed for the same bulk carrier but using wake field distributions for the model and full scale cases, even if the axial wake is simply scaled to obtain the same overall wake fraction for both wake fields. The dynamics of the tip vortex cavitation is pronounced when there is an interaction between sheet

and tip vortex cavitation and it can be seen in the hull pressure signatures.

## 5.2 Recommendations for Future Work

As mentioned previously, the interaction between sheet and tip vortex cavitation results in higher-order oscillations. Therefore, it is relevant to further study and evaluate alternative ways of capturing this interaction. In the current study, the largest of the two, equilibrium radius or the span-wise average of the sheet cavity thickness at the trailing edge is fed to the TVC model as the initial radius. An alternative approach can for example be to take the sheet cavity thickness at the trailing edge at a certain radial station.

Validating the results of the model is in general a challenging task. This is due to the limited extent of previous work (experimental or numerical) on this topic. The previous work regarding prediction of propeller cavitation and associated pressure fluctuations are mostly only concerning the prediction of sheet cavitation and first and second order hull pressure fluctuations. It has only been recently that focus has been put on modelling developed tip vortex cavitation and prediction of higher-order pressure fluctuations. Moreover, the complexity of the problem increases by the fact that tip vortex cavitation occurs in combination with other types of cavitation and therefore, accurate prediction of those will directly influence the accuracy of the results for TVC. With this being said, a future task could be to look into MAN Energy Solutions' extensive propeller design and model test report database to find relevant test cases. This should primarily target propellers that develop rather stable sheet cavitation rolling up into an extended cavitating tip vortex. These cases can then be used for validation of both sheet and tip vortex cavitation.

In this context, a more general recommendation concerns the scope of the experimental results. In case of validating against experimental results, the validation is done mostly indirectly by comparing hull pressure fluctuations. There are uncertainties associated with this approach first of all because other flow phenomena can affect these results and also the dependency of the results on the number of revolutions taken into considerations. Therefore, a more direct way of validating the results for sheet and tip vortex cavitation could be of major help. To date, cavitation videos and sketches are the most common ways employed by the model basin institutes to provide information to their customers and to support their opinion on the cavitation characteristics of the propeller. This can be supported with data on variation of sheet cavitation area or volume and variations of tip vortex cavitation core radius over time.



# Nomenclature

## Abbreviations

BEM	Boundary element method
DTU	Technical University of Denmark
ESPPRO	DTU-developed panel code
SSPA	Statens Skepps-provningsanstalt (the State's Ship Testing Facility)
SVA	The Potsdam Model Basin (Schiffbau Versuchsanstalt Potsdam)
TVC	Tip vortex cavitation

## Greek symbols

$\alpha$	Constant used in the exponential function to account for growth of circulation with roll-up
$\beta$	Ratio between the outer domain radius and the cavity radius
$\delta$	Boundary layer thickness over a flat plate
$\eta_o$	Propeller open water efficiency
$\Gamma$	Vortex circulation
$\gamma$	Ratio of heat capacities
$\Gamma_b$	Blade bound circulation
$\kappa$	Constant depending on the blade shape
$\lambda$	Ratio between initial and blade bound circulation
$\mu$	Dynamic viscosity
$\nu$	Kinematic viscosity
$\phi_i$	Potential at the control point of panel $i$ on blade

## 5 Conclusions and Outlook

$\rho$	Density
$\sigma_B$	Strength of continuous source distribution on blade surface
$\sigma_i$	Incipient cavitation number
$\sigma_k$	Strength of potential point source associated with segment k
$\sigma_n$	Cavitation number based on propeller speed
$\sigma_V$	Strength of continuous source distribution on the vortex line
$\sigma_{CW}$	Strength of continuous source distribution on cavitating wake surface
$\tau$	Factor used for calibrating the viscous core radius, found by data fitting approach

### Latin symbols

<b>A</b>	Influence coefficient matrix ( $A_{ij}$ ): influence of unit strength dipole on blade panel j on blade panel i
<b>B</b>	Influence coefficient matrix ( $B_{ij}$ ): influence of unit strength source on blade panel j on blade panel i
<b>C</b>	Influence coefficient matrix ( $C_{ij}$ ): influence of unit strength source on wake panel j on blade panel i
<b>V</b>	Influence coefficient matrix ( $V_{ij}$ ): influence of unit strength source on tip vortex line segment j on blade panel i
<b>W</b>	Influence coefficient matrix ( $W_{ij}$ ): influence of unit strength dipole on wake panel j on blade panel i
$\vec{U}_B$	Spherical bubble velocity
$\vec{U}_f$	Fluid velocity
$\vec{X}_B$	Spherical bubble position
$C_L$	Lift coefficient
$C_{0.95R}$	Chord at 0.95R
$C_D$	Drag coefficient
$C_{pn}$	Pressure coefficient based on propeller speed

## 5.2 Recommendations for Future Work

$D$	Propeller diameter
$d_q$	Distance between off-body point and segment $i$
$dl_k$	Length of an arbitrary segment $k$
$f$	Frequency of oscillations
$h_{cav}$	Span-wise average of the sheet cavity thickness at blade trailing edge
$J$	Propeller advance ratio
$K$	Constant of proportionality in Equation 1.3
$K_Q$	Propeller torque coefficient
$K_T$	Propeller thrust coefficient
$L_V$	Vortex line
$n$	Propeller speed
$N_b$	Number of cavitation nuclei assumed in the domain for the bubble growth approach
$p_\infty$	Reference pressure
$p_v$	Vapour pressure
$p_{cav}$	Pressure inside the cavitating core
$p_D$	Pressure at the outer domain radius
$p_{g0}$	Initial gas pressure of bubble
$p_{min}$	Minimum pressure at the center of the vortex
$p_{vortex}$	Vortex pressure
$R_c$	Vortex viscous core radius
$r_{b,ave}$	Bubble average radius for the bubble growth approach
$R_{B_0}$	Spherical bubble initial radius
$R_B$	Spherical bubble radius
$R_{cav,eq}$	Cavitating core equilibrium radius
$R_{cav_0}$	Cavitating core initial radius

## 5 Conclusions and Outlook

$R_{cav}$	Cavitating core radius
$R_D$	Outer domain radius
$R_{p,q}$	Distance between the field and variable point
$Re$	Reynolds number
$Re_B$	Spherical bubble Reynolds number
$S$	Surface tension
$T$	Period of oscillations
$v_T$	Vortex induced tangential velocity
$V_{cav}$	Cavity volume
$Z$	Number of blades

## List of Figures

1.1	Various forms of cavitation. By courtesy: SSPA Sweden AB, Gothenburg, Sweden . . . . .	3
1.2	Schematic of growth of tip vortex strength . . . . .	6
1.3	Flow chart showing the sequence involved in analysing propeller performance and induced pressure fluctuations . . . . .	12
2.1	Rankine and Burgers vortex velocity distributions . . . . .	17
2.2	Tip vortex trajectory following the upper edge of the trailing wake sheet and the tip vortex segments . . . . .	17
2.3	Configuration illustrating details of a cavitating vortex segment	22
2.4	Sheet cavity rolling up into the cavitating tip vortex. By Courtesy: MAN Energy Solutions, Frederikshavn, Denmark . . . . .	24
2.5	Rankine pressure distributions. Pressure difference is made non-dimensional by $\rho \frac{\Gamma}{2\pi R_c}$ and radius by $R_c$ . . . . .	26
3.1	Calculation results for single bubble growth under decreased pressure . . . . .	31
3.2	Growth of a cylindrical bubble as a function of time for varying final pressure value . . . . .	32
3.3	Growth of a cylindrical bubble as a function of time for varying $\Delta t$ of the application of the final pressure value . . . . .	33
3.4	Artificial inflow field used for simulations with Propeller S . . . . .	34
3.5	Schematic of developed tip vortex cavitation. Model-scale propeller geometry (Propeller S) . . . . .	35
3.6	Radius of the cavitating segments along the vortex line and the corresponding circulation at a single time-step . . . . .	35
3.7	Average radius of a single segment when initializing with equilibrium and non-equilibrium radius (followed as it travels downstream) . . . . .	37
3.8	Cavitating tip vortex volume over six propeller revolutions. $\theta$ is the angular position of the key blade . . . . .	38
3.9	Total pressure time signal over one revolution (top) and zoom in (bottom) for varying segment sizes . . . . .	39

List of Figures

3.10	Harmonics amplitudes of the total pressure signal for varying segment sizes . . . . .	40
3.11	Pressure time signal induced by the cavitating tip vortex at the off-body point for varying segment sizes ( $\Delta t$ ) . . . . .	41
3.12	Total pressure time signal for varying deviations from the equilibrium radius . . . . .	42
3.13	Total pressure signal harmonics amplitude for varying deviations from the equilibrium radius . . . . .	43
3.14	Pressure time signal induced by the cavitating tip vortex for varying deviations from the equilibrium radius . . . . .	44
3.15	Amplitudes of the pressure signal induced by the cavitating tip vortex for varying deviations from the equilibrium radius . . . . .	45
3.16	Total pressure time signal and harmonics amplitudes for $\Delta t = 1^\circ$ and varying deviations from equilibrium radius . . . . .	46
3.17	Pressure time signal induced by the cavitating tip vortex and harmonics amplitudes for $\Delta t = 1^\circ$ and varying deviations from equilibrium radius . . . . .	47
3.18	Pressure fluctuations with and without growth of the vortex strength and viscous core size . . . . .	49
4.1	Kappel propeller model geometry and the panel code input geometry . . . . .	52
4.2	Wake field of the submarine . . . . .	53
4.3	Measured relative margin against tip vortex cavitation . . . . .	54
4.4	Relative cavitation margin predicted by the engineering criterion, Eq. 2.8, and compared to the experimental results . . . . .	55
4.5	Relative cavitation margin predicted by the bubble growth method and compared to the experimental results . . . . .	56
4.6	Comparison of bubble growth and engineering criterion results for the inception of tip vortex cavitation . . . . .	56
4.7	Variations simulated as part of sensitivity analysis of the bubble growth approach to input parameters . . . . .	57
4.8	Influence of number of bubbles on the inception prediction by bubble growth. ● indicates the prediction by bubble growth method and solid line shows the prediction based on the engineering criterion . . . . .	58
4.9	Influence of average bubble radius on the cavitation margin. ● indicates the prediction by bubble growth method and solid line shows the prediction based on the engineering criterion . . . . .	59
4.10	E779a model geometry and the panel code geometry input . . . . .	60

4.11	Open water curve for wetted flow condition $J = 0.71$ . CFD results refer to the results presented in Vaz et al. (2015) . . . . .	61
4.12	Open water sectional pressure distribution for both wetted and cavitating flow conditions - $J = 0.71$ and $\sigma_n = 1.76$ . . . . .	62
4.13	Propeller surface pressure distribution ( $-C_{pn}$ ) in wetted flow condition $J = 0.71$ . . . . .	62
4.14	Propeller surface pressure distribution ( $-C_{pn}$ ) in cavitating flow condition $J = 0.71$ and $\sigma_n = 1.76$ . . . . .	63
4.15	Open water cavity extent $J = 0.71$ and $\sigma_n = 1.76$ . . . . .	63
4.16	KCS blade and trailing wake geometry . . . . .	65
4.17	Comparison of open-water performance - calculation and experiment . . . . .	66
4.18	KCS wake field distributions in model and full scale - nominal and effective distributions. The measured and estimated model and full-scale wake fields are provided by SVA. The calculated wake fields are obtained by SHIPFLOW-ESPPRO coupling. . . . .	68
4.19	Non-cavitating propeller loads in behind condition for effective model and full-scale wake fields . . . . .	69
4.20	Blade surface pressure distribution ( $-C_{pn}$ ) for model-scale flow conditions. Top row: ESPPRO results, bottom row: SVA viscous flow calculations (color legend only applies to the ESPPRO results)	70
4.21	Arrangement of the pressure pick ups . . . . .	70
4.22	Comparison of the ESPPRO results with the results of the experiment for model and full-scale wake fields in non-cavitating condition . . . . .	71
4.23	Comparison of pressure amplitude for P2 (directly above the propeller) between model and full-scale wake fields for both the ESPPRO and the experimental results in non-cavitating condition	72
4.24	Calculated propeller forces in cavitating condition for model and full-scale effective wake fields . . . . .	73
4.25	Blade surface pressure distribution ( $-C_{pn}$ ) in cavitating and model-scale flow conditions ( $\sigma_n = 1.489$ ) . . . . .	73
4.26	Comparison of cavitation extent between the ESPPRO results and the results from experiment for model-scale wake field . . . . .	75
4.27	Comparison of cavitation extent between full-scale wake (left) and model-scale wake (right) . . . . .	76
4.28	Harmonics of the pressure signal for cavitating condition showing with and without TVC and comparing with experimental results for model-scale wake (top) and zoom in (bottom) . . . . .	78

List of Figures

4.29	ESPPRO results with and without TVC compared to experiment results for model-scale wake field simulations - the arrangement of the plots follow the pick ups arrangement . . . . .	79
4.30	Harmonic amplitudes of the pressure signal for the KCS propeller in cavitating condition showing with and without TVC and comparing with experimental results for full-scale wake (top) and zoom in (bottom) . . . . .	80
4.31	ESPPRO results for the KCS propeller with and without TVC compared to the experimental results for full-scale wake field - the arrangement of the plots follow the pick ups arrangement as shown on the left bottom corner . . . . .	81
4.32	Comparison of pressure fluctuations for pick up P2 directly above the propeller between model and full-scale wake fields for the KCS propeller in cavitating condition . . . . .	82
4.33	Calculated wake fields for the bulk carrier . . . . .	84
4.34	Radius and circulation of the cavitating segments along the tip vortex line of the key blade (blade at 12 o'clock position and without sheet cavitation) . . . . .	85
4.35	Pressure signal induced by only the cavitating tip vortex and the harmonics amplitudes . . . . .	87
4.36	Total pressure signal and the harmonic analysis (without sheet cavitation) . . . . .	88
4.37	Volume of the entire cavitating tip vortex and its harmonic analysis . . . . .	89
4.38	Cavitating segment's circulation along the tip vortex line for the three cases both with and without sheet cavitation. <i>MM</i> and <i>MF</i> refer to propeller <i>M</i> in model nominal and full effective wake and <i>FF</i> to propeller <i>F</i> in full effective wake . . . . .	90
4.39	Initial radius for propeller <i>M</i> in nominal model-scale wake field . . . . .	91
4.40	Radius of the cavitating segments at 4 different time steps for propeller <i>M</i> in effective full scale wake field . . . . .	92
4.41	Propeller <i>F</i> in effective full-scale wake distribution . . . . .	93
4.42	Pressure signal induced by only the cavitating tip vortex and harmonics amplitude . . . . .	94
4.43	Total pressure signal and its harmonic analysis . . . . .	95
4.44	Volume of the cavitating tip vortex . . . . .	96
4.45	Sheet cavitation volume on propeller <i>F</i> with and without TVC influence . . . . .	96

## References

- P. Andersen, J. J. Kappel, and E. Spangenberg. Aspects of Propeller Developments for a Submarine. In *Proceedings of the Second International Symposium on Marine Propulsors*, Trondheim, Norway, 2009. Cited on p. 52
- R. E. A. Arndt. Cavitation in Vortical Flows. *Annual Review of Fluid Mechanics*, 34:143–175, 2002. Cited on pp. 6 and 19
- R. E. A. Arndt, H. Higuchi, and C. J. Quadrelli. Tip Vortex Cavitation. In *Cavitation and Multiphase Flow Forum – 1985*, Albuquerque, New Mexico, 1985. Cited on pp. 6 and 19
- S. Berger. *Numerical Analysis of Propeller-Induced Higher-Order Pressure Fluctuations on the Ship Hull*. PhD thesis, Hamburg University of Technology, 2018. Cited on p. 53
- S. Berger, R. Gosda, M. Scharf, R. Klose, L. Greitsch, and M. Abdel-Maksoud. Efficient Numerical Investigation of Propeller Cavitation Phenomena causing Higher-Order Hull Pressure Fluctuations. In *Proceedings of the 31st Symposium on Naval Hydrodynamics*, Monterey, California, 2016. Cited on pp. 4, 8, 10, 18, 21, 22, 25, 48, and 50
- M. L. Billet and J. W. Holl. Scale Effects on Various Types of Limited Cavitation. *Journal of Fluids Engineering*, 103(3):405–414, 1981. ISSN 00982202. DOI: 10.1115/1.3240800. Cited on p. 7
- J. Bosschers. A Semi-Empirical Method to Predict Broadband Hull Pressure Fluctuations and Underwater Radiated Noise by Cavitating Tip Vortices. In *Proceedings of the Fifth International Symposium on Marine Propulsors*, Helsinki, Finland, 2017. Cited on pp. 4 and 10
- J. Carlton. *Marine Propellers and Propulsion*. Butterworth-Heinemann Ltd., 2007. ISBN 9780750681506. Cited on pp. 2, 4, and 5
- J. Choi, C.-T. Hsiao, G. Chahine, and S. Ceccio. Growth, Oscillation and Collapse of Vortex Cavitation Bubbles. *Journal of Fluid Mechanics*, 624:255–279, 2009. Cited on pp. 30 and 33

## References

- N. E. Fine. *Nonlinear Analysis of Cavitating Propellers in Nonuniform Flow*. Phd thesis, Massachusetts Institute of Technology, 1992. Cited on pp. 1, 9, 11, and 27
- J.-P. Franc and J.-M. Michel. *Fundamentals of Cavitation*. Springer, 2004. ISBN 1402022336. Cited on pp. 2, 4, 5, 6, 7, 15, 18, 20, 21, 22, 25, 29, 30, and 48
- D. H. Fruman, P. Cerrutti, T. Pichon, and P. Dupont. Effect of Hydrofoil Planform on Tip Vortex Roll-Up and Cavitation. *Journal of Fluids Engineering*, 117(1):162–169, 1995. ISSN 00982202. DOI: 10.1115/1.2816806. Cited on p. 7
- D.H. Fruman, C. Dugue, A. Pauchet, P. Cerrutti, and L. Briancon-Marjollet. Tip vortex roll-up and cavitation. In *Proceedings of the 19th Symposium on Naval Hydrodynamics*, Seoul, Korea, 1992. Cited on p. 7
- C.-T. Hsiao, G. Chahine, and H.-L. Liu. Scaling Effect on Bubble Dynamics in a Tip Vortex Flow: Prediction of Cavitation Inception and Noise. Technical report, 2000. Cited on pp. 6, 19, 20, and 55
- J. Hundemer and M. Abdel-Maksoud. Prediction of Tip Vortex Cavitation Inception on Marine Propellers at an Early Design Stage. *Proceedings of the Seventh International Symposium on Cavitation*, 2009. Cited on pp. 15 and 16
- INSEAN. The INSEAN E779A Propeller Dataset Model Geometry Description. Technical report, 2006. Cited on p. 59
- W. H. Isay. Eine Näherungslösung für das Geschwindigkeits- und Druckfeld eines Flügelspitzenwirbels in turbulenter Strömung. Technical report, Institut für Schiffbau der Universität Hamburg, Hamburg, Germany, 1991. Cited on p. 50
- ITTC. Specialist Committee on Cavitation Final Report and Recommendations to the 25th ITTC. In *Proceedings of the 25th International Towing Tank Conference*, pages 473–533, Fukuoka, Japan, 2008. Cited on p. 4
- T. Kanemaru and J. Ando. Numerical Analysis of Steady and Unsteady Sheet Cavitation on a Marine Propeller Using a Simple Surface Panel Method “SQCM”. In *Proceedings of the Ninth International Symposium on Cavitation*, 2015. Cited on p. 4
- G. Kuiper. *Cavitation Inception on Ship Propeller Models*. PhD thesis, Delft University of Technology, 1981. Cited on pp. 6, 18, and 33
- F. H. Lafeber and J. Bosschers. Validation of Computational and Experimental Prediction Methods for the Underwater Radiated Noise of a Small Research Vessel. In *Proceedings of the PRADS16*, Copenhagen, Denmark, 2016. Cited on p. 10

## References

- R. Latorre. TVC Noise Envelope - An Approach to Tip Vortex Cavitation Noise Scaling. *Journal of Ship Research*, 26(1):65–75, 1982. Cited on pp. 15, 20, and 21
- R. Latorre and P. Ligneul. Acoustic Considerations in Tip Vortex Cavitation inception. *Acustica*, 79(3):266–273, 1993. Cited on p. 20
- H. Lee. *Modeling of Unsteady Wake Alignment and Developed Tip Vortex Cavitation*. PhD thesis, University of Texas at Austin, Austin, Texas, 2002. Cited on p. 9
- H. Lee and S. A. Kinnas. Modelling of Unsteady Blade Sheet and Developed Tip Vortex Cavitation. In *Proceedings of the Fourth International Symposium on Cavitation*, Pasedena, California, 2001. Cited on p. 9
- T. Lloyd, G. Vaz, D. Rijpkema, and A. Reverberi. Computational Fluid Dynamics Prediction of Marine Propeller Cavitation Including Solution Verification. In *Proceedings of the Fifth International Symposium on Marine Propulsors*, Helsinki, Finland, 2017. Cited on pp. 8, 58, 60, 61, and 62
- B. W. McCormick. *A Study of the Minimum Pressure in a Trailing Vortex System*. PhD thesis, The Pennsylvania State University, 1954. Cited on p. 6
- B. W. McCormick. On Cavitation Produced by a Vortex Trailing from a Lifting Surface. *Journal of Basic Engineering*, 84(3):369–378, 1962. ISSN 0098-2202. DOI: 10.1115/1.3657328. Cited on pp. 6, 7, and 19
- A. Pauchet, L. Briancon-Marjollet, S. Gowing, P. Cerrutti, and T. Pichon. Effects of foil size and shape on tip vortex cavitation occurrence. In *Proceedings of the Second International Symposium on Cavitation*, pages 133–139, Tokyo, Japan, 1994. Cited on p. 7
- P. Perali, T. Lloyd, and G. Vaz. Comparison of uRANS and BEM-BEM for propeller pressure pulse prediction: E779A propeller in a cavitation tunnel. In *Proceedings of the 19th Numerical Towing Tank Symposium*, pages 90–95, St Pierre d’Oleron, France, 2016. Cited on p. 58
- A. E. Raestad. Tip vortex index – An engineering approach to propeller noise prediction. *Naval Architect*, July/August, 1996. ISSN 03060209. Cited on p. 10
- P. B. Regener. *Hull-Propeller Interaction and Its Effect on Propeller Cavitation*. PhD thesis, Technical University of Denmark, 2016. Cited on p. 11
- P. B. Regener, Y. Mirsadraee, and P. Andersen. Nominal vs. Effective Wake Fields and their Influence on Propeller Cavitation Performance. In *Proceedings of the Fifth International Symposium on Marine Propulsors*, Helsinki, Finland, 2017. Cited on pp. 51, 79, and 83

## References

- D. Rijpkema, B. Starke, and J. Bosschers. Numerical simulation of propeller-hull interaction and determination of the effective wake field using a hybrid RANS-BEM approach. In *Proceedings of the Third International Symposium on Marine Propulsors*, pages 421–429, Launceston, Australia, 2013. Cited on p. 67
- F. Salvatore, H. Streckwall, and T. van Terwisga. Propeller cavitation modelling by CFD - results from the VIRTUE 2008 Rome Workshop. In *Proceedings of the First International Symposium on Marine Propulsors*, Trondheim, Norway, 2009. Cited on p. 58
- K. W. Shin. DES of Tip Vortex Cavitation on a Propeller. In *Proceedings of the 19th Numerical Towing Tank Symposium*, pages 138–143, St Pierre d’Oleron, France, 2016. Cited on p. 8
- SVA. Untersuchung des Einflusses des Nachstromfeldes auf die Kavitation und Druckschwankungen am KRISO Containerschiff KS 621. Technical report, 2003. Cited on pp. 48, 64, 65, and 67
- J. Szantyr. A New Method for the Analysis of Unsteady Propeller Cavitation and Hull Surface Pressures. *Naval Architect*, June, 1985. ISSN 03060209. Cited on p. 9
- J. Szantyr. Analytical prediction of propeller cavitation. *Journal of Ship Research*, August:361–363, 1991. Cited on p. 9
- J. Szantyr. A method for analysis of cavitating marine propellers in non-uniform flow. *International Shipbuilding Progress*, 41(427):223–242, 1994. Cited on p. 9
- J. Szantyr. Dynamic interaction of the cavitating propeller tip vortex with the rudder. *Polish Maritime Research*, 14(4):10–14, 2007. ISSN 1233-2585. DOI: 10.2478/v10012-007-0033-x. Cited on pp. 9, 10, 15, 20, and 22
- G. Vaz, D. Hally, T. Huuva, N. Bulten, P. Muller, P. Becchi, J. L. R. Her-  
rer, S. Whitworth, R. Mace, and A. Korsström. Cavitating Flow Calcula-  
tions for the E779A Propeller in Open Water and Behind Conditions: Code  
Comparison and Solution Validation. In *Proceedings of the Fourth Interna-  
tional Symposium on Marine Propulsors*, pages 330–345, Austin, Texas, 2015.  
Cited on pp. 58, 60, 61, and 107
- E. van Wijngaarden. *Prediction of Propeller-Induced Hull-Pressure Fluctuations*.  
PhD thesis, Delft University of Technology, 2011. Cited on p. 4
- E. van Wijngaarden, J. Bosschers, and G. Kuiper. Aspects of The Cavitating  
Propeller Tip Vortex As a Source of Inboard Noise and Vibration. 2005 ASME

## References

*Fluids Engineering Division Summer Meeting and Exhibition*, pages 1–6, 2005.  
DOI: 10.1115/FEDSM2005-77271. *Cited on p. 4*

N. Yilmaz, M. Khorasanchi, and M. Atlar. An Investigation into Computational Modelling of Cavitation in a Propeller's Slipstream. In *Proceedings of the Fifth International Symposium on Marine Propulsors*, number June, Helsinki, Finland, 2017. *Cited on pp. 8 and 58*





DTU Mechanical Engineering  
Section of Fluid Mechanics, Coastal and Maritime Engineering  
Technical University of Denmark

Nils Koppels Allé, Bld. 403  
DK-2800 Kgs. Lyngby  
Denmark

Tlf.: +45 4525 1360  
Fax: +45 4525 1961

[www.mek.dtu.dk](http://www.mek.dtu.dk)

September 2018

ISBN: 978-87-7475-557-9

**DCAMM**  
**Danish Center for Applied Mathematics**  
**and Mechanics**

Nils Koppels Allé, Bld. 404  
DK-2800 Kgs. Lyngby  
Denmark

Phone (+45) 4525 4250  
Fax (+45) 4525 1961

[www.dcammm.dk](http://www.dcammm.dk)

DCAMM Special Report No. S258

ISSN: 0903-1685